Bright Coherent Ultrafast Tabletop Light Sources Development and the Application on EUV to Soft X-Ray Absorption Spectroscopy

by

Chengyuan Ding

B.S., Nankai University, 2004

M.S., Peking University, 2008

M.S., University of Colorado at Boulder, 2013

A thesis submitted to the

Faculty of the Graduate School of the

University of Colorado in partial fulfillment

of the requirement for the degree of

Doctor of Philosophy

Department of Physics

2014

This thesis entitled:
Bright Coherent Ultrafast Tabletop Light Sources Development
and the Application on EUV to Soft X-Ray Absorption Spectroscopy
by Chengyuan Ding
has been approved for the Department of Physics

_____
(Prof. Margaret Murnane)

_____
(Prof. Henry Kapteyn)

Date_____

The final copy of this thesis has been examined by the signatories, and we
Find that both the content and the form meet acceptable presentation standards
Of scholarly work in the above mentioned discipline.

Ding, Chengyuan (Ph.D., Physics)

Bright Coherent Ultrafast Tabletop Light Sources Development and the Application on EUV to Soft X-Ray Absorption Spectroscopy.

Thesis directed by Prof. Margaret Murnane and Prof. Henry Kepteyn

The generation of the advanced bright coherent ultrafast light source from ultraviolet (UV) to soft X-ray have been pursued for decades. It requires the development of light conversion technique, such as high-order harmonics generation (HHG), as well as the driving laser. In this thesis, we first demonstrate the highest pulse energy (10 mJ), single-stage, ultrafast (45 fs) Ti:sapphire amplifier to date, with a repetition rate of 1 kHz. We then use this laser to pump an optical parametric amplifier system and generate 1.3 μm, 30 fs pulses with sufficient energy (2 mJ) for optimally-efficient, phase matched HHG conversion. This allows us to demonstrate the highest flux, soft X-ray HHG source to date with > 10^6 photons/pulse/1% bandwidth at 1 kHz (corresponding to > 10^9 photons/s/1% bandwidth) in a broadband, continuum, spectrum extending to 200 eV, through the fully phase matched hollow waveguide geometry HHG. This photon flux represents an approximately 3 orders-of-magnitude increase compared with past work. Meanwhile, due to the experimental similarity, the high energy ultrashort (10 fs) UV source is implemented in parallel to the soft X-ray source by the four wave mixing (FWM) process. The pulse energy (32 uJ) of UV source is increased by more than 3 times compared with past work, with the pulse duration compressible to less than 13 fs. Finally, utilizing the unique bright supercontinuum HHG soft X-ray source, we have demonstrated soft X-ray absorption spectroscopy of multiple elements and transitions in molecules simultaneously, with the ability to resolve near edge fine structure with high fidelity. The Xeon photon-ionization

process is also resolved in the EUV transient absorption spectroscopy experiment by tuning the soft X-ray source to the EUV region, which shows the stability, tunability, and applicability of our tabletop extreme nonlinear light source for the time-resolved experiments.

Dedication

To my wife, Jingjing Li, and parents.

Acknowledgements

First of all, I would like to thank my advisors Prof. Margaret Murnane and Prof. Henry Kapteyn for their continuous support and help in the last five years and five months. Without them, this thesis work would not have been possible. They not only provided me the opportunity to work in the world-class researches, especially the ultrafast coherent light source development, but also taught me how to succeed in the research career, which would benefit me for life.

Next, I am very grateful to everyone in the KM molecule group who has taught me so much. Dr. Xinbin Zhou introduced me to the KM group and the AMO project. Dr. Robynne Lock taught me the alignment of the molecules and most of the optics lab work when I first started. Most importantly, I would like to thank Dr. Wei Xiong, now a new professor in University of California, San Diego. We worked closely for a couple of years on the soft X-ray generation and transient absorption projects. He taught me what a real Ph.D. means. I also greatly appreciate Daniel Hickstein. He is the man I collaborated with from the first day in KM group till now, and he helped me in every aspect of the research work. I am also grateful to Tingting Fan who I have collaborated with on the transient absorption experiment. Additionally, Dr. Ellen Keister and Dr. William Peters brought many great ideas to our projects. Currently, Jennifer Ellis is working on the VMI project. A

big thanks goes to all those in the KM molecule group who have made working here a pleasant experience.

Also very important to thank is Dr. Xiaoshi Zhang. He taught me how to build the most powerful laser from scratch, and he also taught me the femto-second machining technique, which is critical in my research on the soft X-ray generation. I am also very grateful to Prof. Lino Misoguti. He helped me to demonstrate the brightest ultrafast UV, which is the first achievement during my Ph.D. career. Additionally, I greatly appreciate Dr. Tenio Popmintchev and Dr. Ming-Chang Chen for their introduction to the long wavelength driven HHG. I also owe my thanks to Matt Seaberg and Dan Adams for their contribution on the pulse shaper, which makes the shortening of the output pulse from the regenerative amplifier possible. Moreover, I would like to thank Paul Arpin who I have collaborated with to keep the Red Dragon working, and he started the soft X-ray transient absorption experiment, which is the final project in this thesis.

I also would like to take this opportunity to thank other members of my thesis committee: Prof. David Jonas, Dr. Agnieszka Jaroń-Becker, and Prof. Ralph Jimenez. It is my great honor to have them serve on my thesis committee. I also appreciate Prof. Steven Cundiff and Prof. Andreas Becker for serving on my Comps III exam committee.

I also would like to thank Sterling Backus and Bob Bower. The experience in KMLabs and EUV ERC will equip me for life.

Finally, I would like to thank my friends and family for their support. My friends have kept me sane. My parents have always believed in me. Most of all, a special thank goes to my wife Jingjing Li, who accompanied me for five years at CU-Boulder. Without her I would never be able to overcome the difficulties and finally accomplish my Ph.D. study.

Contents

Chapter

Figures

Figure

Chapter 1

Introduction and thesis outline

1.1 Introduction

The generation of the bright advanced coherent ultrafast light sources in the spectrum region from ultraviolet (UV) to X-ray has been pursued for decades. At the long wavelength side of the region, the excited electronic states of gas phase molecules and materials lie in the spectrum of UV to vacuum ultraviolet (VUV). Thus, the availability of an ultrafast UV to VUV light would allow the excited state to be accessed. At the short wavelength side, the ultrashort wavelength associated ultra-fine (nanometer 10^{-9} m) spatial resolution and ultra-short (attosecond 10^{-18} s) temporal resolution make the coherent X-ray ideal tools of the nanoworld, such as the imaging of nanometer scale small features and the attosecond time scale coherent control of the fast electrons [1]. Moreover, the chemical and elemental specificity of the coherent X-ray absorption enables the coherent X-ray source a unique probe for the complex chemical and biological samples. However, the developments of both the coherent ultrafast UV-VUV source and coherent X-ray source are challenging. For the UV-VUV generation, the up-conversion from nonlinear crystals only allows the generation of wavelength longer than 160 nm. Meanwhile, the generated pulse duration is limited by the phase matching bandwidth of the nonlinear crystal, which is typically too long to resolve the fast electronic transitions. The situation of coherent X-ray generation is

even worse due to complex reasons, such as the scarcity of the appropriate pumps and optics for building an X-ray laser, and the low conversion efficiency of the extreme nonlinear process for the up-conversion from the driving light. Therefore, special techniques are required to develop the bright coherent X-rays source and the ultrafast coherent UV-VUV source.

Specifically, to obtain the bright coherent tabletop soft X-ray source, high-order harmonic generation (HHG) is utilized. It upconverts light from a tabletop femtosecond laser, while retaining excellent spatial coherence when implemented in a phase matched geometry, as well as temporal coherence that easily supports zeptosecond to attosecond synchronization with the driving laser [2-6]. Thus HHG provides an advanced light source complementary to facility-scale coherent X-ray sources [7-9]. By producing x-ray pulses with durations of <100 attoseconds [10-12] and wavelengths < 1 nm [6], HHG is opening up new research opportunities in molecular spectroscopy [13-16], materials science [17-23], as well as nanoscale coherent diffractive imaging [24, 25]. So far, most implementations of HHG have used Ti:sapphire driving lasers at a wavelength around ~0.8 μm. In this case, phase matching considerations limit bright HHG to photon energies <≈ 100 eV, which lie in the extreme ultraviolet (EUV) region of the spectrum. This limits applications of HHG to very thin samples and a relatively small number of elements which have absorption edges in the EUV. Fortunately, a recent breakthrough extended phase matching of HHG to much higher keV photon energies (i.e. shorter HHG wavelengths), by using longer wavelength mid-infrared driving lasers at wavelengths from 1.3 to 3.9 μm [6, 26-29]. However, these preliminary studies were done using lasers operating at tens of Hz repetition rates, with a total photon flux of 10^6 photons per second in 1% bandwidth [28], which is insufficient for broad applications in spectroscopy or imaging. To fully harness the unique properties of soft X-ray HHG, kHz or higher repetition-rates are required in a phase matched geometry. This

goal requires the development of stable, compact, high pulse-energy, ultrafast laser amplifiers that can generate multi-millijoule, few cycle, mid-infrared laser pulses required for efficient HHG.

In this thesis, we first demonstrate the highest pulse energy (10 mJ), single-stage, ultrafast (45 fs) Ti:sapphire amplifier to date, with a repetition rate of 1 kHz. This laser then is used to pump an optical parametric amplifier system [30] and generate 1.3 μm, 30 fs pulses with sufficient energy (2 mJ) for optimally-efficient, phase matched HHG conversion. This allows us to demonstrate the highest flux, soft X-ray HHG source to date with > 10^6 photons/pulse/1% bandwidth at 1 kHz (corresponding to > 10^9 photons/s/1% bandwidth) in a broadband, continuum spectrum extending to 200 eV. This photon flux represents an approximately 3 orders-of-magnitude increase compared with past work, which used lower repetition rates, or non-phase matched implementations [27, 31-32].

Due to the experimental similarity to the high flux soft X-ray HHG source, the generation of the high pulse energy ultra-short (~10 fs) UV source is investigated in parallel from the four wave mixing (FWM) nonlinear process. The similar hollow waveguide geometry as being used in the development of the two coherent light sources makes them sharing the similar experiment setup and knowledge such as the spatial modes and near plane-wave propagation inside the waveguide. But, the fundamental difference between perturbative regime (UV generation) and nonperturbative regime (X-ray generation) makes the ultrafast UV generation utilizing the completely different physics to achieve the highest pulse energy. The UV optical parametric chirped pulse amplification (OPCPA) scheme is used to increase the output pulse energy and avoid unfavorable ionization, which is critical in the soft X-ray HHG source. We demonstrate a more than 3 times increase of pulse energy (32 uJ) ultrafast UV source compared with past work, with the pulse duration compressible to less than 13 fs.

Finally, utilizing the unique bright supercontinuum HHG soft X-ray source, we demonstrate soft X-ray absorption spectroscopy of multiple elements and transitions in molecules simultaneously, with 0.25 eV spectral resolution, and with the ability to resolve near edge fine structure with high fidelity. The Xeon photo-ionization process is also resolved in the EUV transient absorption spectroscopy experiment by tuning the soft X-ray source to the EUV region, which demonstrates the stability, tunability, and applicability of our tabletop extreme nonlinear light source for the time-resolved experiments.

1.2 Outline of thesis

This thesis presents the development of the three ultrafast light sources, which includes the 10 mJ, 1 kHz single-stage Ti:sapphire ultrafast amplifier (800 nm), 32 uJ, < 13 fs ultrafast UV pulse (267 nm), and the highest flux (> 10^9 photons/s/1% bandwidth) up to 200 eV soft X-ray HHG source (6 nm), as well as the application of the developed soft X-ray source, which is the observation of the near edge X-ray absorption fine structure (NEXAFS) [33] and EUV transient absorption spectroscopy.

In Chapter 2, we will focus on the development of the Ti:sapphire amplifier, emphasizing on how we have achieved the highest pulse energy. The high pulse energy and the perfect spatial mode are the two prerequisites for the efficient high quality OPA output, which is the driving pulse of the high flux soft X-ray source. Therefore, the high energy amplifier discussed in chapter 2 could be considered as the preparation for the soft X-ray generation (Chapter 4).

In Chapter 3, we will discuss the ultrafast UV generation. In this chapter, we not only explain the reason why the chirped FWM process enables us to obtain the high energy ultrashort UV pulse, but also present the necessary physics of the EM modes inside hollow

waveguide, which can be applied to both the UV generation and HHG. Therefore, chapter 3 could be considered as an independent chapter, as well as the preliminary chapter for the discussion of the HHG in chapter 4. The author do believe, the phase matching (determinant of the macroscopic emission), the mode matching (one of the determinants of the efficiency), and the mode coupling (the prerequisite for the other two) are the three critical points to achieve efficient output from the hollow waveguide geometry.

In Chapter 4, we will explain the long wavelength driving HHG in detail. Both single-atom response and the phase matching problem of HHG will be discussed. And both the classical model and the quantum model will be considered. Especially, we will emphasize on the new cutoff rule in the phase matching condition, which allows us to use the 1.3 um light to achieve soft X-ray source, and explain how the phase matching condition would balance the low single atom yield by the increase of the pressure length product and the transparency with long driving wavelength HHG. The high flux soft X-ray generation is a direct proof of the long wavelength driving HHG theory.

In Chapter 5, we will present the experiment results of the absorption spectroscopy utilizing the soft X-ray source presented in Chapter 4. The high quality NEXAFS of gas SF_6 and solid P_3HT (polymer of thiophene) will be shown. And transient absorption experiment of Xeon photo-ionization will be presented as well. Chapter 5 could be considered as the application of the soft X-ray source, but it is also the start of the new tabletop X-ray spectroscopy technique, which may bring up new physics in future.

Chapter 2

First 10 mJ single-stage kHz regenerative ultrafast Ti:Sapphire Amplifier

2.1 Introduction

The ultrafast (ultra-short) laser pulse is an ideal tool for both scientific research and industrial application. On one hand, the ultra-short pulse duration makes the laser pulse the indispensable probe to the fast atomic or even electronic motion [34], as well as to access the strong field physics up to the relativistic nonlinear optics regime [35], since the peak intensity is inversely proportional to the pulse duration with fixed pulse energy; on the other hand, the ultrafast pulse enables ultra-fine machining, which can be applied to industrial use such as semiconductor chip manufacture [36-37] and medical use such as laser-assisted cataract surgery [38]. Therefore, people have been developing the ultrafast laser since the invention of the laser. Actually, the first ultrafast pulse was implemented by De Maria in 1966, only six years after the first laser was demonstrated, by using a passively mode-locked a Nd:glass laser [39], although the pulse train containing the picosecond pulses was not regular, which remained a problem for 20 years before the use of saturable absorbers from semiconductors [40].

The investigation of the femtosecond laser experienced two periods generally. During 1980s, dye amplifiers were heavily studied in conjunction with the mode-locked dye

laser oscillator [41]. Then, because of the striking difference of saturation fluence of the gain material, for example the saturation fluence of Ti:sapphire is three order of magnitude higher than that of dye, as well as the obvious practical difference associated with solid-state laser vs. liquid-state laser, the broadband solid-state laser has dominated femtosecond lasers since 1990s, especially the Ti:sapphire laser. Here, we want to discriminate femtosecond lasers by oscillators and amplifiers. The mode-locked Ti:sapphire oscillator typically generates pulses with energies on the order of nJ, pulse duration around 10 fs, at the repetition rate of 80 MHz to 100 MHz. This corresponds to peak intensity of order 10^{13} W/cm^2, assuming that the beam is focused to the limit of a square wavelength. However, compared to the static Coulomb field in an atom, this electric field is still weak, so that bound electrons remain bound in the ground state and the conventional perturbation nonlinear optics still holds. In order to reach the strong field regime around 10^{15} W/cm^2, where non-perturbation theory works, an ultrafast laser amplifier is required. In this thesis, only the amplifier, specifically Ti:sapphire amplifier, is going to be discussed. The Kerr lens mode-locking Ti:sapphire oscillator, which provide the seed for the Ti:sapphire amplifier is extensively discussed in almost all ultrafast laser textbook, so it won't be included here.

Since the energy of the output pulse from oscillator (seed) is of nJ, and the amplified pulse energy after the amplifier is expected to be 10 mJ, the overall gain should be around 10^7. Due to the fundamental trade-off in amplifier design, that small signal regime is most favorable for achieving the high gain but is associated with low energy extraction, while the large-signal (saturated) regime allows efficient energy extraction but leads to low gain, in order to achieve high overall gain and efficient energy extraction, the multipass amplification is considered [42]. Generally, there are two types of the ultrafast amplifier, multipass amplifier and regenerative amplifier.

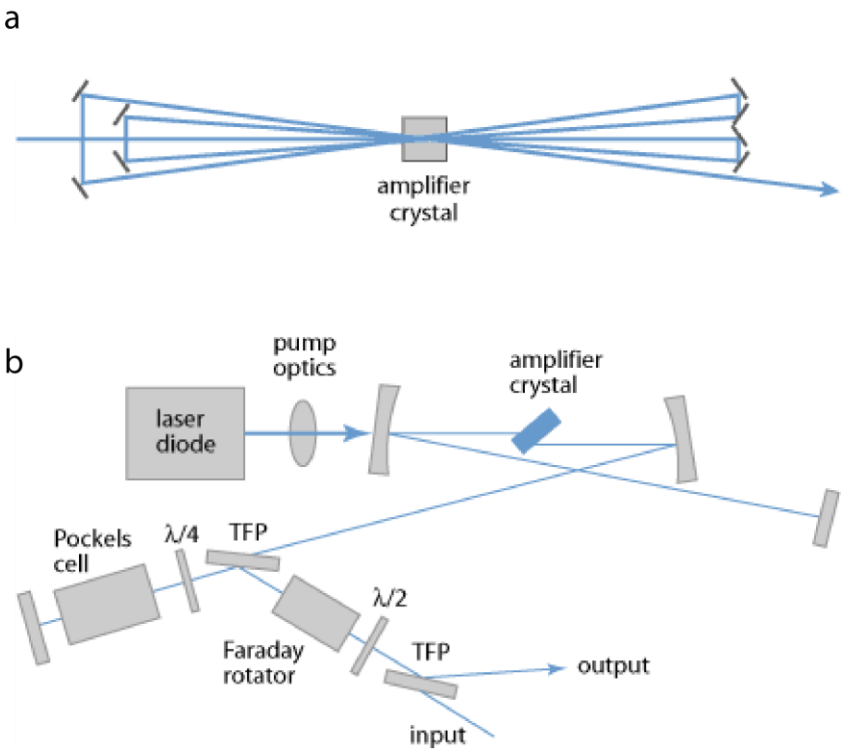

Figure 2.1 (a) Setup of a multipass amplifier. (b) Setup of a regenerative amplifier. Figure captured from Ref. [43].

As shown in Fig 2.1 (a), the multipass amplifier utilizes a fixed geometry to determine the number of passes the seed to be amplified in the gain medium, so the number is fixed; while, the regenerative amplifier combines the electro-optic element, typically a Pockels cell, with polarization control elements, the thin film polarizer (TFP) and quarter waveplate, to realize a polarization gating, during which the seed is trapped inside the regenerative cavity and get amplified (Fig. 2.1 (b)). The Pockels' "on" and "off" switch is acting as the optical switch and the time in between is called Pockels window, which is tunable. The advantage of the multi-pass amplifier is that it typically generates shorter pulse compared to the regenerative amplifier, because it has less material in the beam line as shown in the Fig 2.1, and it typically associated with higher gain therefore

fewer passes through the gain medium is needed to achieve the same overall gain which further reduces the material in the beam line. The advantage of the regenerative amplifier is that it provides a better mode spatial quality because the seed is amplified in a real cavity. Since the purpose of the newly-designed Ti:sapphire amplifier is to pump an optical parametric amplifier (OPA) in order to obtain the high pulse energy infrared driving pulse, and couple the driving pulse into a hollow waveguide for the soft X-ray high-order harmonics generation (HHG), a high energy regenerative amplifier is preferred as the pump laser, because both the OPA and the light coupling are very sensitive to the mode spatial quality while OPA is not sensitive to the pump pulse duration (Section 3.3 and Section 4.4).

2.2 Regenerative amplifier

The schematic diagram of the single-stage 10 mJ kilohertz (kHz) regenerative ultrafast Ti:sapphire amplifier system is shown in Fig. 2.2. Similar to other ultrafast amplifiers, this regenerative amplifier utilizes the chirped pulse amplification (CPA) technique. The seed of 800 nm light pulse is generated from the Kerr-lens passively mode-locked Ti:sapphire oscillator, KMLabs Griffin Series. The typical seed power is 0.5 W with the repetition rate of 80 MHz, which equals pulse energy of 6.25 nJ, and the bandwidth of seed spectrum is from 730 nm to 840 nm tail to tail.

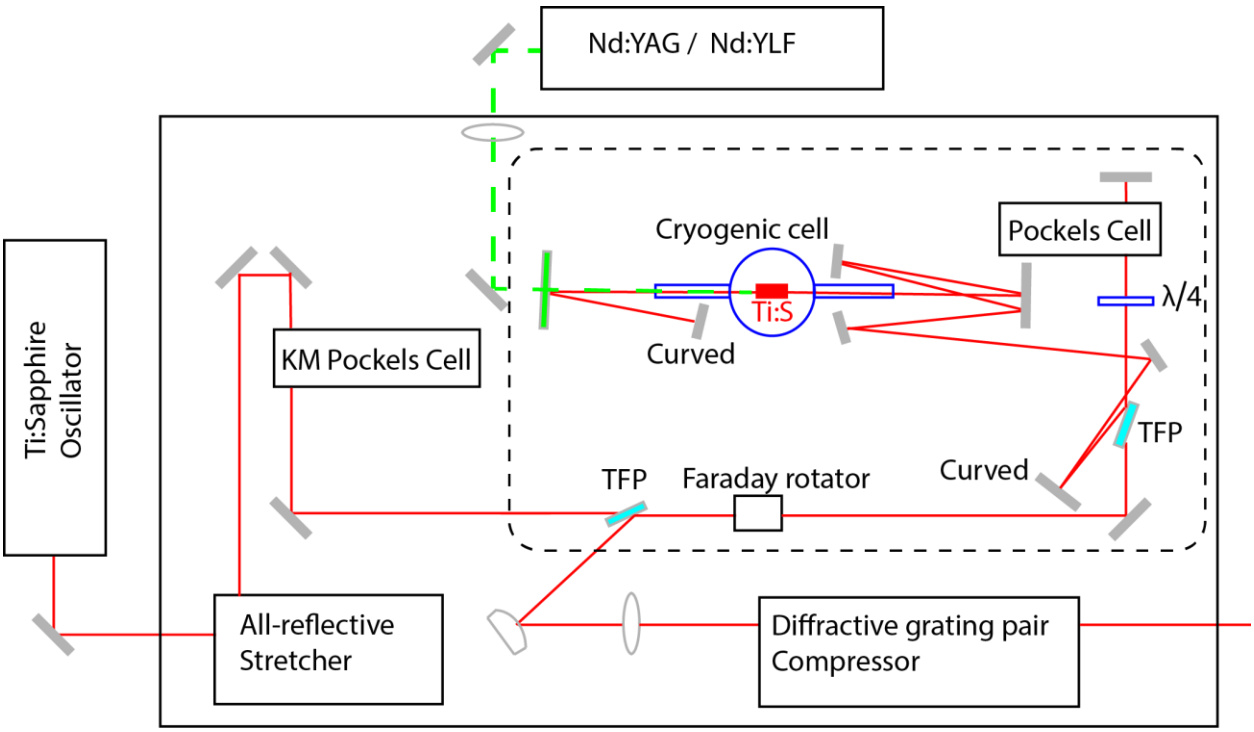

Figure 2.2 Schematic diagram of the 0.2-TW 1kHz single stage regenerative Ti:Sapphire amplifier system.

In the amplifier, as shown in the big solid black block, the seed is first chirped from 10 fs to more than 100 ps by an all-reflective stretcher [44]. Then, the stretched pulse passes through the KMLabs home-built Pockels cell, and the repetition rate of the seed pulses is picked from 80 MHz to 1 kHz before the regenerative cavity. The core part of the regenerative amplifier starts from the dashed black box, and all important elements of the regenerative amplifier are emphasized in the dashed box. The function of the thin film polarizer (TFP) is to transmit the "p" polarized light and reflect the "s" polarized light. The input seed is "p" polarized, so it can pass through the first TFP (on the left in Fig. 2.2) and go into the regenerative amplifier. The function of the Faraday rotator is to rotate the polarization 90 degree when the light travels from right to left while to keep the polarization in the opposite direction, so the input seed can pass through Faraday rotator

and keep “p” polarized since it’s from the left to right before it enters the regenerative cavity. Then, the input seed passes through the second TFP (on the right in Fig. 2.2) since it is still “p” polarized at this time. After that, if there is no Pockels cell or if the Pockels cell is off, the “p” polarized seed will be switched to “s” polarized light once since it passes through the quarter waveplate twice when it bounces the end-mirror on the right-top corner, then it will travel inside the cavity for one round trip after being reflected by the 2nd TFP since it’s “s” now, and then be switched back to “p” polarized light the second time it passes through the quarter waveplate twice, and finally it can pass through TFP and exit and regenerative cavity. After that, since it passes the Faraday rotator from right to the left, it will change the polarization again from “p” to “s”, and it will be reflected by the first TFP and exit the core part of the regenerative amplifier. So, if the Pockels cell is off, the seed travels through the regenerative cavity only once, and no real amplification would happen. The key to control the seed amplification, that how many times the seed is amplified inside the regenerative cavity, is by using Pockels cell. The function of the Pockels cells is like a quarter waveplate, so combining it with the quarter waveplate, when the Pockels cells is on, they work as a half waveplate, and since the seed will pass them twice every time it bounces the end mirror, they don’t change the polarization at all, so the “s” polarized light will be trapped inside the regenerative cavity and get amplified until the Pockels cell turns off, and after it is off, the amplified pulse will be changed back to “p” polarization and exit the cavity. Meanwhile, since the pulses outside the cavity are “p” polarized, when the Pockels cell is on, there is no chance they can change to “s” polarized light, so they will be blocked outside the cavity. (In principle, there is no pulse outside the cavity in our case since we have used the KMLabs homebuilt Pockels cell to pick the pulse, however, this pulse-picking Pockels cell is not necessary if the “on” and “off” contrast of the Pockels cell inside cavity is large enough and the regenerative cavity is not larger than oscillator cavity

so that only one seed pulse can be in the regenerative cavity, because Pockels cell inside the cavity can pick the pulse and amplify it at the same time as we explained above.) Therefore, the Pockels cell acts like a gate, and the Pockels cell window determines the seed amplification. Practically, the Pockels cell window should overlap the pump timing and seed timing. The time "on" should be set some time after the rising edge of the pump pulse so the Pockels cell window overlaps with pump timing while still leaves some time for population inversion to build up, and the time "off" should be set right after the gain is saturated, so the amplified pulse can have the highest energy extraction without burning. Finally, after the seed is amplified, it's up-collimated by a pair of convex mirror and lens, then it is compressed by the diffractive grating pair compressor and exits the laser amplifier for use.

So far, the discussion on regenerative amplifier is quite general. Since the unique property of the newly-designed regenerative amplifier is its highest pulse energy in the world for a single-stage amplifier, with perfect spatial mode quality, from now on, we will focus on the key points to achieve the high pulse energy of 10 mJ. Specifically, the maximum output pulse energy obtainable from an ultrafast Ti:sapphire regenerative amplifier is primarily limited by two factors: thermal lensing [45] and optical damage. In order to overcome the two factors, we proposed three ideas: increasing the cavity mode size by enlarging the cavity size and pump mode size, cooling the crystal to the cryogenic temperature by KMLabs patent cryogenic cell and the stretching the pulse longer by higher groove density gratings. As to be discussed in the following sections, the first idea will reduce the thermal lensing and the optical damage simultaneously, and the second idea will greatly reduce the thermal lensing, and the third idea will reduce the optical damage further. We will follow these three ideas, first discuss the thermal lensing effect in the next section, and then derive the relationship between the grating groove density and stretched

pulse duration in the CPA process in order to demonstrate how the stretching is considered practically in the section after that, and finally show the performance of the newly-designed regenerative amplifier and some further investigation of the regenerative amplifier.

2.3 **Thermal lensing**

The term “laser” originated as an acronym for “light amplification by stimulated emission of radiation”. Since stimulated emission requires the population inversion, which doesn’t naturally exist because of the thermal equilibrium between the energy levels of active ions, atoms or molecules, a pump and an appropriate energy level system, which enable the population inversion, are the prerequisite of a laser. The pumping process in a laser material is inevitably associated with the generation of heat for a number of reasons [46]: 1. The energy ratio of the laser emission photon energy to pump photon energy, which is called the quantum defect efficiency. 2. Nonradiative relaxation from the upper laser level to the ground state. 3. A certain amount of background absorption by the laser host material when the spectrum of the pump source is broad. Therefore, the thermal effects in the gain medium, especially the solid-state material, naturally accompany the functioning of the laser, and the problem of solving the thermal issues caused by high average power pump source has arisen almost since the invention of solid-state lasers.

Generally, the thermal effects, including thermal lensing, thermal birefringence [47] and thermal fracture [48], can be attributed to the non-uniform temperature distribution caused by the heat dissipated inside the crystal and cooling at the boundary of the crystal and the stress introduced by the non-uniform temperature distribution. In order to show the causality of the thermal effects clearly, we discuss the simplest model following the

original paper, where heat is assumed to be generated inside the crystal uniformly [49]. It presents the simple expressions of the temperature distribution and stress distribution as well as the general physics pictures of the thermal effects. The thermal lensing effect will be emphasized since it is one of the main obstacles to achieve high energy ultrafast amplifier.

When the heat is generated within the laser rod uniformly by the pump laser and removed by the coolant or just through the thermal contact with laser rod mount along the cylindrical rod surface, and when the thermal steady-state is reached which means the generation of heat equals the removal of heat, the radial temperature distribution in a cylindrical rod can be obtained from the one-dimensional heat conduction equation [46],

$$\frac{d^2T}{dr^2} + \left(\frac{1}{r}\right)\left(\frac{dT}{dr}\right) + \frac{Q}{K} = 0 \tag{2.1}$$

where T is the function temperature with respect to radial coordinate r, Q is the heat generated per volume, and K is the thermal conductivity. The solution of (2.1) is that.

$$T(r) = T(r_0) + \left(\frac{Q}{4K}\right)(r_0^2 - r^2) \tag{2.2}$$

where r_o is the radius of the laser rod. We can see that under the assumption of the uniform heat generation within the laser rod, the temperature profile is parabolic. Since the temperature-dependent change of the refractive index can be expressed as

$$\Delta n(r)_T = [T(r) - T(0)]\left(\frac{dn}{dT}\right) \tag{2.3}$$

by inserting (2.2) into (2.3), we can obtain

$$\Delta n(r)_T = -(\frac{Q}{4K})r^2\left(\frac{dn}{dT}\right) \tag{2.4}$$

Therefore, the temperature-dependent change of the refractive index is parabolic as well.

The non-uniform temperature distribution generates stresses in the laser rod since the hotter inside area is constrained from expansion by the cooler outer zone, as shown in equation (2.2). The expressions for radial σ_r, tangential σ_Φ, and axial σ_z stresses under the condition of plane strain, which means the axial thermal gradient is much smaller than the radial thermal gradient and certainly is satisfied under our assumption, and in the case of free ends, are given by [50],

$$\sigma_r = \frac{\alpha E}{1-\nu}\left[\frac{1}{r_0^2}\int_0^{r_0} T(r)rdr - \frac{1}{r^2}\int_0^{r} T(r)rdr\right] = \frac{Q\alpha E}{16K(1-\nu)}(r^2 - r_0^2) \tag{2.5}$$

$$\sigma_\Phi = \frac{\alpha E}{1-\nu}\left[\frac{1}{r_0^2}\int_0^{r_0} T(r)rdr + \frac{1}{r^2}\int_0^{r} T(r)rdr - T(r)\right] = \frac{Q\alpha E}{16K(1-\nu)}(3r^2 - r_0^2) \tag{2.6}$$

$$\sigma_r = \frac{\alpha E}{1-\nu}\left[\frac{2}{r_0^2}\int_0^{r_0} T(r)rdr - T(r)\right] = \frac{Q\alpha E}{8K(1-\nu)}(2r^2 - r_0^2) \tag{2.7}$$

where E is Young's modulus, ν is Poisson's ratio, α is the thermal coefficient of expansion. From these expressions we can see that the maximum stress is at the surface of the laser rod. When the stress exceeds the maximum surface stress, thermal stress fracture occurs.

Since stress and strain are linked in elastic media by a stress-strain or *constitutive* relationship,

$$\sigma_{ij} = \sum_k \sum_j c_{ijkl} S_{kl} \tag{2.8}$$

where c_{ijkl} is the elastic tensor and S_{kl} is the strain tensor, the stress generated in the laser rod introduces thermal strain, which, in turn, produces refractive index variations via the photoelastic (Acousto-Optics) effect by [51],

$$\Delta\eta_{ij} = \Delta\left(\frac{1}{n^2}\right)_{ij} = \sum_k \sum_j p_{ijkl} S_{kl} \tag{2.9}$$

where p_{ijkl} is the strain-optic tensor. From (2.8), (2.9) and the crystal symmetry the laser rod, we can obtain the refractive index change from the thermal stress. Due the complex tensor calculation, only the final expression is shown here, and the detailed derivation is in reference [47]:

$$\Delta n_r = -\frac{1}{2} n_0^3 \frac{\alpha Q}{K} C_r r^2 \tag{2.10}$$

$$\Delta n_\Phi = -\frac{1}{2} n_0^3 \frac{\alpha Q}{K} C_\Phi r^2 \tag{2.11}$$

C_r and C_Φ are functions of the strain-optic tensor p_{ijkl}, and typically they are not equal as shown in the cubic crystal such as Nd:YAG [47], therefore, the thermal stress introduces the thermal birefringence in radial and tangential direction.

Combining the refractive index change from the nonuniform thermal distribution and thermal stress, we can obtain the total refractive index change in the cylindrical laser rod to be,

$$\Delta n = -2 n_0 r^2 \left[\frac{Q}{8 K n_0} \left(\frac{dn}{dT} \right) + n_0^2 \frac{\alpha Q}{4K} C_{r,\Phi} \right] \tag{2.12}$$

Therefore, the equivalent focal length of the thermal lens can be obtained from the thin-lens formula

$$f' = \left[\frac{Q}{8 K n_0} \left(\frac{dn}{dT} \right) + n_0^2 \frac{\alpha Q}{4K} C_{r,\Phi} \right]^{-1} \Big/ 4 n_0 l = \frac{K}{Q l} \left(\frac{1}{2} \frac{dn}{dT} + n_0^3 \alpha C_{r,\Phi} \right)^{-1} \tag{2.13}$$

where l is the length of the laser rod.

So far, the thermal lensing effect only considers the bulk effect inside the cylindrical laser rod. In order to obtain the full expression of the focal length of the thermal lensing, one so-called end effect, which accounts for the physical distortion of the flatness of the rod

ends or end bulging, has to be considered as well. From thermal expansion, the deviation from flatness of the rod ends is obtained from

$$l(r) = \alpha r_0[T(r) - T(0)] = \alpha r_0 \frac{Q}{4K}(r_0^2 - r^2) \tag{2.14}$$

Then, the equivalent focal length can be obtained from the thick lens formula

$$f'' = \frac{-\left(d^2 l/dr^2\right)^{-1}}{2(n_0 - 1)} = \frac{K}{Q}[\alpha r_0(n_0 - 1)]^{-1} \tag{2.15}$$

Therefore, the general thermal lensing formula for a laser rod has the final expression as

$$f = \left(\frac{1}{f'} + \frac{1}{f''}\right)^{-1} = \frac{K}{Ql}\left(\frac{1}{2}\frac{dn}{dT} + n_0^3 \alpha C_{r,\Phi} + \frac{\alpha r_0(n_0 - 1)}{l}\right)^{-1}$$

$$= \frac{KA}{P}\left(\frac{1}{2}\frac{dn}{dT} + n_0^3 \alpha C_{r,\Phi} + \frac{\alpha r_0(n_0 - 1)}{l}\right)^{-1} \tag{2.16}$$

where A is the pump area, P is the pump power.

The thermal lensing comes from three terms: the temperature gradient term, the thermal stress term and the end bulging term. Typically, the first term is the dominant term in thermal lensing [52]. If we just consider the first term in Equation (2.16), and put the thermal parameters of the Ti:sapphire crystal at room temperature (300 K) and cryogenic temperature (77K) in, we can obtain the thermal lens effective focal length as a function of the pump diameter, which is associated with large cavity design, and we can compare the effective focal lengths at room temperature and at cryogenic temperature, which is associated with cryogenic cooling to the crystal. From Fig. 2.3, we can see that: first, the focal length of the thermal length is increased by more than 200 times (30 cm to 60 meters under the pump diameter of 1.15 mm) by the cryogenic cooling. Second, since the focal length is proportional to the pump area as in Eq. (2.16), for meters long cavity, the

pump diameter should be kept above 1 mm scale to keep the effective focal length to be long enough compared to the cavity size. These two points explain why we are building a larger cavity and using the cryogenic cooling to the Ti:sapphire crystal.

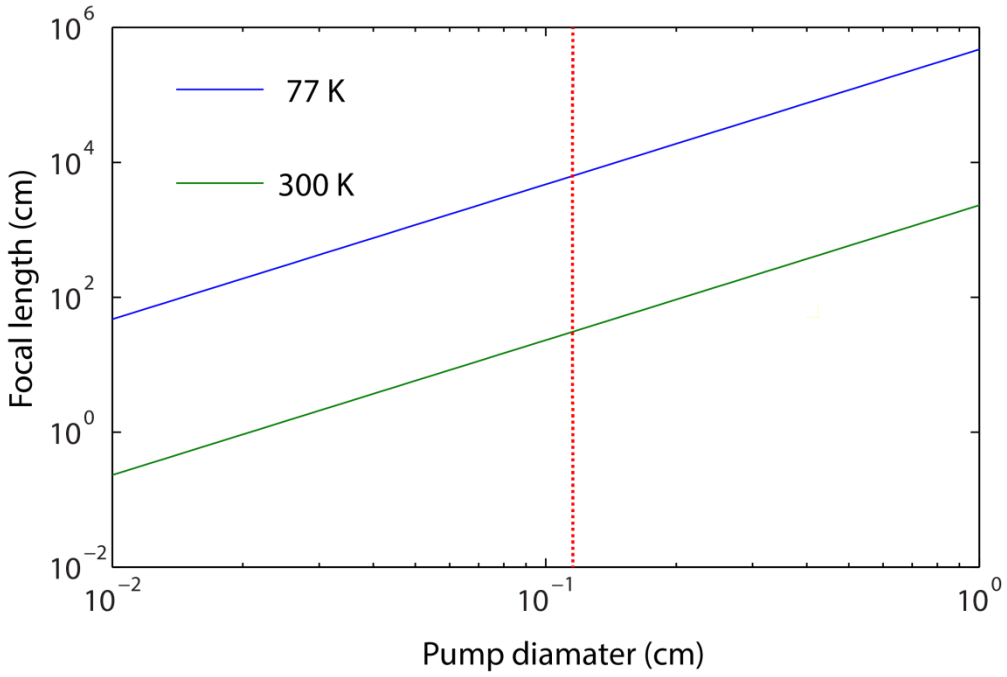

Figure 2.3 Effective focal length based on the uniform continuous pump model. The red vertical line corresponding to real pump size used in our amplifier.

2.4 Grating based optical stretcher and compressor

For the femtosecond pulse amplification, probably the most profound concern is the ultra-high peak intensity induced nonlinear phase accumulation duration the beam propagation through any material, which could introduce self-focusing by the Kerr lens effect [53], even just within the air if the intensity is high enough. One way to characterize

this nonlinear total on-axis nonlinear phase shift accumulated over the length of the amplifier is in terms of *B integral*, written,

$$B = \frac{2\pi}{\lambda} \int n_2 I(z) dz \tag{2.17}$$

Typically in amplifier design, one desires $B \leq 2$, and for $B = 3\sim5$, there is a risk that self-focusing may occur: the Kerr lens effect can become so strong that the beam collapses to a very small radius, so that the optical intensities are strongly further increased and easily exceed the damage threshold. For a femtosecond pulse in the amplifier, for example, an beam with pulse energy of 1 mJ, pulse duration of 50 fs, and mode diameter of 1 mm, passing through 1 cm Ti:sapphire crystal only once without any amplification so the intensity keeps the same along the 1 cm, then the B integral is 112, which is much larger than the desired number. In reality, the number is higher if we consider the multiple passes to reach the gain saturation intensity and other material such as the Pockels cell crystal included in the amplifier. Therefore, the chirped pulse amplification method is used in the ultrafast laser amplifier, which means the seed pulse is first chirped to a much longer pulse duration, typically tens to hundreds of ps, before being amplified through the material, so the accumulated nonlinear phase is 3-4 orders of magnitude smaller the number above, and then amplified pulse is compressed back to the fs pulse duration before use. The chirping and compressing process are achieved by the ultrafast stretcher and compressor.

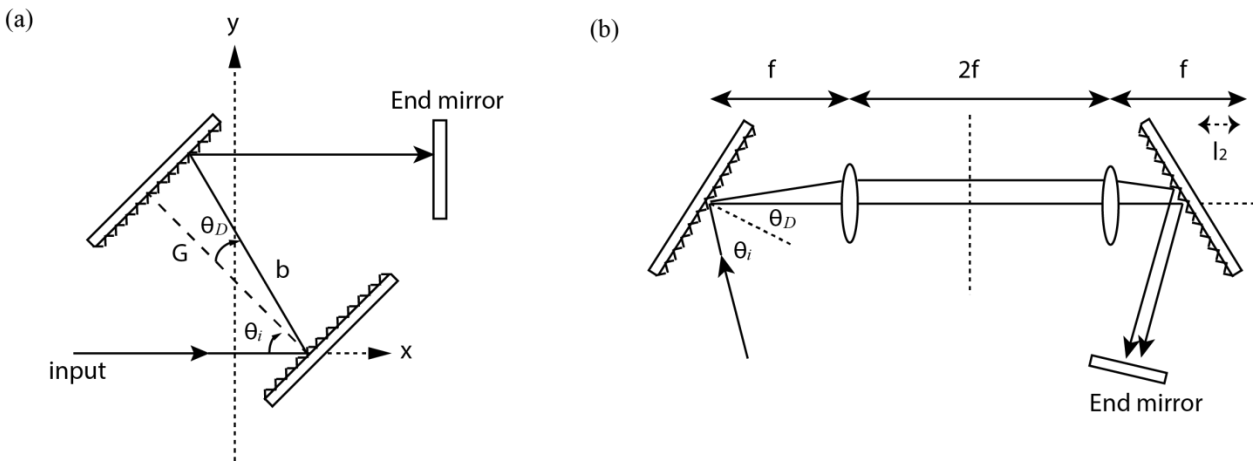

Fig 2.4 (a) Schematic diagram of the grating based compressor. (b) Schematic diagram of the grating pair with internal lens stretcher.

The schematic diagrams of the grating based ultrafast optical compressor and stretcher are shown in Fig 2.4. Some ultrafast optics terminology is needed to describe the function of the compressor and stretcher. From Fourier Optics, if a input pulse $e_{in}(t)$ has the spectrum $E_{in}(\omega)$, after passing through a dispersive system that adds spectral phase $\psi(\omega)$, the output pulse is given by

$$e_{out} = \frac{1}{2\pi}\int d\omega E_{in}(\omega)e^{i\omega t}e^{i\psi(\omega)} \tag{2.18}$$

$\psi(\omega)$ is commonly written in terms of the Taylor series expansions as follows:

$$\psi(\omega) = \psi_0 + \psi_1(\omega-\omega_0) + \frac{1}{2}\psi_2(\omega-\omega_0)^2 + \frac{1}{3!}\psi_3(\omega-\omega_0)^3 + \cdots \tag{2.19}$$

where $\psi_n = \partial^n\psi/\partial\omega^n$. And the propagation constant in the medium of length L is defined as $\psi(\omega) = -\beta(\omega)L$, where

$$\beta(\omega) = \beta_0 + \beta_1(\omega-\omega_0) + \frac{1}{2}\beta_2(\omega-\omega_0)^2 + \frac{1}{3!}\beta_3(\omega-\omega_0)^3 + \cdots \tag{2.20}$$

so $\beta_n = \partial^n\beta/\partial\omega^n = -\psi_n/L$. From these, the group velocity is defined as

$$v_g = (\partial\beta/\partial\omega)^{-1} \tag{2.21}$$

and this is equivalent to the definition of group delay

$$\tau = -\partial\psi(\omega)/\partial\omega \tag{2.22}$$

since $\tau = -\frac{\partial\psi(\omega)}{\partial\omega} = \frac{\partial\beta(\omega)}{\partial\omega} \cdot L = L/v_g$. From (2.21), if $\beta(\omega)$ or $\psi(\omega)$ is not linear with ω, the envelope of the pulse can't keep invariant since light with different frequency will travel at different group velocity, therefore the part of $\beta(\omega)$ that is not linear in ω is called dispersion, and ψ_n is called nth order nonlinear phase when $n \geq 2$. The concept of the dispersion is probably the most important one in Ultrafast Optics. From Fourier Optics, we know that the temporal transform limit of a pulse exits when its nonlinear spectral phase is zero, so using dispersive devices such as compressor, stretcher and pulse shaper to balance the unwanted dispersion introduced by the materials in order to achieve the shortest pulse is of great importance. Here, we will focus on the dispersion in our amplifier, specifically, the compressor and stretcher, so that we can understand how it helps to achieve the high pulse energy.

We first discuss the dispersion of the compressor. As shown is Fig 2.4 (a), the grating based compressor is composed of a pair of identical grating placed in parallel facing each other. The distance between the two gratings is called G, the incidence angle of the input beam is θ_i, then by the grating equation, the diffraction angle is determined by,

$$\sin(\theta_D) = \sin(\theta_i) + m\lambda/d \tag{2.23}$$

where d is the periodicity of the grating rulings and m is the diffraction order. If we use the speed of light c, λ and ω is related by.

$$\lambda = 2\pi c/\omega, \frac{d\lambda}{d\omega} = -2\pi c/\omega^2 = -\lambda^2/2\pi c \tag{2.24}$$

From Eq. (2.23) and Eq. (2.24), a particular frequency component ω will travel at a particular diffracted angle θ_D, so the compressor introduces the angular dispersion. In general, if a beam travels through an infinite uniform dispersive medium $n(\omega)$ for a distance L at the reference ω_0 direction, the frequency-dependent phase difference $\psi(\omega)$ between the start and end wavefront is given by,

$$\psi(\omega) = -\omega L n(\omega)\cos\theta(\omega)/c \tag{2.25}$$

where $\theta(\omega)$ is the angle between the direction of frequency component ω and the reference ω_0. This expression is true in the case of passing through a uniform slab as well [43]. From (2.24) and (2.25),

$$\psi_2 = \frac{\partial^2\psi}{\partial\omega^2} = -\frac{\lambda^3}{2\pi c^2}\frac{\partial^2 P}{\partial\lambda^2} \tag{2.26}$$

where $P(\omega) = Ln(\omega)\cos\theta(\omega)$ is the optical path. Using the (2.24) and the chain rule, we can obtain,

$$\frac{\partial^2 P}{\partial\lambda^2} = L[\frac{d^2 n}{d\lambda^2}\cos\theta - 2\frac{dn}{d\lambda}\sin\theta\left(\frac{d\theta}{d\lambda}\right) - n\cos\theta\left(\frac{d\theta}{d\lambda}\right)^2 - n\sin\theta\left(\frac{d^2\theta}{d\lambda^2}\right)] \tag{2.27}$$

If the dispersion is evaluated along the reference direction, $\omega = \omega_0$,$\theta = 0$, then,

$$\frac{\partial^2 P}{\partial\lambda^2} = L[\frac{d^2 n}{d\lambda^2} - n\cos\theta\left(\frac{d\theta}{d\lambda}\right)^2] \tag{2.28}$$

From the definition of group delay, we can get

$$\frac{\partial\tau}{\partial\lambda} = -\frac{\lambda}{c}\frac{d^2 P}{d\lambda^2} \tag{2.29}$$

Put (2.28) into (2.29)

$$\frac{\partial\tau}{\partial\lambda} = -\frac{\lambda L}{c}[\frac{d^2 n}{d\lambda^2} - n\left(\frac{d\theta}{d\lambda}\right)^2] \tag{2.30}$$

This expression gives the group delay dispersion, coming from the material dispersion and angular dispersion, with respect to wavelength of propagating beam in the direction of the reference frequency ω_0. In the case of the grating based compressor, if we choose the reference direction to be at the diffracted angle θ_D as shown in Fig 2.4 (a), and considering there is no material dispersion since $n = 1$ between two gratings, then, from Eq. (2.30), the dispersion from grating pairs is

$$\frac{\partial \tau}{\partial \lambda} = 2 \times \frac{\lambda b}{c}\left(\frac{d\theta_D}{d\lambda}\right)^2 \tag{2.31}$$

where a factor of 2 is added because an end roof mirror is used typically as show in Fig 2.4 (a), so there are two passes through the grating pair following the same optical path. This will avoid the spatial chirp in the output beam. In the case of single-pass compressor, the factor of 2 should be omitted. We will keep the factor of 2 since it is the common case. From grating equation (2.23), we can easily obtain,

$$\frac{d\theta_D}{d\lambda} = \frac{m}{d\cos\theta_D} \tag{2.32}$$

Therefore, the dispersion is

$$\frac{\partial \tau}{\partial \lambda} = 2 \times \frac{m^2 \lambda b}{c d^{\,2} \cos^2\theta_D} \tag{2.33}$$

And from (2.26), the 2nd order nonlinear phase is

$$\psi_2 = \frac{\partial^2 \psi}{\partial \omega^2} = 2 \times \frac{m^2 \lambda^3 b}{2\pi c^2 d^{\,2} \cos^2\theta_D} \tag{2.34}$$

And the 3rd order nonlinear phase is

$$\psi_3 = \frac{\partial^3 \psi}{\partial \omega^3} = 2 \times \frac{-3m^2\lambda^4 b}{4\pi^2 c^3 d^{\,2} \cos^2\theta_D}\left(1 + \frac{m\lambda \sin\theta_D}{d\,\cos^2\theta_D}\right) = 2 \times \frac{-3m^2\lambda^4 b}{4\pi^2 c^3 d^{\,2} \cos^2\theta_D}\left(\frac{1-\sin\theta_D \sin\theta_i}{d\,\cos^2\theta_D}\right) \tag{2.35}$$

From (2.34), (2.35), we can see that the 2nd order dispersion of the grating pair based compressor is always negative, and 3rd is always positive. Here, the way we define the sign of the dispersion is following the convention of the Ultrafast Optics, where the sign of the 2nd and the 3rd dispersion of normal material are defined as positive in the visible light region, which means the red light travels faster than the blue light. And the reason of the compressor is name as "compressor" is because the 2nd order dispersion of the compressor has the opposite sign to the normal material, the total spectral phase can be balanced, which means the pulse can be compressed by the compressor.

After obtaining the dispersion of the compressor, let's investigate the dispersion of the stretcher as shown in Fig 2.4 (b). Here, I want to point out that, the stretcher used in the ultrafast amplifier is an aberration free all-reflective design [44]. It uses the concave mirror instead of the lenses, and it uses only one concave mirror and one grating instead of two lenses and two gratings as shown in Fig 2.4 (b). However, the optical paths are equivalent. So we'll use this system to demonstrate the stretcher dispersion. The system shown in Fig 2.4 (b) is also frequently used in Fourier optical systems, called a 4-f system, since plane of where the vertical dashed line shows is the Fourier plane of the left dot on the left grating. In Ultrafast Optics, as shown in Fig 2.4 (b), when the distance between two gratings is are equal to 4*f* and a phase modulator is placed at where the dashed vertical line is, it is a pulse shaper, and we will further discuss this in the next section; when the distance between two gratings is shorter than 4*f*, which is the exact case shown in Fig 2.4 (b), it is a stretcher, which is used in the ultrafast amplifier for CPA; and when the distance between two gratings is longer than 4*f*, it is actually a compressor, the same as discussed above. The reasoning is quite straightforward. Let's first consider the case that the distance between two gratings is exactly 4*f*, then phase accumulated in the two different paths shown in Fig 2.4 (b) are equal because the lens' law. It means when distance between two

gratings is exactly 4*f*, there is no dispersion at all. And only the distance shorter or longer than 4*f* is the optical path that will introduce the angular dispersion as in the case of the grating pair compressors. Therefore, the 2nd order nonlinear phase of the stretcher is

$$\psi_2 = \frac{\partial^2 \psi}{\partial \omega^2} = 2 \times \frac{m^2 \lambda^3 (\pm l_2)}{2\pi c^2 d^{\,2} \cos^2 \theta_D} \tag{2.36}$$

In this formula, the "+" sign applies to the case when the distance is longer than 4*f*, and the "-" sign applies to the case when the distance is shorter. Therefore, from the sign of ψ_2, we can see that, only when distance between two gratings is shorter than 4*f*, the system shown in Fig 2.4 (b), can be used to introduce the dispersion opposite to that of a compressor, which is a true stretcher.

The 2nd and 3rd order nonlinear dispersion of the stretcher and compressor are used for the chirp pulse amplification and balancing the nonlinear dispersion introduced by the material in the amplifier, that is

$$\begin{cases} \psi_2^{(stretcher)} + \psi_2^{(material)} + \psi_2^{(compressor)} \\ \psi_3^{(stretcher)} + \psi_3^{(material)} + \psi_3^{(compressor)} \end{cases} = 0 \tag{2.37}$$

Typically, only the first two orders nonlinear phase (ψ_2 and ψ_3) are considered, which is enough for most ultrafast amplifiers. If higher orders nonlinear phase needs to be included, for example 4th and 5th order nonlinear phase, the prism pair stretcher and compressor can be used together with the grating based stretcher and compressor to balance them. And, in principle, the pulse shaper would be able to fix nonlinear phase of any order.

The final question is how the practical parameter, the grating groove period *d*, and the grating width w_g is related to the maximum chirped pulse duration in the CPA, since the pulse duration determines the pulse intensity so that the optical damage inside the

amplifier. From Fig 2.4 (a), if the input beam in x direction, then, the y coordinate of the output ray is given by

$$y = b\sin(\theta_i + \theta_D) \tag{2.38}$$

Then, assuming $m = -1$, the separation Δy between two output rays at different wavelengths separated by $\Delta\lambda$ is

$$|\Delta y| = \left|\frac{\partial y}{\partial \lambda}\Delta\lambda\right| = \frac{b\cos\theta_i \Delta\lambda}{d\cos^2\theta_D} \tag{2.39}$$

The maximum $|\Delta y|$ is limited by the grating width w_g, that $|\Delta y| \le w_g \cos\theta_i$. Put Equation (2.39) into this relationship and use (2.33) to replace $b/\cos^2\theta_D$, we can obtain,

$$\Delta\tau \le \frac{\lambda w_g}{cd} \tag{2.40}$$

From (2.40), we can see that, for a fixed grating width w_g, the maximum chirped pulse duration is proportional to the grating's groove density $1/d$. In the old stretcher design, 1200 g/mm grating was used, while, in the new design 1800 g/mm is used, so the pulse is chirped 1.5 times longer, which can support pulse energy of 1.5 times more than before.

2.5 Performance of the 10 mJ kHz single-stage Ti:sapphire amplifier

First, the maximum output (compressed) pulse energy is 10.6 mJ when pumped with 50 mJ of 527 nm light from a Nd:YLF pump laser. Since the efficiency of the diffraction grating based compressor is 70%, this represents an optical-to-optical efficiency of the regenerative amplifier of ~30% before compression. To our knowledge, this represents at least a 50% improvement in the pulse energy obtainable from a single-stage amplifier [54].

Second, the 10 mJ single-stage regenerative Ti:sapphire amplifier has a nearly perfect Gaussian mode output (see Fig. 2.5), with M^2 [55] values for both x-axis and y-axis of ~1.1, which means almost all the pulse energy is in the lowest order Gaussian mode. This feature ensures good conversion efficiency and output mode for the OPA [56], which in turn ensures high HHG efficiency, since a good OPA mode efficiently couples into a waveguide and facilitates good phase matching (Chapter 3).

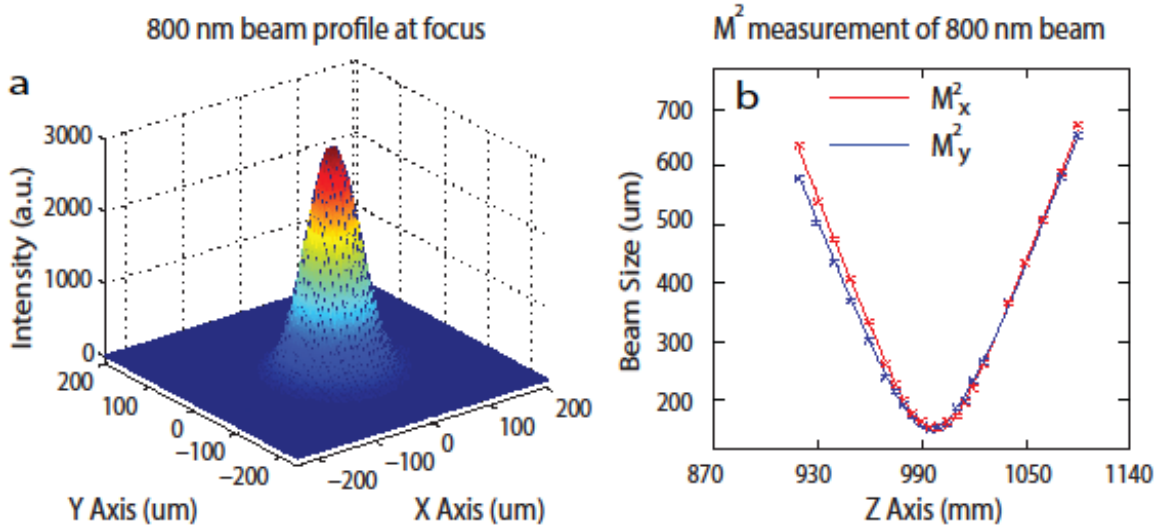

Fig. 2.5. (a) Focal spot of the single-stage laser amplifier output (KMLabs Wyvern HE™), using a 1 m focal length lens; (b) M^2 characterization of the 0.8 μm amplifier output. Data taken at 10 mJ, 1 kHz.

Third, the output pulse duration after the compressor is ≲45 fs, characterized by SHG FROG. It is primarily limited by the bandwidth of the thin film polarizer (TFP) inside the amplifier cavity. Unlike a conventional regenerative cavity, the dispersion introduced

by the material in the regenerative cavity is not the limiting factor for the pulse duration because only 12 passes through the Ti:sapphire crystal are needed to reach the full output power (15 mJ before compression), which is approximately the same number of passes used in a typical multipass ti:sapphire amplifier, but with much higher efficiency. In contrast, a typical regenerative amplifier requires 20-40 passes. In the future, a shorter pulse can be achieved when broader bandwidth, higher-damage-threshold, TFPs becomes available.

Finally, the 8 hours' stability test of the 10 mJ, 1 kHz, Ti:sapphire amplifier shows that the fluctuation of the output power (pulse energy) is within 0.59% RMS (Fig. 2.6), which meets the commercial specs of <1%.

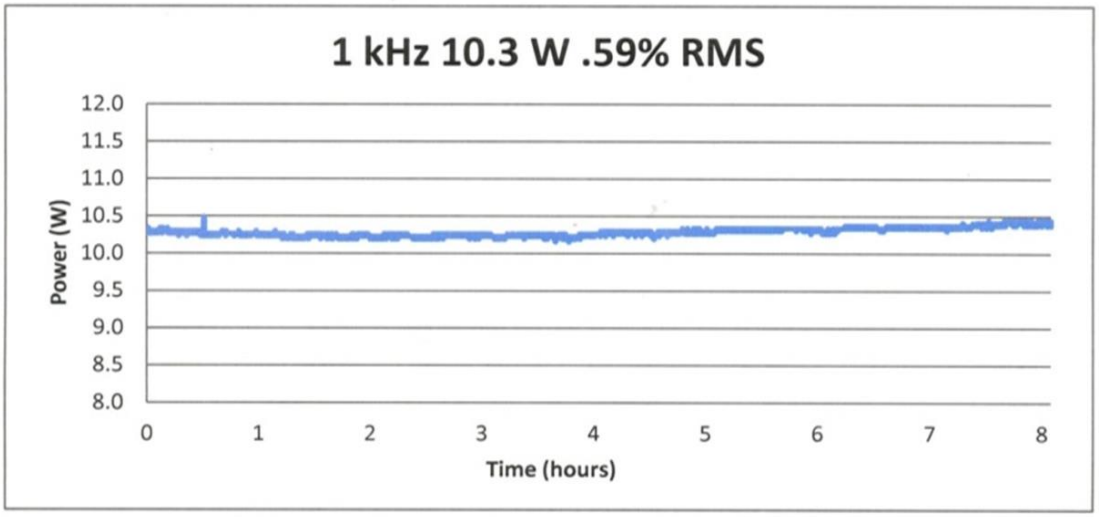

Figure 2.6 The stability test of the 10 mJ kHz Ti:sapphire amplifier for 8 hours.

2.6 Further investigation of the ultrafast amplifier with pulse shaper

After implementing the first 10 mJ single-stage 1 kHz Ti:sapphire amplifier with perfect spatial mode, we further investigate the possibility of reducing the output pulse duration of the regenerative amplifier, since this is the disadvantage of regenerative amplifier compared to the multipass amplifier.

The TFP in the 10 mJ regenerative amplifier limits output bandwidth of the amplified pulse. So, we used another 5 kHz, 3 mJ, regenerative amplifier for the test, which uses different TFP bearing broader bandwidth. Once the broader bandwidth, higher-damage-threshold, TFP becomes available for the 10 mJ amplifier, the results from the 3 mJ amplifier should be implantable to the 10 mJ amplifier.

In order to shorten the amplified pulse, a spectral filter [44] is placed before or in the regenerative cavity, and a pulse shaper [57] built from the 4-f system with the liquid crystal array placed at the Fourier plane is positioned between the oscillator and the amplifier. The function of the spectral filter is to reduce the gain narrowing effect [44] during the pulse amplification so that broader bandwidth can be obtained after amplification, and the function of the pulse shaper is to flatten the higher order phase that compressor can't be fixed.

The results are shown in Fig. 2.7. When no spectral filter is used, the output power is 15 W, and the pulse duration is 44 fs. When the spectral filter is placed before the regenerative cavity, the output power is 14.5 W, and the fully compressed pulse duration is 35.5 fs. When the spectral filter is placed inside the regenerative cavity, the output power is 10 W, and the fully compressed pulse duration is 29 fs, close to what the number from multipass amplifier. Therefore, with the spectral filter and pulse shaper, the pulse duration of the regenerative amplifier can be reduced by sacrificing the output pulse energy.

a

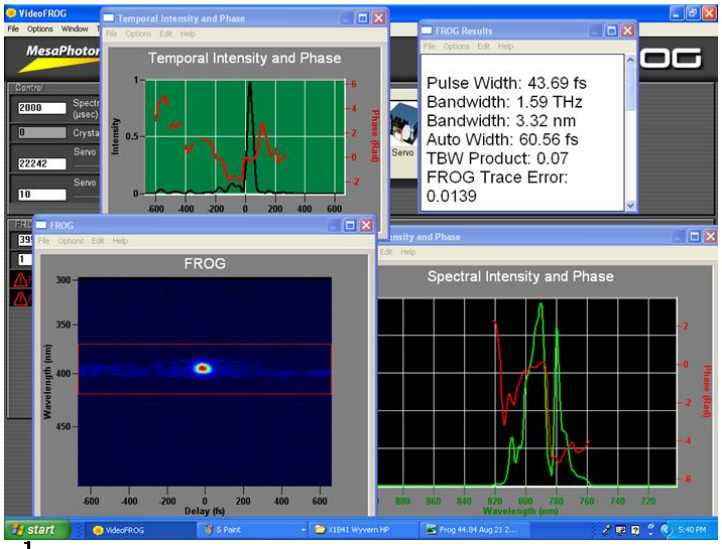
Temporal Intensity and Phase
Pulse Width: 43.69 fs
Bandwidth: 1.59 THz
Bandwidth: 3.32 nm
Auto Width: 60.56 fs
TBW Product: 0.07
FROG Trace Error:
0.0139
FROG
Spectral Intensity and Phase

b

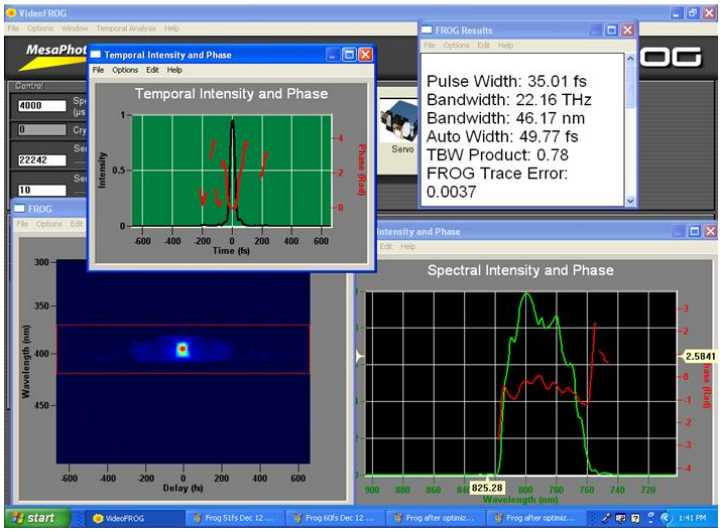
Temporal Intensity and Phase
Pulse Width: 35.01 fs
Bandwidth: 22.16 THz
Bandwidth: 46.17 nm
Auto Width: 49.77 fs
TBW Product: 0.78
FROG Trace Error:
0.0037
Spectral Intensity and Phase

c

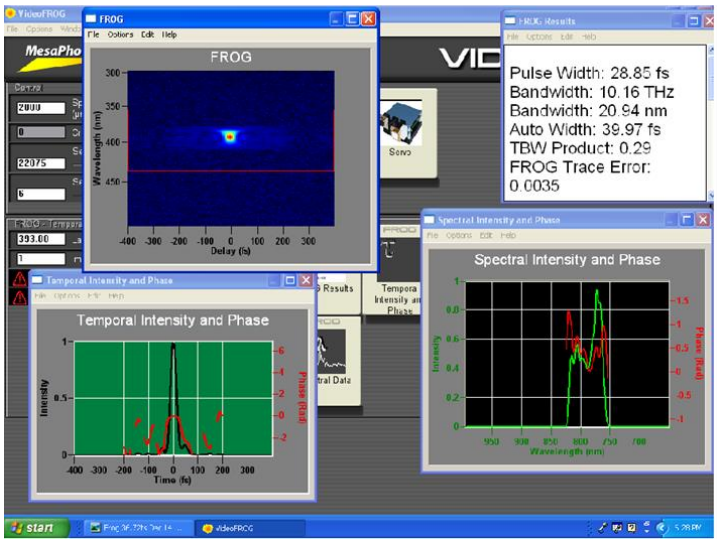
FROG
Pulse Width: 28.85 fs
Bandwidth: 10.16 THz
Bandwidth: 20.94 nm
Auto Width: 39.97 fs
TBW Product: 0.29
FROG Trace Error:
0.0035
Spectral Intensity and Phase
Temporal Intensity and Phase

Figure 2.7 FROG measurement of the amplified pulse, without the spectral filter (a), with the spectral filter before the regenerative cavity (b), with the spectral filter inside the regenerative cavity (c).

2.7 Conclusion and future investigation

In this chapter, we first introduced the history of the development of the ultrafast amplifier. Then, we explained the general operation principle of the regenerative amplifier. In order to explain the three key points, the larger regenerative cavity, the cryogenic cooling to the crystal, and the higher groove density grating in stretcher and compressor, to achieve to first 10 mJ single-stage kHz Ti:Sapphire amplifier, we extensively discussed the thermal issue and the chirping technique for the laser amplifier. Finally, we presented the performance of the newly-designed regenerative amplifier, and investigated the possibility to further reduce the pulse duration of the regenerative amplifier.

Future investigation:

First, test the spatially chirped pulse amplification in the ultrafast Ti:sapphire amplifier. Gain narrowing is one of the primary limiting factors of the bandwidth of the amplified pulse. Different color competing to consume the population inversion makes the situation even worse. Therefore, if the pulse can be spatially chirped on the crystal, and the pump beam can be shaped to amplify the side frequency, then the bandwidth of the amplified pulse could be broadened [58].

Second, further investigate the thermal lens issue. Although expression (2.16) shows clear physics pictures of the thermal lensing and can be used to calculate the focal length of the thermal lens quantitatively to some extent, it's derived from oversimplified

assumptions which typically don't apply to the Ti:sapphire system. On one hand, since the upper laser level lifetime of Ti:sapphire is short (3.2 μs), and the saturation power is very high, another laser, such as Nd:YAG or Nd:YLF, is typically used as the pump source in the end pump geometry. For example, the Ti:sapphire crystal rod used in our 10 mJ system is 1 cm diameter and 1 cm long, while the typical pump beam mode diameter is typically around 1 mm in the crystal in order to make the gain high enough. Therefore the assumption of uniform heat generation inside the crystal is not suitable radially. Meanwhile, the low power single pass absorption at 532 nm (pump wavelength) is 92% (the absorption coefficient γ is 2.5 cm^{-1}), the assumption of uniform heat generation inside the crystal is not suitable axially as well. On the other hand, the generation of the ultra-short pulse at fs time scale is the primary reason of using Ti:sapphire crystal due to its ultra-broad lasing bandwidth, hence, the pump source is typically also a pulsed laser with the same rep rate in the amplifier system (1kHz in our case). Therefore, the assumption of a cw pump source, as in (2.1), is not appropriate as well. An end-pumped pulsed heating thermal lens model is given by R. Lausten [59]. The result differs from the simple model we have presented by orders of magnitude, which predicts a much longer focal length. And C. Durfee et al. measured the transient thermal lens [60], which doesn't agree with R. Lausten's model. No pulsed end-pumped analytical model matches the experiments so far based on the author's knowledge.

Chapter 3

High flux ultrafast UV-VUV generation from 4-wave mixing process

3.1 Introduction

An ultrashort pulse at wavelengths in the ultraviolet (UV) and vacuum ultraviolet (VUV) is of great interest to ultrafast science and technology. On one hand, the excited electronic states of gas phase molecules and materials lie in the UV to VUV. Thus, the availability of an ultrafast UV to VUV light would allow the excited state to be accessed [61-65]. On the other hand, the nonlinear crystal is limited to the generation of narrow-band light at wavelengths longer than 180 nm. Although Watt-level average-power tunable deep ultraviolet (DUV) from 185 nm to 200 nm has been generated by $KBe_2BO_3F_2$ (KBBF) crystal [66] and pulse duration is around 150 fs-200 fs by KBBF and $RbBe_2BO_3F_2$ (RBBF) crystal [66-67], the large group velocity dispersion (GVD) in the UV to VUV region for solid-state materials makes it difficult to reach broad-band phase matching to obtain the pulse duration of < 20 fs with the practical thickness of the material. Meanwhile, the transmission of the crystal is typically limited to 200 nm or so, for example, beta-BaB_2O_4 (BBO) crystal is not transparent below 189 nm, and the shortest phase matched sum frequency generation (SFG) is at 156nm by KBBF whose transmission limit is 155 nm [68]. Due to the demand of the 10 fs pulse, or even less, to match the ultrafast electronic

transitions in the UV-VUV region, the generation of high flux ultrafast UV-VUV pulse is desired.

Charles G. Durfee from our group pioneered the ultrafast UV generation from noble-gas as the nonlinear medium by utilizing four wave mixing (FWM) process in the hollow-waveguide geometry [69-72]. It enables an ultrashort pulse duration of 8 fs and pulse energy of few uJ level at wavelength of 267 nm. By the cascade processes, the 4^{th} and 5^{th} harmonics of Ti:sapphire laser at 200 nm and 160 nm are generated simultaneously. Then, other schemes using gas medium were implemented as well. For example, the scheme that combining the UV multipass excimer amplifier and the SPM in hollow-waveguide generated the highest pulse energy UV light pulse in the < 30 fs region, that is 200 uJ at 248 nm of 24 fs [73]; and the scheme, that using SPM to achieve the ultrashort driving pulse at 800 nm before doing third harmonic generation (THG) through a thin gas jet, generated the shortest UV pulse so far, that is 200 nJ at 263 nm of 2.8 fs [74]. However, although the two schemes pushed the output parameter to the limit, the first one included another laser amplifier and didn't obtain the ~10 fs pulse; and the second one didn't support enough pulse energy for applications due to the short interaction distance. Therefore, the FWM in hollow waveguide geometry is still one of the most commonly used schemes. And since the limitation of this scheme is the input pulse intensity, as the ionization inside the waveguide would violate the phase matching process [72], Charles G. Durfee proposed the chirped FWM ($2\omega + 2\omega - \omega = 3\omega$) in the hollow waveguide geometry to greatly improve the output pulse energy [75], a similar idea to the CPA system as mentioned in the last chapter. The followers have generated the applicable UV-VUV pulse by the chirped FWM process [61, 76-77]. The other commonly used scheme to obtain ultrafast UV-VUV pulse is also by the FWM process but with filamentation guiding instead

of the hollow waveguide guiding [78-81]. Recently, the kagome-style hollow core photonic crystal fiber (HC-PCF) is used to implement to ultrafast UV-VUV pulse [82-83]. Its fabulous fiber dispersion enables many nonlinear phenomena in a super tiny core so that the low pulse energy high repetition rate pulse is preferred for this type of flexible fiber, which attracts great industry interests.

In the following sections, we'll first discuss the modes supported by the hollow waveguide, which is also critical to both ultrafast UV-VUV generation and high order harmonic generation, then explain the three important questions for the ultrafast UV generation in the hollow waveguide: the mode coupling problem, the phase matching problem and the mode matching problem, and finally present our experimental results to support the theories and demonstrate that we have achieved the highest pulse energy of ultrafast UV pulse in ~ 10 fs region. The cascaded VUV generation will be discussed as one of the further experiments since it simultaneously happens with UV generation but needs further investigation.

3.2 Electromagnetic modes in the dielectric hollow waveguide

The diagram of the dielectric hollow waveguide is shown in Fig 3.1. It could be considered as a cylinder of radius a and free space dielectric constant ε_0 embedded in another cylindrical medium of dielectric (or metal) having complex dielectric constant ε. The magnetic permeability μ_0 is assumed to be that of free space for both media. The solution of the cylindrical dielectric waveguide modes was first provided by E. Snitzer [84], while E. Marcatili and R. Schmeltzer first proposed the use of the dielectric hollow waveguide for long distance optical transmission [85].

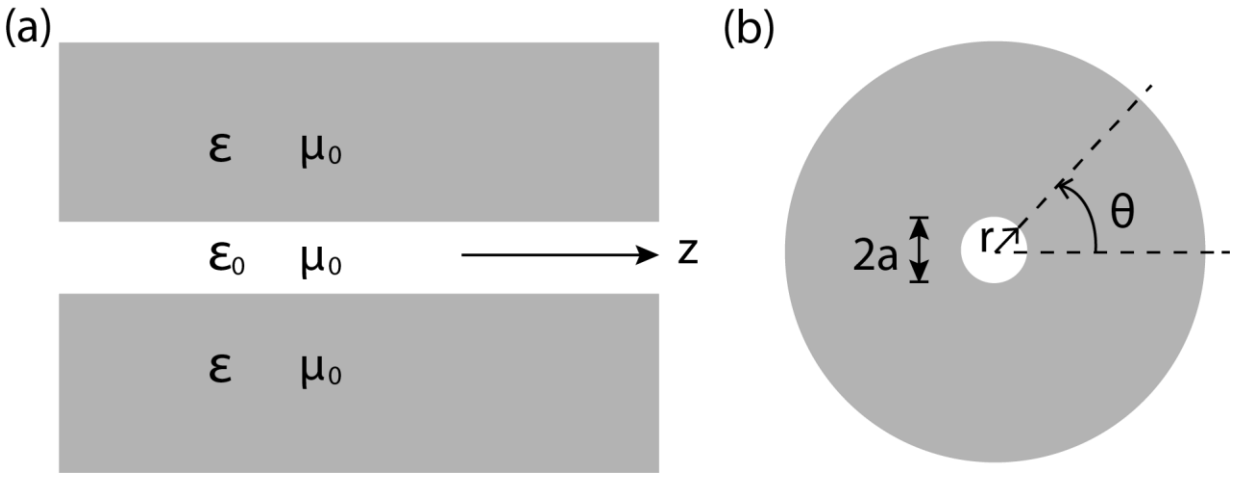

Fig 3.1 (a) Side view of the dielectric hollow waveguide. (b) End view of the dielectric hollow waveguide.

Generally, the problem can be substantially simplified with the assumptions that the radius is much larger than the wavelength of the propagation light and the modes of interests are the low-loss modes whose propagation constants are close to that of free space:

$$ka = 2\pi a/\lambda \gg |\nu|\mu_{nm} \tag{3.1}$$

$$\left|\frac{\gamma}{k} - 1\right| \ll 1 \tag{3.2}$$

where k is the free space propagation constant; $\nu = \sqrt{\varepsilon/\varepsilon_0}$ is the ratio of the refractive index; μ_{nm} is the m^{th} root of equation $J_{n-1}(\mu_{nm}) = 0$, n and m are integers that characterize the propagation mode; and γ is the axial propagation constant of the mode considered. The analytical solutions under the assumptions are given by E. Marcatili and R. Schmeltzer [85]. Before we cite the formulas from E. Marcatili and R. Schmeltzer [85], we want to point out a few things in order to pick up the necessary solutions we are interested in from the general discussion of the dielectric hollow waveguide modes, and make the notations clear

to all readers. First, we are using the notations from E. Marcatili throughout this thesis because they are more commonly used in the society of the UV to X-ray source generation, although in most of the text books, the notations from Snitzer are used since they are original. For example, the important modes such as EH_{1m} modes is labeled as HE_{1m} in the way defined by Snitzer. Second, in general, there are three types of mode supported by the cylindrical boundary conditions with the assumptions, the circular electric mode TE_{0m}, the circular magnetic mode TM_{0m}, and the hybrid modes EH_{nm}. Considering the input lights, 800 nm light and 400 nm light, are both linearly polarized in the same direction, and the third order susceptibility tensor only have nonzero component $\chi^{(3)}_{iiii}, \chi^{(3)}_{iijj}, \chi^{(3)}_{ijij}$, and $\chi^{(3)}_{ijji}$ (for the isotropic material such as the gas used in our experiment, $\chi^{(3)}_{iiii}=\chi^{(3)}_{iijj}+\chi^{(3)}_{ijij}+\chi^{(3)}_{ijji}$), the generated UV light has to be linearly polarized in the same direction in any third order nonlinear problems. So, only the linearly polarized modes in the waveguide are needed to be considered. Third, only the EH_{1m} modes and the combination of $EH_{-|n|,m}$ modes and $EH_{n+2,m}$ modes, which can be called $LP_{|n|,m}$ (linearly polarized) modes [86], ($n \geq 2$), are linearly polarized modes mathematically supported by the waveguide. When the refractive index $\nu \sim 1$, the combinations of the TE_{0m} modes and EH_{2m} modes are also close to linearly polarized light [85], so, in principle, EH_{1m} modes, $LP_{|n|,m}$ modes and the combinations of the TE_{0m} modes and EH_{2m} modes, which can be called $LP_{1,m}$ comprise the complete set for the linearly polarized modes in the waveguide. Forth, the mode selection during the mode coupling process and UV generation process has to be treated separately because of the different initial condition. During the coupling process, the input light can be considered as the lowest order Gaussian distribution TEM_{00}. Since the asymptotical behavior of $LP_{|n|,m}$ modes ($n \geq 1$) (here we have combined the two kinds of combination modes mentioned above) don't fit the lowest order Gaussian distribution TEM_{00}, (for example, the

distributions of $\mathrm{LP}_{|n|,m}$ modes are $E_{\mathrm{LP}_{nm}} = J_n(\mu_{nm} r/a)$ [86]), the $\mathrm{EH}_{1\mathrm{m}}$ modes are considered as the complete basis during the coupling process. However, in the UV generation process, there is no such restriction of the mode selection, so all linearly polarized modes supported by the waveguide boundary condition should be considered.

From the discussions above, only a few modes, $\mathrm{EH}_{1\mathrm{m}}$ and $\mathrm{LP}_{|\mathrm{n}|\mathrm{m}}$ modes, are interesting in our experiments. The field distribution is shown in Fig 3.2 [86]. Under the assumptions (3.1), expressions of $\mathrm{EH}_{1\mathrm{m}}$ mode and $\mathrm{LP}_{|\mathrm{n}|\mathrm{m}}$ modes are

$$E^{y}_{\mathrm{EH}_{1m}}(r) = J_0(\mu_{1m} r/a) e^{i(\gamma_{1m} z - \omega t)} \tag{3.3}$$

$$H^{x}_{\mathrm{EH}_{1m}}(r) = -(\varepsilon_0/\mu_0)^{1/2} E^{y}_{\mathrm{EH}_{1m}}(r) \tag{3.4}$$

$$E^{y}_{\mathrm{LP}_{|n|m}}(r) = J_n(\mu_{nm} r/a) e^{i(\gamma_{nm} z - \omega t)} \tag{3.5}$$

$$H^{x}_{\mathrm{LP}_{|n|m}}(r) = -(\varepsilon_0/\mu_0)^{1/2} E^{y}_{\mathrm{LP}_{|n|m}}(r) \tag{3.6}$$

, where we have assumed the electric field is polarized in the y direction. From now on, the $E^{y}_{\mathrm{EH}_{1m}}(r)$ will be abbreviated to be $E_{1m}(r)$, and $E^{y}_{\mathrm{LP}_{|n|m}}(r)$ will be abbreviated to be $E_{nm}(r)$. The polarization direction is selected arbitrarily, so it becomes a 1-D problem.

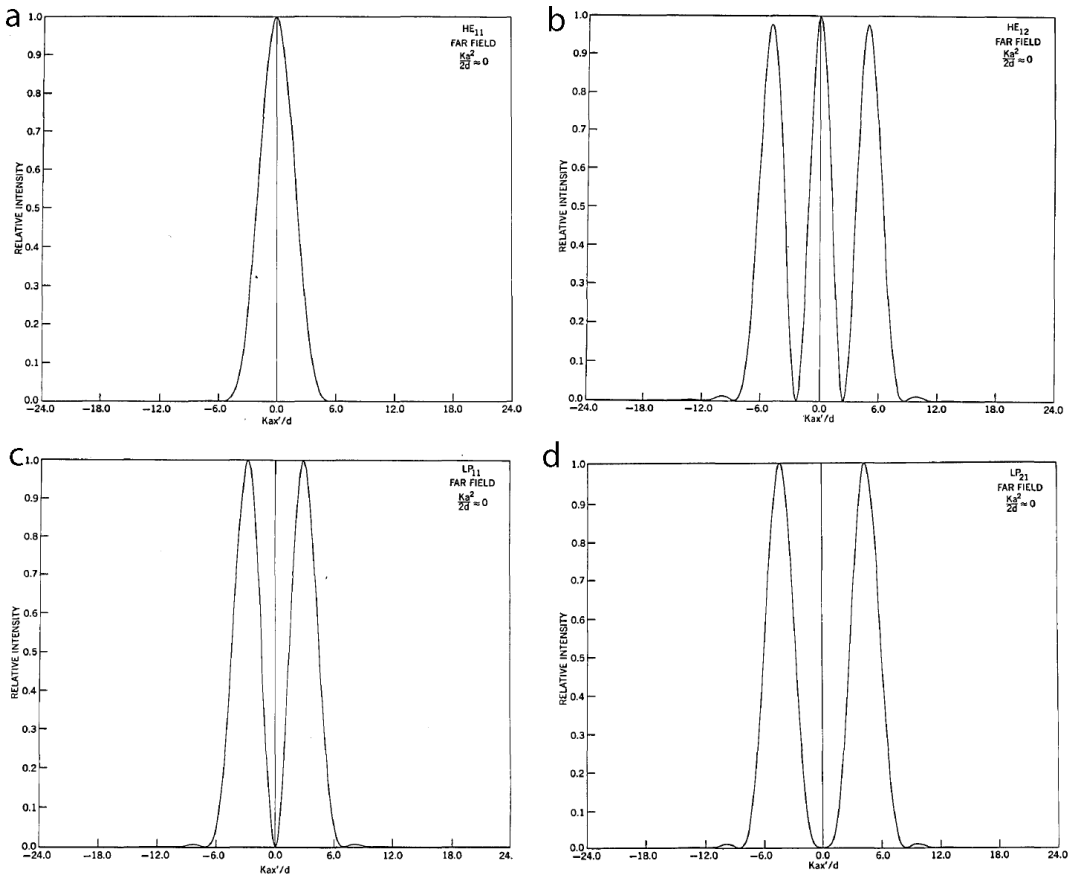

Fig 3.2 (a) The far filed distribution of EH_{11} mode. (b) The far filed distribution of EH_{12} mode. (c) The far filed distribution of LP_{11} mode. (d) The far filed distribution of LP_{12} mode.

Another important parameter is the propagation constant γ_{nm},

$$\gamma_{nm} = k_{nm} + i \cdot \alpha_{nm} \tag{3.7}$$

$$k_{nm} = \frac{2\pi}{\lambda}\left\{1 - \frac{1}{2}\left(\frac{\mu_{nm}\lambda}{2\pi a}\right)^2 \left[1 + \mathrm{Im}\left(\frac{\nu_n \lambda}{2a}\right)\right]\right\} \tag{3.8}$$

$$\alpha_{nm} = \left(\frac{\mu_{nm}}{2\pi}\right)^2 \frac{\lambda^2}{a^3}\mathrm{Re}(\nu_n) \tag{3.9}$$

where

$$\nu_n = \begin{cases} \frac{1}{\sqrt{v^2-1}} & \mathrm{TE}_{0m} \\ \frac{v^2}{\sqrt{v^2-1}} & \mathrm{TM}_{0m} \\ \frac{\frac{1}{2}(v^2+1)}{\sqrt{v^2-1}} & \mathrm{EH}_{nm} \end{cases} \tag{3.10}$$

From (3.6), the phase matching problem can be discussed in the next section. From (3.7) and (3.8), we can see that, for longer wavelength and smaller radius hollow waveguide, the beam would attenuate faster. For example, for beams propagating in the lowest-order mode EH_{11} in a waveguide with core radius $a = 75$ μm and length of 1 meter, the intensity throughput at wavelengths 800, 400, and 267 nm are 52%, 85%, and 93%, respectively.

3.3 Mode coupling, phase matching and mode matching for the hollow waveguide

As in most of the nonlinear optical processes, the phase matching problem is the most important problem in order to obtain an efficient output of ultrafast UV. Since the nonlinear process happens in the hollow waveguide, the mode coupling and mode matching are also determinants to the output flux. In this section, we first discuss the problem of mode coupling since it is the first step of the whole process, affecting the other two problems; then explain the phase matching problem from the derivation of the third order nonlinear process; and then the importance of the mode matching will show automatically by comparing THG and FWM through the derivation.

As we mentioned in the last section, during the light coupling from free space into the hollow waveguide, we assume the incoming beam is a linearly polarized lowest order Gaussian TEM_{00} beam and the beam is at its waist so that the flat wave-front matches the wave-front inside the waveguide, then, the set of EH_{1m} modes can be used as the eigen-

basis of the hollow waveguide modes during the coupling. The TEM_{00} mode is decomposed into EH_{1m} modes as

$$E_{\mathrm{TEM}_{00}} = \sum_m A_m E_{1m} \tag{3.11}$$

where A_m is the coefficient associated with each EH_{1m} mode. Using (3.5), (3.11) and

$$E_{\mathrm{TEM}_{00}} = e^{-\frac{r^2}{w^2}} \tag{3.12}$$

where w is the radius of waist, we can obtain the power coupling coefficients for the EH_{1m} modes from TEM_{00} mode as a function of the ratio of the beam waist to the guide radius, w/a , as shown in Fig. 3.3 [87]. From Fig 3.3, we can see that the entrance of the hollow waveguide is acting as a spatial filter. When w/a = 0.64, all the energy is coupled into the waveguide, and all energy is distributed in the EH_{11} mode. When w/a > 0.64, some of the energy is lost at the entrance and the energy in the waveguide is almost all distributed in the EH_{11} mode. When w/a < 0.64, all energy is coupled into the waveguide and the energy in the waveguide is distributed in the combination of the EH_{1m} modes. In principle, we want to achieve w/a = 0.64 by the selection of focusing lens and hollow waveguide, when the input beam has perfect spatial profile of lowest order Gaussian distribution, M^2 = 1. Practically, it is better to choose the ratio slightly larger than 0.64 in order to clean the mode by the waveguide entrance. Here, we want to point out that, from this calculation, importance of the input mode spatial quality is presented as well. It explains one of the reasons for setting up a regenerative amplifier instead of multipass amplifier mentioned in chapter 2, because the assumptions of the TEM_{00} mode input mode as well as the correct ratio of w/a chose for the coupling process are both the prerequisites that all input pulse energy can be coupled into the EH_{11} mode.

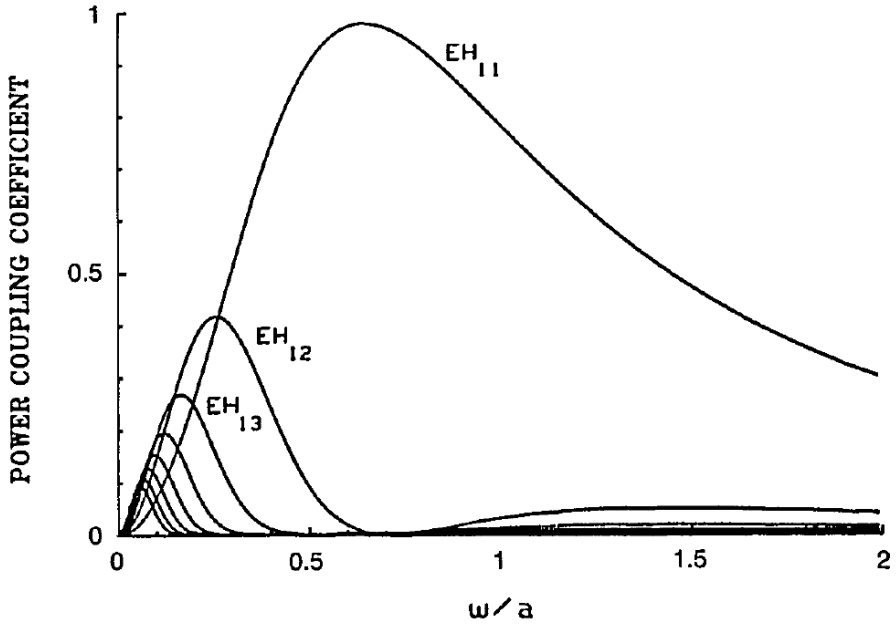

Figure 3.3 Calculations of power coupling coefficients for the EH_{1m} modes as a function of the ratio of the beam waist to the guide radius, w/a. This figure is captured from Ref. [87].

After the discussion of the mode coupling, we now turn to the problems of phase matching and mode matching for generating the ultrafast UV, 3rd harmonic from Ti:Sapphire (267 nm), in the hollow waveguide. In principle, the generation of the 3rd order harmonic could be from THG and FWM processes. The 2nd order sum frequency generation (SFG) from fundamental (800 nm light) and 2nd order harmonics (400 nm light) is forbidden due to the use of gas as the nonlinear medium, since the second order susceptibility vanishes in isotopic materials. We first demonstrate that THG is not an efficient way to generate the ultrafast UV because of the bad mode matching, although it could be phase matched by utilizing the high order modes. If the input 800 nm light and 400 nm light is

labeled as E_1 and E_2, and the output 267 nm light is labeled as E_3, they can be represented in the non-depletion model as:

$$E_1 = \frac{1}{2} f_1(r) F_1(0) \exp[-i\omega t + (ik_1 - \alpha_1)z] + \text{c. c.} \tag{3.13}$$

$$E_2 = \frac{1}{2} f_2(r) F_2(0) \exp[-i2\omega t + (ik_2 - \alpha_2)z] + \text{c. c.} \tag{3.14}$$

$$E_3 = \frac{1}{2} f_3(r) F_3(z) \exp[-i3\omega t + (ik_3 - \alpha_3)z] + \text{c. c.} \tag{3.15}$$

where, $f_1(r), f_2(r)$ and $f_3(r)$ represent the mode distribution of 800 nm light, 400 nm light and 267 nm light respectively, as shown in (3.5) and (3.7); $F_1(0)$ and $F_2(0)$ are the amplitudes of the pulses of the 800 nm and 400 nm light at the entrance of the hollow waveguide; $F_3(z)$ is the slowly varying amplitude of the 267 nm light. Then the THG equation for the slowly varying envelope of the 267 nm light in the hollow waveguide is written as

$$\frac{d}{dz} F_{3,nm}^{THG}(z) + \alpha_{3,nm} F_{3,nm}^{THG}(z) = i\beta_{nm}^{THG} [F_1(0)]^3 \exp(-i\Delta k_{nm}^{THG} z - 3\alpha_{1,11} z) \tag{3.16}$$

We have put the mode number nm in, since different mode has different propagation constant and assumed the energy coupled into the waveguide is all distributed in EH_{11} mode by proper mode coupling. The phase mismatch is then written as

$$\Delta k_{nm}^{\text{THG}} = k_{3,nm} - 3k_{1,11} \tag{3.17}$$

The relevant nonlinear-optical cubic susceptibility is written as [88]

$$\beta_{nm}^{\text{THG}} = \frac{9\pi\omega^2}{2k_{3.nm}c^2} \chi_{\text{THG}}^{(3)} \frac{\iint f_{3,nm}(r)[f_{1,11}(r)]^3 r dr d\theta}{\iint [f_{3,nm}(r)]^2 r dr d\theta} \tag{3.18}$$

Integrating (3.16), we can get

$$F_{3,nm}^{THG}(L) = \frac{i\beta_{nm}^{\mathrm{THG}}[F_1(0)]^3\{\exp(-\alpha_{3,nm}L)-\exp[-(3\alpha_{1,11}+i\Delta k_{nm}^{\mathrm{THG}})L]\}}{\alpha_{3,nm}-3\alpha_{1,11}-i\Delta k_{nm}^{\mathrm{THG}}} \tag{3.19}$$

From (3.19), if we neglect the absorption, the $F_{3,nm}^{THG}(L)$ is a sinc function with respect to the phase mismatch $\Delta k_{nm}^{\mathrm{THG}}$ as expected.

From (3.8) and (3.10), when ν is real which means the dielectric material of the waveguide itself is not lossy, then

$$k_{nm} = \frac{2\pi n(\lambda)}{\lambda}\left[1-\frac{1}{2}\left(\frac{\mu_{nm}\lambda}{2\pi a}\right)^2\right] \approx \frac{2\pi}{\lambda} + \frac{2\pi N_a\delta(\lambda)}{\lambda} - N_e r_e\lambda - \frac{{\mu_{nm}}^2\lambda}{4\pi a^2} \tag{3.20}$$

where N_a is the neutral atomic density, $\delta(\lambda)$contains the gas dispersion function, N_e is the neutral atomic density, and r_e is the classic electron radius. Here, we have assumed that there is some gas with refractive index $n(\lambda)$ in the waveguide as the nonlinear medium. In general, the real part of the propagation constant is the sum of four sources of dispersion: vacuum, gas, free electrons (plasma), and waveguide. Since the THG in argon the critical ionization fraction is only 1.3% [72], (the detailed discussion the problem of the critical ionization for the phase matching is shown in the next chapter for high order harmonic generation), and in UV generation the emitters are not the ionized atoms, typically, we don't want to introduce any ionization in the ultrafast UV generation process. The nonlinear problem is limited, in turn, within the perturbation theory. So the third term in the propagation constant can be neglected. Then, from (3.17), the phase mismatch is

$$\Delta k_{nm}^{\mathrm{THG}} = \left[2\pi N_a\left(\frac{\delta_3}{\lambda_3}-3\frac{\delta_1}{\lambda_1}\right)\right] - \left[\frac{{\mu_{nm}}^2\lambda_3-3{\mu_{11}}^2\lambda_1}{4\pi a^2}\right] = \Delta k_{materil}^{\mathrm{THG}} - \Delta k_{mode}^{\mathrm{THG}} \tag{3.21}$$

where λ_3= 267 nm, λ_1= 800 nm, δ_3 and δ_1 are gas dispersion at 267 nm and 800 nm respectively. $\Delta k_{materil}^{\mathrm{THG}}$ is positive for normal dispersion, so in order to make phase matched, $\Delta k_{mode}^{\mathrm{THG}}$has to be positive as well, that is $\frac{{\mu_{nm}}^2}{{\mu_{11}}^2} > 9$. Therefore, the generated UV pulse has to

be in a mode μ_{nm} different from μ_{11} to make the phase matching happen. For example, the lowest order EH_{1m} mode fulfilling the relationship, $\frac{{\mu_{nm}}^2}{{\mu_{11}}^2} > 9$, is EH_{13} mode, and by properly choosing the neutral atomic density N_a in (3.21), which can be achieved by playing with the gas pressure P since $P \sim N_a$ for the ideal gas, THG could be phased matched in the waveguide. If phase matching happens and we neglect the absorption terms, (3.19) changes to

$$F_{3,nm}^{THG}(L) = i\beta_{nm}^{\mathrm{THG}}[F_1(0)]^3 L \tag{3.22}$$

So, the 3rd harmonic efficiency is mainly determined by the relevant nonlinear-optical cubic susceptibility $\beta_{nm}^{\mathrm{THG}}$. $\beta_{nm}^{\mathrm{THG}}$ is significantly affected by the mode matching as shown in the integration in (3.18). A simple calculation can show that $\beta_{11}^{\mathrm{THG}}$: $\beta_{13}^{\mathrm{THG}} \approx 50$. Therefore, unable to generate the beam in the same spatial mode as the pump and idler spatial mode in the phase matching condition significantly reduces the efficiency of THG in the hollow waveguide. The discussion so far is not limited only to the THG; any 3rd order SFG, say $\omega_1 + \omega_2 + \omega_3 = \omega_4$, has the similar phase mismatch relationship as in (3.21), then the normal material dispersion has to be balanced by the mode dispersion in the way of using the higher order mode to reach phase matching condition, so all 3rd order SFG have low efficiency due to the bad mode matching. (This problem might be solved by using PCF, see the section of future experiment).

FWM is proposed because it can satisfy the requirements of the phase matching condition and mode matching condition simultaneously. The FWM equation for the slowly varying envelope of the 267 nm light in the hollow waveguide is written as

$$\frac{d}{dz}F_{3,nm}^{FWM}(z) + \alpha_{3,nm}F_{3,nm}^{FWM}(z) = i\beta_{nm}^{FWM}[F_1(0)]^*[F_2(0)]^2\exp[-i\Delta k_{nm}^{FWM}z - (\alpha_{1,11} + 2\alpha_{2,11})z] \tag{3.23}$$

where the relevant nonlinear-optical cubic susceptibility is written as [88]

$$\beta_{nm}^{\mathrm{FWM}} = \frac{27\pi\omega^2}{k_{3.nm}c^2}\chi_{\mathrm{DFG}}^{(3)}\frac{\iint f_{3,nm}(r)[f_{1,11}(r)]^3 r dr d\theta}{\iint [f_{3,nm}(r)]^2 r dr d\theta} \tag{3.24}$$

and phase mismatch can be written as

$$\Delta k_{nm}^{\mathrm{FWM}} = \left[2\pi N_a\left(\frac{\delta_3}{\lambda_3}+\frac{\delta_1}{\lambda_1}-2\frac{\delta_2}{\lambda_2}\right)\right]-\left[\frac{{\mu_{nm}}^2\lambda_3+{\mu_{11}}^2(\lambda_1-2\lambda_2)}{4\pi a^2}\right]$$

$$=\left[2\pi N_a\left(\frac{\delta_3}{\lambda_3}+\frac{\delta_1}{\lambda_1}-2\frac{\delta_2}{\lambda_2}\right)\right]-\left[\frac{{\mu_{nm}}^2\lambda_3}{4\pi a^2}\right]=\Delta k_{materil}^{\mathrm{FWM}}-\Delta k_{mode}^{\mathrm{FWM}} \tag{3.25}$$

where λ_2 = 400 nm, $\delta_2$is gas dispersion at 400nm. $\Delta k_{materil}^{\mathrm{THG}}$ is positive for normal dispersion, and $\Delta k_{mode}^{\mathrm{THG}}$ is always positive for any mode μ_{nm}. So, by properly choosing the neutral atomic density N_a and $\mu_{nm}=\mu_{11}$, the phase matching condition and mode matching condition simultaneously. By using $P{\sim}N_a$ and equation (3.25), the phase matching condition can also be written as

$$P_{nm}a^2 = \frac{1}{8\pi^2}\left(\frac{{\mu_{nm}}^2\lambda_3}{\frac{\delta_3}{\lambda_3}+\frac{\delta_1}{\lambda_1}-2\frac{\delta_2}{\lambda_2}}\right)P_{atm} \tag{3.26}$$

where P_{atm} is the pressure of one atmosphere. Formula (3.26) means that the pressure times the area of the waveguide is a constant for certain mode. This relationship is important for future discussion. If phase matching happens and we neglect the absorption terms, (3.23) can be solved to be

$$F_{3,nm}^{FWM}(L) = i\beta_{nm}^{\mathrm{FWM}}[F_1(0)]^*[F_2(0)]^2 L \tag{3.27}$$

If we write (3.27) in terms of the input and output pulse energy, then,

$$W_3{\sim}W_2^2W_1L^2/a^4 \tag{3.28}$$

where W_1, W_2, W_3, are the pulse energy of the fundamental, 2nd and 3rd harmonic, respectively.

3.4 Ultrafast UV generation setup and results

The schematic diagram of the ultrafast UV generation is shown is the Figure 3.4. The 800 nm light is incident from the left. After the SHG BBO crystal, 20% of the pulse energy of 800 nm light will be converted into 400 nm light. A beam-splitter is used after the BBO to separate the 400 nm light from 800 nm light. There are two reasons for separating and recombining the 800 nm and 400 nm light beams before coupling them into the hollow waveguide. First, lenses of different focal length are used in 800 nm and 400 nm light beams respectively in order to optimize the mode coupling, because the waist size are proportional to the wavelength and focal length. Second, the pulse energy of the 800 nm light has to be reduced before the waveguide, since the pulse energy of 800 nm light needed for FWM is only a quarter of that of the 400 nm light and too much pulse energy would ionize the gas and violate the phase matching. This is achieved by using the combination of the half waveplate and polarizer beam in 800 nm light beam. The polarization of the 800 nm light could be controlled by them as well. After 800 nm light and 400 nm light are both coupled into the waveguide, by controlling the gas pressure inside and the time delay between 400 nm light and 800 nm light, pulse energy of the 267 nm light could be optimized. The output of the 267 nm light is compressed by an UV compressor, built by a pair of reflective gratings (300 rules/mm, 300-nm blaze, Al coating), whose throughput is 50 %. Then the pulse duration and spectral phase is characterized by a self-diffraction FROG [70].

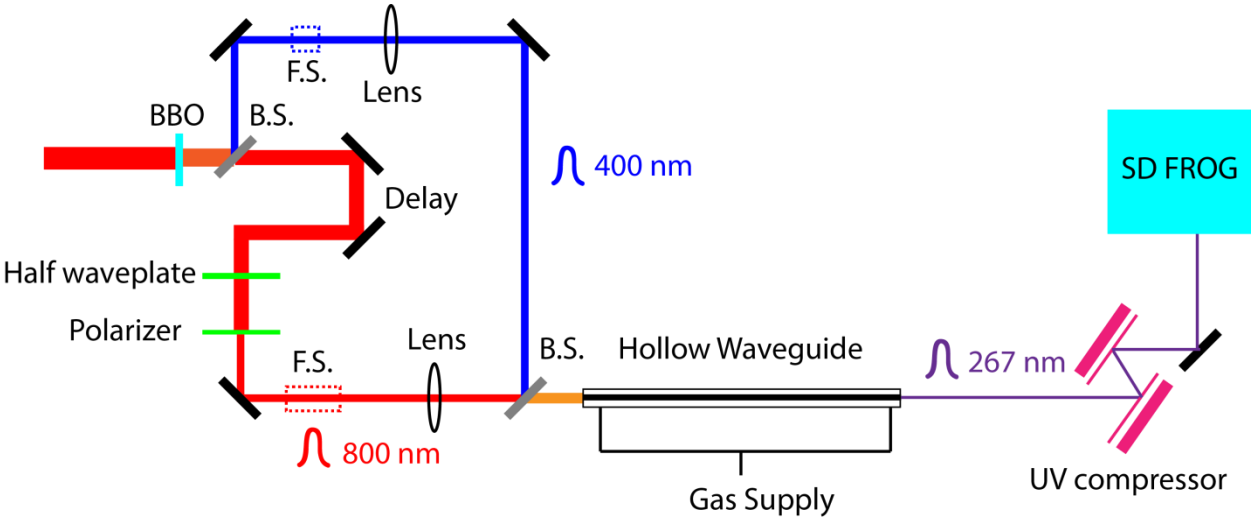

Figure 3.4 Diagram of the ultrafast UV generation in hollow waveguide.

In experiments, we have tested the hollow waveguides with diameters of 100 um, 150 um and 250 um, and with lengths of 20 cm and 100 cm in order to prove the theories in last section and find the optimized parameters for ultrafast UV generation. Noble gas argon (Ar) is supplied into the hollow waveguide as the nonlinear medium. Most features of the ultrafast UV generation are shown in the pressure scan of the throughput of UV (267 nm) as in Fig 3.5 (a), which is taken by using the hollow waveguide of 150 um diameter and 100 cm long.

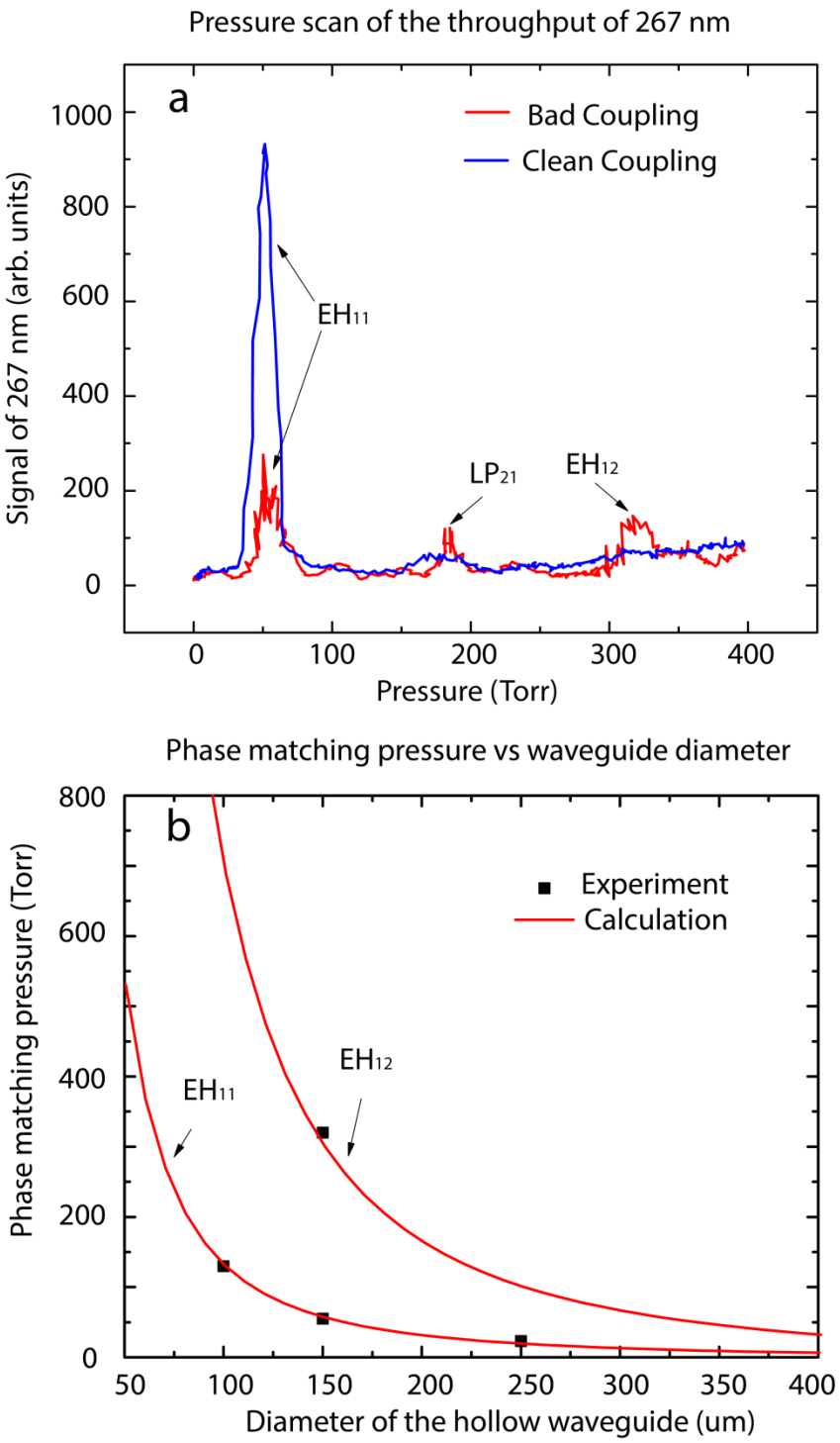

Figure 3.5 (a) The throughput of 267 nm light as a function of the gas pressure inside the hollow waveguide. (b) Phase matching pressure curve with respect to the diameter of the hollow waveguide and the output mode.

First, the efficient output of the 267 nm is only shown when the input light is coupled into hollow waveguide properly, that all energy of both 400 nm light and 800 nm light are distributed in the EH_{11} mode, and when the gas pressure is tuned to the phase matching pressure. This is a manifestation of the optimization of the mode coupling, phase matching and mode matching simultaneously. The results of the output pulse energy and pulse duration of the 267 nm light mentioned later is both taken under this condition. Second, when the mode coupling is clean, as shown in the blue curve, the 267 nm light is "only" phase matched at one mode, EH_{11}. This is because the mode matching between the phase-matched higher order signal modes and the pump and idler mode, EH_{11}, is too little, so that they don't show clear output in the pressure scan, although they could be phase matched. When the mode coupling is not clean as shown in the red curve, the 267 nm light can be phase matched at multiple modes in the pressure scan. This is because the coupled higher order modes of the pump light could help the higher order modes of 267 nm light to mode match with them. Therefore, some higher order modes of the 267 nm light can be generated. Third, the phase matching pressure of each mode can be directly obtained from the pressure scan. Combing the phase matching pressure, the mode number and the diameter of the hollow waveguide, the phase matching equation (3.26) can be proven, which is shown in Fig 3.5 (b). The red curve is calculated from (3.26), and the black dot is obtained from the pressure scan of the 267 nm throughput signal. The experimental results agree with theoretical prediction perfectly. This is a direct proof of the theories of mode coupling and phase matching mentioned in the last section.

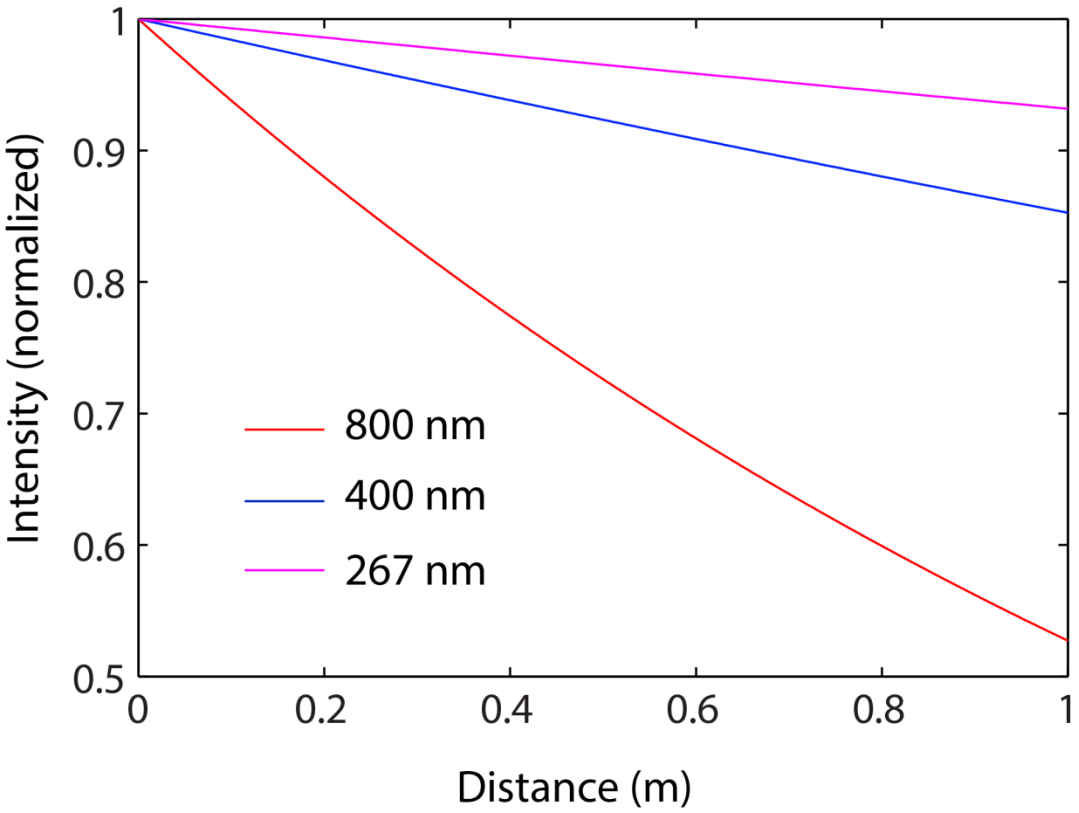

Figure 3.6 The decay of light intensity inside the hollow waveguide as a function of propagation distance. The lights of wavelength related to the FWM process are chosen in plots.

Having proven the theories, we are aiming for the high energy ultra-short UV pulse, which are coupled problems. We first compare the efficiency of UV generation for different lengths of the hollow waveguides. When we are using the 20 cm long waveguide, the coupling efficiencies of both 800 nm light and 400 nm light are both close to 60%. (The coupling efficiency is characterized as the throughput pulse energy after the waveguide divided by the input pulse energy before the fiber). The short interaction length limits the conversion efficiency from 400 nm light to 267 nm below 10 %. When we are using 1 m long fiber, the coupling efficiency of 400 nm light drops to 40% and the coupling efficiency of 800

nm light is even lower due large decay of the light at long wavelength (Fig. 3.6). However, the long interaction length improves the conversion efficiency to above 30% when the coupled energy of 400 nm light is below 20 uJ, and close to 20 %, when the coupled energy of 400 nm light is around the saturation energy, above which the ionization of the gas would greatly reduce the coupling efficiency and conversion efficiency so that more coupled 400 nm light won't generate more 267 nm light. Therefore, all the results below are based on the 1 m long waveguide. Then, we compare different diameter waveguides, and expect larger diameter waveguide would help to improve 267 nm output pulse energy. In principle, if we keep the coupled intensity the same (below the saturation intensity), we can get more pulse energy coupled into the bigger waveguide, and if the conversion efficiency is the same, then we can get higher 267 nm output pulse energy. However, since phase matching pressure is inversely proportional to the waveguide core area, when bigger waveguide is used, the phase matching pressure drops simultaneously, and the conversion efficiency drops as well. A brief explanation of this phenomena: If we assume the gas density is proportional to the pressure, then the number of gas atoms inside the waveguide is $N = n \times A \times L \sim P \times A \times L \sim L$, where n, A, L, P are gas density, core area, waveguide length and phase matching pressure respectively. So the number of UV emitters will not change under the phase matching condition by using the bigger waveguide of the same length. Therefore, using the bigger waveguide won't increase the output pulse energy efficiently, which is consistent with our experiment result. All the results below are based on the 150 um diameter hollow waveguide.

When we use input 800 nm light and 400 nm light both with pulse duration around 30 fs, which are un-chirped input beams, the maximum pulse energy of 267 nm we can obtain is 12 uJ, through a 150 um diameter, 1 m long, waveguide with noble gas Ar. In

order to obtain more pulse energy, we chirped both 800 nm light and 400 nm light to 100 fs by the fused silica rods (1 inch long for 800 nm light and 1 cm long for 400 nm light due to the different GVD), and the maximum output pulse energy of 267 nm increases to 32 uJ, which is more than 3 times of what people have got before [3.10]. Then, the questions are if the chirped 267 nm pulse compressible and how short it can be compressed (Here, we mean by using the conventional compressors such as grating pairs or prism pairs. The pulse shaper is not included).

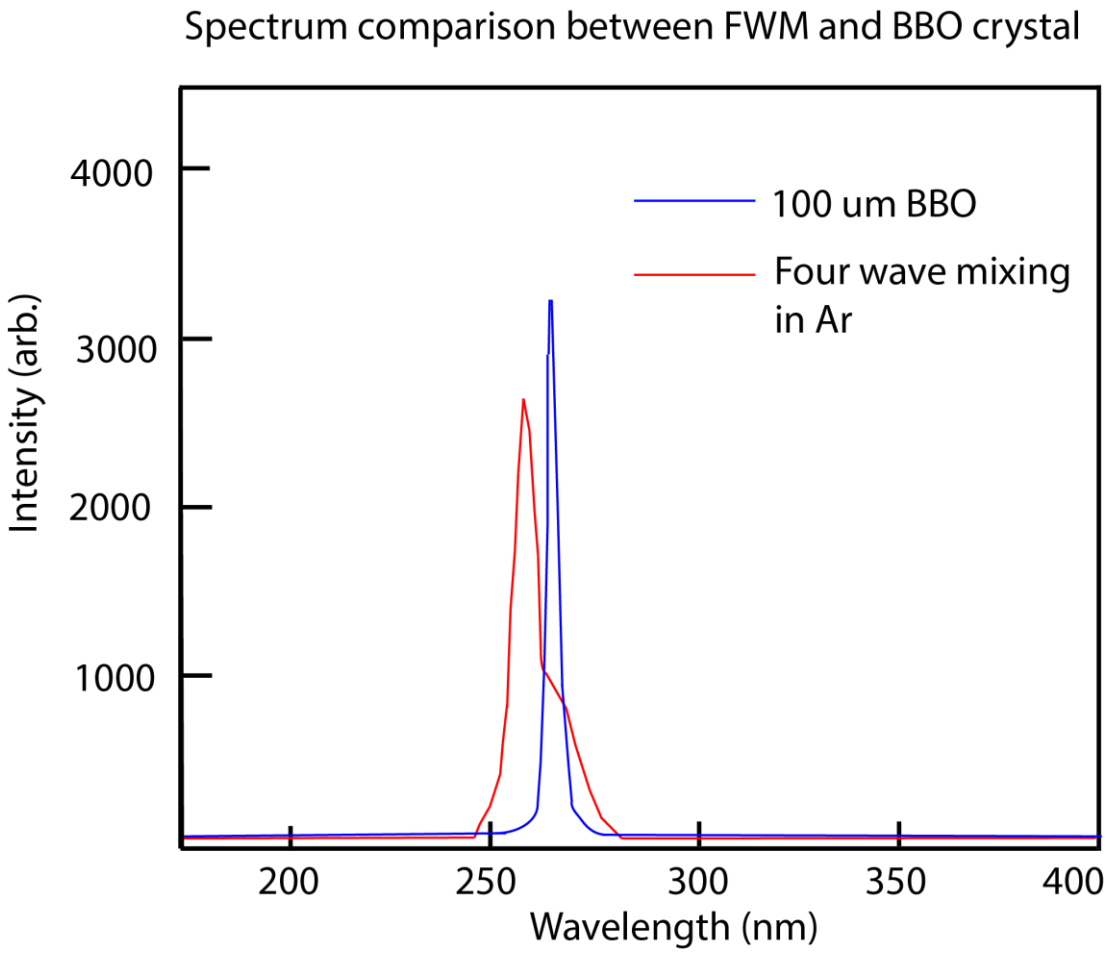

Figure 3.7 The spectrum comparison between the ultrafast UV light generated from the FWM process through hollow core fiber and the ultrafast UV light generated from the 100 um thick BBO crystal. The three times broaden spectrum from FWM implies that the pulse duration could be three times shorter than that from the crystal.

We first checked the spectrum of the output 267 nm light, since the width of the spectrum determines the transform limited pulse duration. As we can see from Figure 3.7, the bandwidth of spectrum of the 267 nm light from FWM through the hollow waveguide is about three times of that from a thin BBO crystal, which means the pulse duration of the 267 nm through hollow waveguide could be 3 times shorter than that from the crystal. (Here, we only showed the bandwidth at the high output pulse energy; actually we can sacrifice the output pulse energy to obtain broader bandwidth through self-phase modulation and cross-phase modulation, which have been demonstrated in our experiments.) Then, we characterized the pulse duration of the 267 nm light after the compressor built from a pair of aluminum gratings. By properly choosing the incident and angle and distance between the two gratings, the pulse could be compressed to around 10 fs (Fig 3.8), with an efficiency of 50 %. Therefore, we have generated ultra-short high energy UV pulse, achieving at least three times more pulse energy than before.

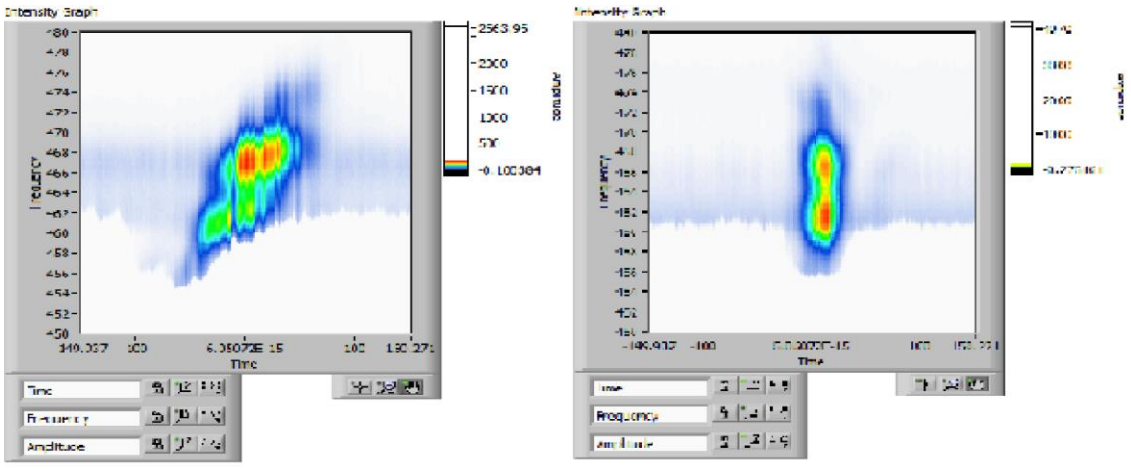

Figure 3.8 SD Frog traces of the chirped 267 nm pulse (left) and compressed 267 nm pulse (right). The SD autocorrelation is 13 fs, which implies the retrieved pulse duration is close to 10 fs.

3.5 Summary and future experiments

In this chapter, we first introduced the history and state-of-art techniques of the ultrafast UV generation. Then, we investigated the electromagnetic modes allowed in the hollow waveguide, since it is the basis of the mode coupling, mode matching and phase matching problems in the hollow waveguide. Then, we extensively discussed the model coupling, phase matching and mode matching problems in the ultrafast UV generation. It's worth noting that the knowledge of the mode coupling and mode matching apply to the high-order harmonics generation as well, which will be discussed in the next chapter. Finally, we verified the theory of the FWM phase matching in hollow waveguide and demonstrated the ultra-short (10 fs) high energy (32 uJ) UV pulse in experiments, achieving at least three times more pulse energy than before.

The future experiments are proposed:

First, keep improving the ultra-short UV pulse energy through FWM, and investigate the phase transfer problem. We have shown that, in order to increase the output pulse energy of UV light, we have to chirp the input pulse of 800 nm and 400 nm light. In principle, they should be chirped to the same pulse duration to optimize the temporal overlap. However, this would inevitably introduce the high order spectral phase. The reason is: from the mathematics of the Fourier transform, we know that the Fourier transform of a product is a convolution. Therefore, from equation (3.27), the spectral phase of the 3rd harmonic is the convolution of the spectral phase of the second harmonic and the complex conjugate of the spectral phase of the fundamental light. This means that, if one of the input lights has the flat phase (400 nm or 800 nm) and the other input light has the linear chirp, the 3rd harmonic would be linear chirped as well, the same sign as 400 nm

light if 400 nm light is the chirped one and the opposite sign to 800 nm light if 800 nm light is the chirped one. However, if 400 nm light and 800 nm light are originally having similar pulse durations, this will not be favored by the conversion efficiency; otherwise the pulse durations would differ a lot after one of them is chirped. So, in principle, the spectral phase of the 3rd harmonic is the convolution of three linearly chirped spectral phases, which has high order spectral phase. Therefore, at some point of chirping input pulses, the chirped 3rd harmonic won't be able compressed just by a pair of gratings or prisms. It may require both or even pulse shaper to compress it, although I believe the bandwidth of the spectrum is always there. Moreover, if we could control the phase transfer to obtain the negatively chirped UV output, we may just use materials to compress it.

Second, a more interesting experiment is to use the PCF to generate the ultrafast UV. The reason is that: Although the phase matching equation still holds due to the same boundary condition, the PCF would change the material dispersion from normal to abnormal [83]. Recall that, the reason that THG in hollow waveguide doesn't work is the material dispersion and the waveguide dispersion are in the opposite sign in equation (3.21) when the material dispersion is normal and all light have the same mode. If the PCF can change the sign of material dispersion, then THG can be phase matched with perfect mode matching. Therefore, the ultrafast UV generation scheme can be simplified from two input lights scheme to one input light scheme. Furthermore, PCF typically has very tiny core < 50 um, which would bring up the coupled intensity orders of magnitude higher if the input pulse energy keeps the same. On the other hand, if we keep the coupled intensity the same which is preferred by UV generation, we can use a lower pulse energy pump, such as a fiber laser. Then, we can obtain a high rep-rate ultrafast tabletop UV source.

Third, in order to obtain the VUV light, the cascaded processes in hollow waveguide could be utilized. Actually, the cascaded process happens simultaneously with the FWM

process, and efficiency is on the order of 10% [71-72]. We have generated the brightest ultrafast UV light which means the VUV light generated from the cascaded process is probably also the much brighter than before. However, the phase transfer problem as well as the conversion efficiency problem still needs to be investigated to optimize the VUV generation. Moreover, VUV generation could be the bridge between UV generation and high order harmonic generation. What's the physics there could be investigated as well.

Chapter 4

High flux soft X-ray generation by HHG

4.1 Introduction

High-order harmonics generation (HHG) describes the phenomena that harmonics result from a strong nonlinear interaction between the electric field of the incident laser pulse and the individual atoms, in which the perturbative nonlinear picture doesn't apply. The incident laser field simultaneously drives the nonlinear generation of harmonics in a large number of atoms or molecules all at the phase coherent with the incident laser field. Thus, resultant harmonics add in phase in the direction of the driving pulse, enabling the efficient high-order harmonics emission in a relatively narrow forward radiation cone [89]. The first observations of HHG date back to the late 1980s. In 1987, the 17^{th} harmonic (14.6 nm) was observed when the intense picosecond 248 nm light (3-10 mJ) was focused into noble gas neon (Ne) [90]. In 1989, the 33rd harmonic (32.2 nm) was observed when the strong 1064 nm light was focused into noble gas argon (Ar) [91]. In 1990s, due to the development of the femtosecond laser, especially the Ti:sapphire amplifier, the harmonics photon energy cutoff had been greatly increased [92]. When high ionization potential gas helium (He) was used, the cutoff reached the "water window" region [93]. The "new" ultrafast technique, self-phase modulation (SPM) [94], also provided the way to obtain the

ultra-short 800 nm driving pulse of 5 fs pulse duration, which enabled the water window harmonics as well with low driving pulse energy [95]. All works above were based on the tight focusing geometry using the gas jet. The short interaction lengths limited the HHG efficiency and coherence. In 1998, Andy Rundquist demonstrated the first fully phase matched HHG by using the hollow waveguide geometry [2]. The harmonic flux was increased by 100-1000 times compared to the previous tight focusing geometry, because the interaction distance was greatly increased while the fully phase matching HHG is maintained in the hollow waveguide. In the waveguide geometry, the fully spatial coherence of HHG was demonstrated as well, so the high harmonic (HH) beam became a "laser" like beam [3]. In order to increase the photon energy cutoff of HHG in the phase matching geometry, the quasi-phase matching scheme was proposed first [96-97]. Then, in 2008 Tenio Popmintchev proposed the new way to increase the cutoff by using driving pulse of the long wavelength [27]. Thanks to the recent development of the ultrafast optical parametric amplifier (OPA) and optical parametric chirped pulse amplification (OPCPA) systems, multi-mJ level infrared (IR) pulses are available [29-30]; and the fully phase matched water window harmonics has been demonstrated by using driving pulse of wavelength at 2 um [28], and the fully phase matched harmonics of photon energy up to 1.6 keV was implemented by using driving pulse of wavelength at 3.9 um [4].

The HHG spectrum is generally consisted of three regions: a steep decrease for the first few order harmonics, a plateau, and a sudden cutoff for highest few order harmonics, as shown in Fig. 4.1 [91]. Specifically (Fig. 4.1), in region I, the yield of the 3^{rd}, the 5^{th} and the 7^{th} harmonic drops fast at a rate as the perturbative nonlinear theory predicts. In region II, for harmonic orders from the 9^{th} to the 29^{th}, the harmonic yield keeps most a constant level, called the plateau which can't be explained by the perturbative nonlinear theory. In region III, harmonic yield drops dramatically from harmonic order of the 31^{th} to

the 35th, and almost disappears at the 35th harmonic order, which is called the harmonic cutoff. The corresponding photon energy is called the cutoff photon energy, which is 40 eV in this case.

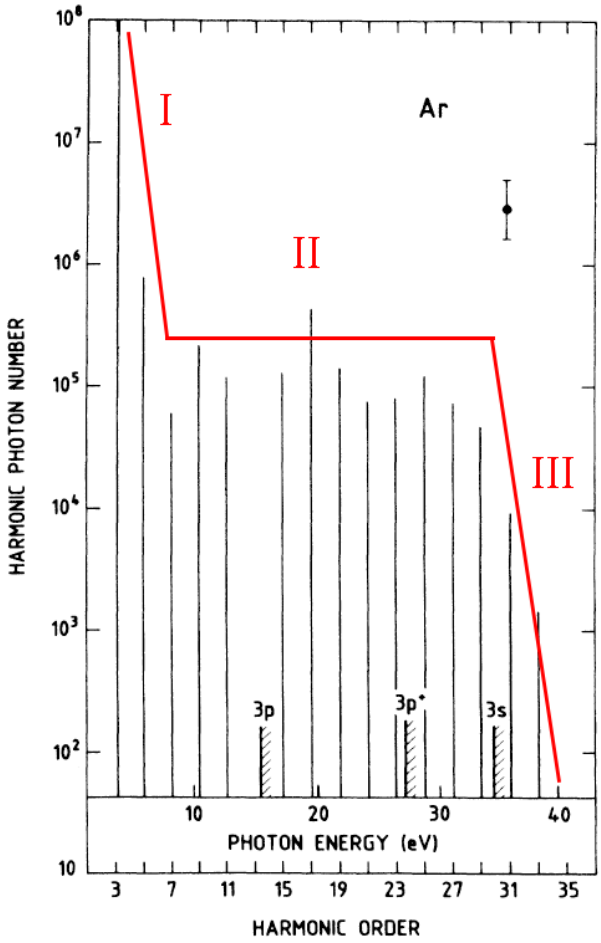

Figure 4.1 The general feature of the HHG spectrum. The spectrum is generated from noble gas Ar with intensity of at 3×10^{13} W/cm^2 at gas pressure of 15 Torr. Figure is captured from Ref. [91].

Simply speaking, the discussion of the HHG is focused on region II and III, and the researches of HHG source development could be considered as two groups: 1. increase the photon energy of the HHG cutoff so that broader spectrum could be achieved for applications; 2. demonstrate the shortest pulse from HHG since it is so far the only way to achieve the attosecond pulse which is the shortest event human beings can capture. Since the goal of our HHG development is to obtain high flux in soft X-ray region for real applications (chapter 5), in this chapter we will focus on the discussion of increasing HHG cutoff photon energy and the flux, which is implemented by using driving pulse of long driving wavelength and the fully phase matching geometry. We will discuss the physics in it in the next two sections and present our experiment results after that. The summary and future investigation is given finally.

4.2 Single atom picture of HHG

The physics process of HHG is classified into two categories. One is the single atom response of the noble gas in the intense laser filed. The other one is the macroscopic effect during the propagation of the harmonic fields in the noble gas as a dispersive and absorptive medium. We will discuss the single atom picture in this section first, because, it determines the theoretical limit of the photon energy cutoff of the HHG, which suggests to use longer wavelength driving pulse and higher driving intensity to obtain higher cutoff energy. However, it also brings up the problem that single atom yield of HHG scales to $\lambda^{-5.5\sim-6.5}$ in a certain bandwidth and constant laser intensity, which needs to be overcome by the macroscopic effect, the phase matching of HHG, that is to be discussed in the next section.

The most straight forward way to derive the photon energy cutoff of HHG is from a simple classical model called “three-step model” proposed by K. C. Kulander and P. B. Corkum in 1993 [98-99]. In this model, the whole HHG process is divided into three steps as shown in Fig. 4.2. First, when a linearly polarized strong laser field is focused into the gas atoms. It bends the coulomb potential, and the electron in the ground state may tunnel out to the free continuum state with initial velocity of zero. Second, the free electron is accelerated by the driving laser field and gains kinetic energy from it. Third, after the electric field reverses, the electron is accelerated in the opposite direction. It might return and recombine with the parent ion, back to the ground state of the atom. The excess kinetic energy it has gained during the travel in the laser field will be emitted as high energy photons, which are called high order harmonics. Despite the simplistic approach, the “three-step model” successfully explains the maximum photon energy, called single-atom HHG cutoff, which could be obtained in the HHG,

$$h\nu_{max} = I_p + 3.17U_p \approx I_l\lambda_l^2 \tag{4.1}$$

where I_p is the ionization potential and U_p represents the average oscillation energy of a free electron in the field, which is commonly called the ponderomotive potential, I_l and λ_l are driving laser’s intensity and wavelength.

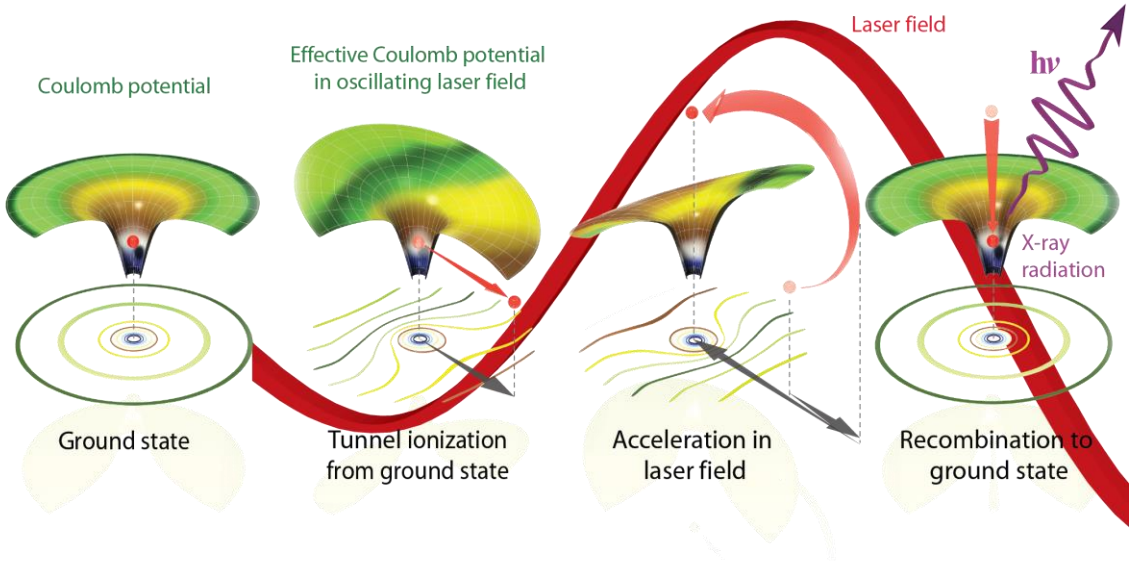

Figure 4.2 The cartoon of the classical schematic of HHG captured from Ref. [100]. The electric field of an intense laser extracts an electron from an atom through tunnel ionization. The laser field then accelerates the electron, with a small fraction of the electron returning back to the ground state of the same atom, liberating its excess energy as a high-energy photon.

We will use the classic model to obtain equation (4.1), and then use the quantum mechanics model from M. Lewenstein [101] to confirm this equation and explain the reason why the long wavelength driving HHG was not expected to have efficient throughput at the early age of HHG.

The first step of the "three-step model" is called the tunneling ionization. The ionization rate in tunneling ionization regime can be approximated by the Ammosov-Delone-Krainov (ADK) model [102]. Since the ionization rate is a critical factor in the phase matching of HHG, we will leave the detailed discussion of the ionization to the next section. In the quantum mechanics model from M. Lewenstein, it is described by a transition dipole moment from ground state to the continuum state as shown laser.

The second step of the "three-step model" directly determines the kinetic energy a free electron can gain from the laser field. Consider an electron tunneling out from ground state to continuum state at t_0 in the electric field $E = E_0\cos(\omega t)$, where the tunneling could be considered as instantaneous compared to the duration of the electron traveling in the laser field before recombining, the equation of the motion of the free electron follows the Newton's second law:

$$m\ddot{x} = F = -eE_0\cos(\omega t + \varphi_0) \tag{4.2}$$

where e is the electron charge, m is the electron mass, x is the displacement of the electron with respect to the parent iron, φ_0 is the initial phase with respect to the peak of the laser filed when the electron tunnels out at t_0. The laser field is assumed to be linearly polarized, so this is just a one dimensional second order derivative equation. With the initial condition that $x(t_0) = 0$ and $\dot{x}(t_0) = 0$ [101, 103], the solution of equation (4.2) is easily obtained

$$x(t) = \frac{eE_0}{m\omega^2}[\cos(\omega t + \varphi_0) - \cos(\varphi_0 + \omega t_0) + \omega(t - t_0)\sin(\varphi_0 + \omega t_0)] \tag{4.3}$$

Then, the kinetic energy is written as,

$$E_K(t) = \frac{1}{2}m\dot{x}^2 = \frac{1}{2}\frac{e^2E_0^2}{m\omega^2}[\sin(\omega t + \varphi_0) - \sin(\varphi_0 + \omega t_0)]^2$$

$$= 2U_p[\sin(\omega t + \varphi_0) - \sin(\varphi_0 + \omega t_0)]^2 \tag{4.4}$$

where $U_p = \overline{E_K} = \frac{1}{2}\overline{\dot{x}^2} = \frac{1}{4}\frac{e^2E_0^2}{m\omega^2} \sim I_l\lambda_l^2$ is the ponderomotive potential, I_l is the intensity of the laser, and λ_l is the wavelength of the driving laser. The chosen of t_0 is arbitrary, so we can set $t_0 = 0$. Then, the relationship of between the trajectory of the free electron $x(t)$ and the initial phase φ_0 is given by

$$x(t) = \frac{eE_0}{m\omega^2}[\cos(\omega t + \varphi_0) - \cos(\varphi_0) + \omega t \cdot \sin(\varphi_0)] \quad (4.5)$$

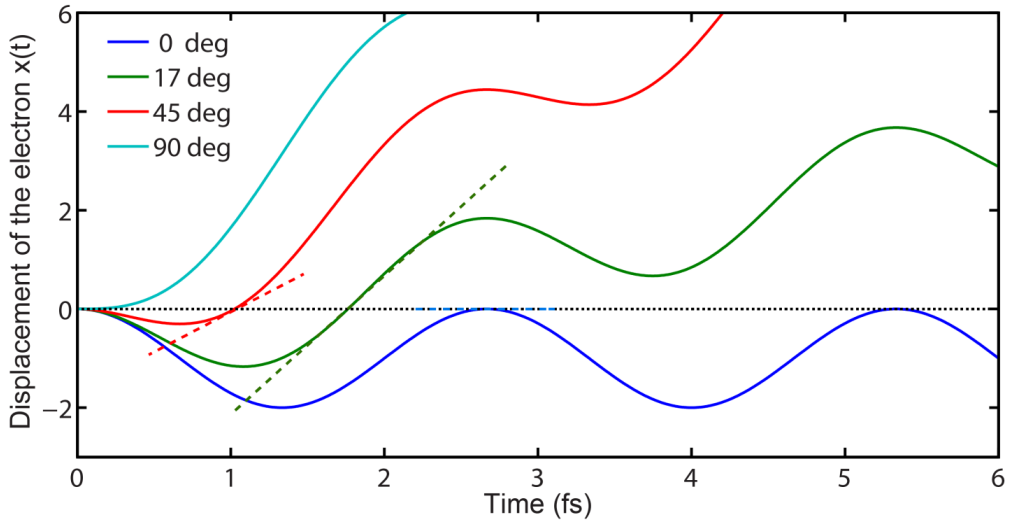

Figure 4.3 The electron trajectories of different initial phase with respect to the peak of the laser field at the tunneling time t_0. The driving laser is assumed to be at 800 nm. Y axis of the plot is in the unit of the ponderomotive radius, $a = \frac{eE_0}{m\omega^2}$.

A few trajectories of different initial phases φ_0 are plotted in Fig. 4.3 by equation (4.5). From the trajectories, we can see that: First, when $0^\circ < \varphi_0 < 90^\circ$, the electron could come back to its parent iron, which equals to $x(t) = 0$ has solution after t_0; when $90^\circ < \varphi_0 < 180^\circ$, the electron cannot come back. Second, the highest kinetic energy to be gained by an electron accelerated in the continuum can be determined by solving $x(t) = 0$ for various phases of the laser electric field. The slopes of the trajectories in Fig. 4.3 at $x(t) = 0$, labeled by the dashed lines, are indicatives of the velocity of the electron at the point of recombining with the ion core and therefore represents the kinetic energy available. From

numerical calculation, it is found that $3.17Up$ is the maximum kinetic energy to be acquired, which occurs when the electron has been ionized at a phase of the laser electric field of 17°. And this is the origin of the photon energy cutoff of HHG from the classical model. Third, from 0° to 17°, the gained kinetic energy is increasing and then falls off beyond an electric field phase of 17°. It means that there are two trajectories that may impart the same kinetic energy to the free electron ionized at the initial phase in opposite sides of the phase of 17°. Trajectories of the free electron acquiring the same kinetic energy are the so-called long and short trajectories, which are defined as $0^\circ < \varphi_0 < 17^\circ$ the long trajectory and $17^\circ < \varphi_0 < 90^\circ$ short trajectory that can be easily understood by their duration before the recombination.

The third step of the "three-step model" says the electron recombines with the parent iron, and the transition from continuum state to the ground state happens. Therefore, besides the gained kinetic energy from the laser field, the combining energy which is called the ionization potential I_p will also be emitted in the third step. So the maximum energy, cutoff, of the HHG is given by equation (4.1).

The classical model explains (4.1) in an elegant way, however, it doesn't show the quantum nature of the ionization, the quantum diffusion when the electron travels in the laser field and the recombination. Therefore, it can't explain the questions such as HHG single atom yield and HHG intrinsic phase. So we will follow quantum mechanics model from Lewenstein to recheck the whole process.

The Lewenstein model calculates the time-dependent dipole moment which is responsible for the HHG. The electric field is calculated from the second derivative of the dipole. Finally, a Fourier transform reveals the spectrum. Derivation of this model begins with the Schrödinger equation in the length gauge

$$i\frac{\partial}{\partial t}|\psi(\vec{x},t)\rangle = [-\frac{1}{2}\nabla^2 + V(\vec{x}) - E\cos(t)x]|\psi(\vec{x},t)\rangle \tag{4.6}$$

where, $V(\vec{x})$ is the molecular potential and $E\cos(t)$ is the laser field. Next, in writing the wavefunction, several approximations are made. First, only the ground bound state $|0\rangle$ is considered. Second, depletion of the ground state is neglected. U_p should be large enough, so that $U_p \geq 2I_p$, but still below the saturation level, U_{sat}, when all atoms ionize during the interaction time. So the ionization is in the tunneling regime. Third, in the continuum, the electron can be treated as a free particle moving in the electric field with no effect of $V(\vec{x})$. Mathematically, it is expressed as

$$\langle \vec{v}|\vec{x}|\vec{v}\rangle = i\nabla_v \delta(\vec{v} - \overrightarrow{v'}) \tag{4.7}$$

where the continuum-continuum transitions are rewritten to reflect only the most singular part. $|\vec{v}\rangle$ represents the continuum state of velocity $\vec{v}$. Then, the wavefunction can be written as

$$|\psi(\vec{x},t)\rangle = e^{iI_p t}[a(t)|0\rangle + \int d^3\vec{v}\, b(\vec{v},t)|\vec{v}\rangle] \tag{4.8}$$

where $a(t) \approx 1$ is the ground state amplitude and $b(\vec{v},t)$ is the amplitude of the continuum state. Insert (4.8) into (4.6) and consider (4.7), $\langle 0|\vec{v}\rangle = 0$, as well as $x = i\frac{\partial}{\partial v_x}$ in the momentum representation. The Schrödinger equation for $b(\vec{v},t)$ reads as

$$\frac{\partial}{\partial t} b(\vec{v},t) = -i\left(\frac{1}{2}v^2 + I_p\right) b(\vec{v},t) - E\cos(t)\frac{\partial}{\partial v_x} b(\vec{v},t) + iE\cos(t)\, d_x(\vec{v}) \tag{4.9}$$

where $\vec{d}(\vec{v}) = \langle \vec{v}|x|0\rangle$ denotes the atomic dipole matrix element for the bound to free transition and $d_x(\vec{v})$ is the component parallel to the polarization axis. The solution to equation (4.9) is

$$b(\vec{v},t) = i\int_0^t dt' E\cos(t')\, d_x[\vec{v} + \vec{A}(t) - \vec{A}(t')] \times \exp\left\{-i\int_{t'}^t dt'' \left[\frac{1}{2}(\vec{v} + \vec{A}(t) - \vec{A}(t'))^2 + I_p\right]\right\} \tag{4.10}$$

where $\vec{A}(t) = (-E\sin(t), 0, 0)$ is the vector potential of the laser field. Using equations (4.8) and (4.10), the x-component of the dipole moment is

$$x(t) = \langle \psi(t)|x|\psi(t)\rangle = \int d^3\vec{v}\; d_x^*(\vec{v}) b(\vec{v}, t) + c.c. \tag{4.11}$$

Using the canonical momentum $\vec{p} = \vec{v} + \vec{A}(t)$, dipole moment becomes

$$x(t) = i\int_0^t dt' \int d^3\vec{p}\, E\cos(t')\, d_x\left(\vec{p} - \vec{A}(t')\right) d_x^*(\vec{p} - \vec{A}(t))\exp[-iS(\vec{p}, t, t')] + c.c. \tag{4.12}$$

where

$$S(\vec{p}, t, t') = \int_{t'}^t dt'' \left\{\frac{1}{2}[\vec{p} - \vec{A}(t'')]^2 + I_p\right\} \tag{4.13}$$

Equation (4.12) shows the quantum mechanics version of the three-step model. $E\cos(t')\, d_x\left(\vec{p} - \vec{A}(t')\right)$ describes ionization at time t' as the step 1. The electronic wave function is then propagated until the time t and acquires a phase factor equal to $\exp[-iS(\vec{p}, t, t')]$, where $S(\vec{p}, t, t')$ is the quasiclassical action, as the step 2. This phase is called the intrinsic phase of HHG. (The effects of the atomic potential are assumed to be small between t' and t based on the assumption 3, so $S(\vec{p}, t, t')$ actually describes the motion of an electron freely moving in the laser field with a conserved canonical momentum $\vec{p}$, although it does incorporate some effects of the binding potential through its dependence on I_p.) Finally, the recombination at time t is described by $d_x^*(\vec{p} - \vec{A}(t))$, as the step 3.

Since $\tau = t - t'$ is of the order of one period of the laser field which as in Fig 4.3, the quasiclassical action varies much faster than the other factors entering Eq. (4.12). Therefore, the major contribution to the integral over $\vec{p}$ in Eq. (4.12) comes from the stationary points of the classical action

$$\nabla_{\vec{p}}\, S(\vec{p}, t, t') = 0 \tag{4.14}$$

Considering $\nabla_{\vec{p}}\, S(\vec{p}, t, t') = \vec{x}(t) - \vec{x}(t')$, equation (4.14) just means the most the dominant contribution to the harmonic emission comes from the electrons which tunnel away from the nucleus but then reencounter it while oscillating in the laser field, which is actually the assumption of the three-step model. By (4.14), the integral over $\vec{p}$ in Eq. (4.12) might be performed using a saddle-point method. The result is

$$x(t) = i\int_0^\infty d\tau \left(\frac{\pi}{\varepsilon + \frac{i\tau}{2}}\right)^{\frac{3}{2}} d_x^*\big(p_{st}(t,\tau) - A_x(t)\big) d_x\big(p_{st}(t,\tau) - A_x(t-\tau)\big)\, E\cos(t-\tau)\exp[-iS_{st}(t,\tau)] + c.c. \tag{4.15}$$

where $p_{st}(t,\tau) = E[\cos(t) - \cos(t-\tau)]/\tau$ is the stationary value of the component of the momentum in the direction the of the polarization of the laser field. The value of the quasiclassical action in Eq. (4.15) is given by

$$S_{st}(t,\tau) = \frac{1}{2}\int_{t-\tau}^{t} dt''\big(p_{st} - A(t'')\big)^2 = \big(I_p + U_p\big)\tau - \frac{2U_p[1-\cos(\tau)]}{\tau} - U_p C(\tau) \times \cos(2t-\tau) \tag{4.16}$$

where

$$C(\tau) = \sin(\tau) - 4\sin^2\left(\frac{\tau}{2}\right)/\tau \tag{4.17}$$

The Fourier transform of the dipole moment $x(t)$ gives the spectrum of the HHG. We don't go further than this, since (4.16) and (4.17) already show the cutoff energy and single-atom HHG field for our interests. More detailed derivation could be found [101].

First, in equation (4.16), we can see that $C(\tau)$ determines the variation of $S_{st}(t,\tau)$ as a function of t in the unit of U_p. Since the action $S_{st}(t,\tau)$ is the integral of the kinetic energy over t'', the maxima of $C(\tau)$ correspond to the maxima of the kinetic energy gain of the electron at t. The detailed derivation shows that the maximum of $2\,C(\tau)$ in the unit of U_p is

the maximum kinetic energy, and maximum of $2\,C(\tau)$ is 3.17. So from the quantum model, we can obtain the same HHG cutoff as the result obtaining from the classical model.

Second, from the first factor in equation (4.15), we can see that the dipole moment $x(t)\sim\tau^{-3/2}$, so the single atom yield of HHG is proportional to τ^{-3}. Since $\tau\sim\lambda$, it means the single atom yield of HHG is proportional to λ^{-3} as well. However, this is just count from something called from quantum diffusion from free electron. An additional λ^{-2} factor arises from the conversion factor from photon number to energy since HHG cutoff is scaled by λ^2. Totally, the single atom yield of HHG is scaling around λ^{-5}.

More precise theoretical solutions of the time dependent Schrodinger equation (TDSE) showed slightly worse scaling factor of $\lambda^{-5.5}$ [104-106], and Shiner et al. experimentally obtained an even worse scaling factor of $\lambda^{-6.5}$ [107]. These results mean that, when the driving wavelength is doubled, the single-atom harmonic yield is expected to be decreased by 50-100 times. Although the longer wavelength driving pulse is expected to produce more energetic harmonics, the lower single-atom yield "seems" to be the problem. However, all things considered so far are based on the single-atom response. In the next section, we'll show that the phase matching could compensate low single-atom yield by the increase of the gas pressure-length product and transparency in the case of longer driving wavelength.

4.3 Phase matching HHG in hollow waveguide

The macroscopic effect of HHG could be considered as the generation and the propagation of the high-order harmonics from the fundamental light in the noble gas as a dispersive and absorptive medium. Assuming the harmonics are all propagating in the z

direction, under the slowly varying envelope approximation (SVEA), the wave equations of the fundamental light and qth order harmonic can be written as,

$$\Delta_{\perp} E_l(r,t) + 2ik_l(r,t)\frac{\partial E_l(r.t)}{\partial z} = 0 \tag{4.18}$$

$$\Delta_{\perp} E_q(r,t) + 2ik_q(r,t)\frac{\partial E_q(r,t)}{\partial z} = -\frac{q^2\omega_l^2}{\varepsilon_0 c^2} P_q^{NL}(r,t)\exp(iqk_l - ik_q)z \tag{4.19}$$

where $E_l(r,t)$and $E_q(r,t)$ represent the slowly varying amplitude of the fundamental light and qth order harmonic propagating in the gas medium with wave vectors of k_l and k_q respectively. $P_q^{NL}(r,t)$ is the nonlinear polarization of the gas medium, which should calculated by the quantum mechanics instead of assuming to be proportional to $[E_l(r,t)]^q$ as in the perturbation theory. If we confine the discussion in the z-direction and neglect the spatial variation in the x-y plane, (4.19) can be written as

$$\frac{dE_q(r,t)}{dz} = \frac{i\mu_0 q^2\omega_l^2}{2k_q} P_q^{NL}\exp\left[i\left(qk_l - k_q\right)z\right] = \frac{i\mu_0 q^2\omega_l^2}{2k_q} P_q^{NL}\exp[i\Delta kz] \tag{4.20}$$

where Δk is the phase mismatch between the fundamental light and qth order harmonic. From (4.20), we can see that as the fundamental light propagates long z direction, it ionizes the atoms at position z which generate the qth order harmonic of spatial phase of qk_lz, coherent with the fundamental light at z. After being generated, the qth order harmonic has its own propagation speed, associating with the spatial phase of k_qz which might be different from the spatial phase of the fundamental light qk_lz. Therefore, the de-phasing between the fundamental light and qth order harmonic in propagation limits the nonlinear macroscopic HHG efficiency. The maximum conversion efficiency from the fundamental light to the macroscopic high-order harmonic yield happens when the phase matching HHG, $\Delta k = 0$, could be maintained over long enough distance before touching the limit set by the

reabsorption of the high-order harmonic field from the medium. Equivalently, it means that the high-order harmonic light should travel at the same speed as the fundamental light in the dispersive medium over enough distance.

Just based on the discussions of HHG phase matching so far, we can compare the different geometries that have been used for HHG. Typically, there are two types of geometries being used for HHG: tight focusing geometry and plane wave geometry. As shown in Fig. 4.4 (b), the tight focusing geometry causes a large Gouy phase shift through the focus, which is particularly problematic for HHG because of the large difference in wavelength and divergence of the harmonics compared with those of the driving laser [108]. Although, by considering the intrinsic phase as an effective additional wave vector added to the overall phase matching of the HHG process, the interplay between Gouy phase and intrinsic phase could enable the phase matching happen at some point, for example, when the gas jet is placed at the position where the laser is slowly diverging from the focus, the Gouy phase induced phase mismatch could be compensated by the intrinsic phase [109-110], the short confocal length would limit the interaction distance since the laser intensity drops fast beyond confocal length, which in turn would change the ionization rate or plasma generation, an critical factor in phase matching problem as shown later. Therefore, the conversion efficiency in the tight focusing geometry is low although it is relatively easy to be implemented.

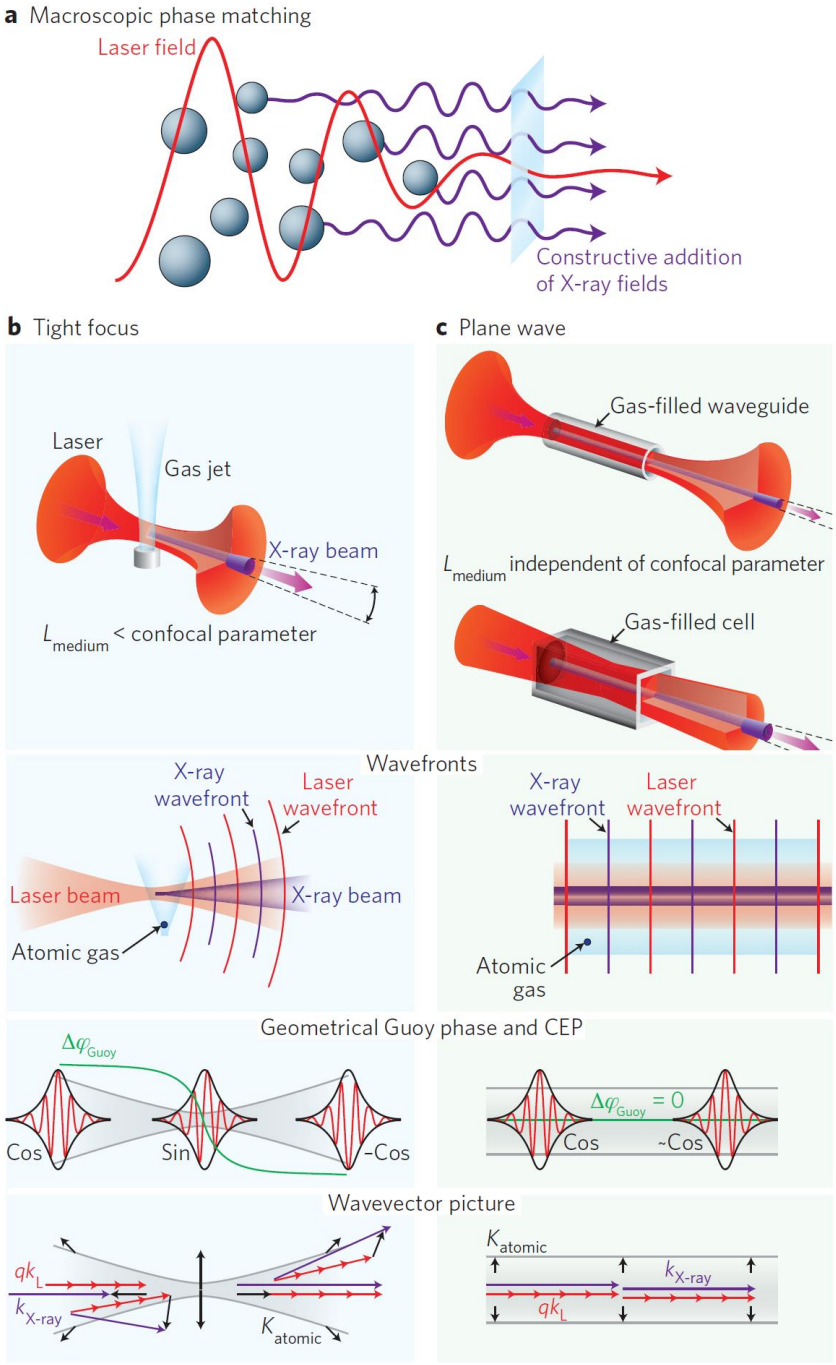

Figure 4.4 Physical pictures of HHG phase matching in different geometries. (a) Phase-matched signal growth ensures that harmonic emission from many atoms adds together coherently over an extended medium. (b) The tight focusing geometry is associated curved laser and X-ray wavefronts, which limits the phase matching distance within the confocal length and has to deal with the problem of Guoy phase shift. (c) The waveguide or cell geometry minimizes the curvature of the laser and HHG wavefront. The nearly plane wave propagation allows long distance phase matching HHG and has no Guoy phase or Carrier-Envelope phase (CEP) problem. The Figure is captured from Ref. [100]

Contrarily, the plane wave geometry maintains the phase matching condition over an extended distance, making it possible to build up a fully spatially coherent and fully phase-matched high-harmonic beam (Fig. 4.4 (c)). Especially, by using the hollow waveguide geometry, the guided mode ensures the near plane-wave propagation of the driving beam, maintaining a flat uniform phase and high peak intensity over a large interaction distance, avoiding any variation in the intrinsic quantum phase. The waveguide also makes it straightforward to create a region of controlled, confined and well-characterized gas pressure, with optimal differential pumping at the entrance and exit of the waveguide. This feature is more critical for achieving absorption-limited phase matched HHG flux for longer driving wavelengths, since the high-pressure gas medium together with an abrupt transition to vacuum becomes increasingly important as the HHG driving laser wavelength is increased. Therefore, we will focus on the phase matching HHG in the hollow waveguide geometry in the following discussion, and this is consistent with the discussion in the ultrafast UV generation.

The near-plane-wave geometry can also be realized using a large focus and high laser energy when the confocal parameter of the beam is much longer than the gas medium. Such a high-energy HHG geometry has been effectively used in experiments that benefit from high peak power rather than high repetition rate. However, considering the application end, the high repetition rate is always preferred, so we will not discuss it in the following paragraph.

We have extensively discussed the modes inside the hollow waveguide in Chapter 3. The wave vector (real part of the propagation constant) of mode EH_{nm} is given by (3.20) as

$$k_{nm} = \frac{2\pi n(\lambda)}{\lambda}\left[1 - \frac{1}{2}\left(\frac{\mu_{nm}\lambda}{2\pi a}\right)^2\right] \approx \frac{2\pi}{\lambda} + \frac{2\pi N_a \delta(\lambda)}{\lambda} - N_e r_e \lambda - \frac{{\mu_{nm}}^2 \lambda}{4\pi a^2} \tag{4.21}$$

where N_a is the neutral atomic density, $\delta(\lambda)$ contains the gas dispersion function, N_e is the neutral atomic density, and r_e is the classic electron radius. So, the wave vector is the sum of four sources of dispersion: vacuum, gas, free electrons (plasma), and waveguide. In contrary to the UV generation, HHG has to be associated with the ionization as described by the three-step model, so the third term can't be neglected in HHG. If we assume the driving laser is coupled properly into the hollow waveguide mode EH_{11} and the ionization fraction of the gas is $\eta(t)$, then, the wave vector of the driving laser is

$$k_l \approx \frac{2\pi}{\lambda_l} + \frac{2\pi P\Delta n}{\lambda_l}\,[1-\eta(t)] - P\,\eta(t)N_{atm}r_e\lambda_l - \frac{{\mu_{11}}^2\lambda_l}{4\pi a^2} \tag{4.22}$$

where P is the pressure of gas in the waveguide, Δn is the difference between the refractive index of the gas at specific driving wavelength at one atmosphere and the refractive index of vacuum, which is one. N_{atm} is the gas density at one atmosphere. Obviously, we have used the same relationship that P~N as in Chapter 3 to obtain (4.22). For the wave vector of the qth order harmonic, considering the phase velocity of the high harmonics is close to the speed of light in vacuum because the refractive index for high photon frequencies (far above most atomic resonances) is close to unity, it could be written as,

$$k_q \approx \frac{2\pi q}{\lambda_l} - P\,\eta(t)N_{atm}r_e\frac{\lambda_l}{q} \tag{4.23}$$

Here, we neglect the waveguide term for two reasons: first, the HHG is very sensitive to the ionization, the ionization is stronger at the center of the hollow waveguide than close to the boundary, so it hard to describe it in a single mode; second, when we consider it as $\frac{{\mu_{nm}}^2\lambda_l}{4\pi a^2 q}$, it is only $\frac{1}{q^2}$ of the sum of wave-vectors of the fundamental waveguide terms. If the mode number is not huge (which doesn't make sure because of the mode matching), this term

should be very small. So, the phase mismatch of HHG in qth order harmonic in the hollow waveguide geometry is

$$\Delta k(t) = -k_q + qk_l \approx P\left\{q\frac{2\pi\Delta n}{\lambda_l}\left[1-\eta(t)\right] - (q-\frac{1}{q})\eta(t)N_{atm}r_e\lambda_l\right\} - q\frac{{\mu_{11}}^2\lambda_l}{4\pi a^2} \tag{4.24}$$

The physics explanations of equations (4.22), (4.23) and (4.24) are: from (4.23), the high harmonic travels at a speed close to the speed of light in vacuum, although it is slightly off by the plasma term and waveguide term; from (4.22), the speed of the fundamental light is reduced by the normal dispersion from the neutral gas and increased by the waveguide dispersion and plasma dispersion. The change of speed is quite dynamic, depending on the ionization induced by the driving pulse; from (4.24), in order to make phase matching happen, the modified speed of the fundamental light should be the same as the speed of the high harmonic, which is close to the speed of light in vacuum. And since the speed of the fundamental light dynamically depends on the ionization $\eta(t)$, from (4.24), phase matching actually requires the term in the braces to be positive which sets the upper limit of $\eta(t)$, called critical ionization level η_c. Below the critical ionization level, phase matching is possible, and higher ionization fraction is preferred since the ionized atoms are the real emitters of high harmonic, while, above the critical ionization level, phase matching is impossible and no macroscopic harmonic emission would happen.

From the discussion above, we can see the critical ionization level η_c play an importance role in the phase matching. From now on, we will show it actually sets the photon energy cutoff of HHG in the phase matching condition. From (4.24), the critical ionization level is given by

$$\eta_c = \left[\left(\frac{\lambda_l^2 r_e N_{atm}}{2\pi\Delta n}\right)\left(1-\frac{1}{q^2}\right)+1\right]^{-1} \tag{4.25}$$

when $q \gg 1$, equation (4.25) can be approximated to be

$$\eta_c \approx \left(\frac{r_e N_{atm}}{2\pi\Delta n}\right)^{-1} \lambda_l^{-2} \tag{4.26}$$

From (4.26), the critical ionization level monotonically decreases as the driving laser wavelength increases. Put the parameters Δn of specific gas species and driving wavelength as well as the numbers of r_e and N_{atm} in Eq. (4.26), we can see that the values for η_c are on the order of a few percent in the near-IR region, approximately 4% for Ar, 1% for Ne, and 0.5% for He, respectively, at driving laser wavelengths of 0.8 um and decreased to about 0.01% in the mid-IR region. Since Δn changes by only less than 1% when the wavelength changes from near-IR region to mid-IR region, equation (4.26) can be approximately written as

$$\eta_c \sim \lambda_l^{-2} \tag{4.27}$$

The plot of η_c with respect to the driving laser wavelength λ_l for noble gases Ar, Ne, and He are shown in Fig 4.5. (a) [27].

After obtaining the values of the critical ionization level in phase matching HHG, the further and more important question is what's the maximum intensity we can use in HHG? On one hand, since the critical ionization level sets the upper limit of the ionization fraction in phase matching condition, if the driving intensity is too high, it will over-ionize the atoms and exceed the critical ionization level, so the high harmonics can't coherently build up; on the other hand, we always want to have as much ionization as allowed by the phase matching, since the ionized particles are real emitters. Although the low driving intensity allows phase matching (see chapter 3), the no-emitters' phase matching means no high harmonic, which actually changes back to the theory in Chapter 3. Therefore, in

principle, to obtain efficient high harmonics, we want to apply the driving intensity right below what would introduce the ionization associated with the critical ionization level.

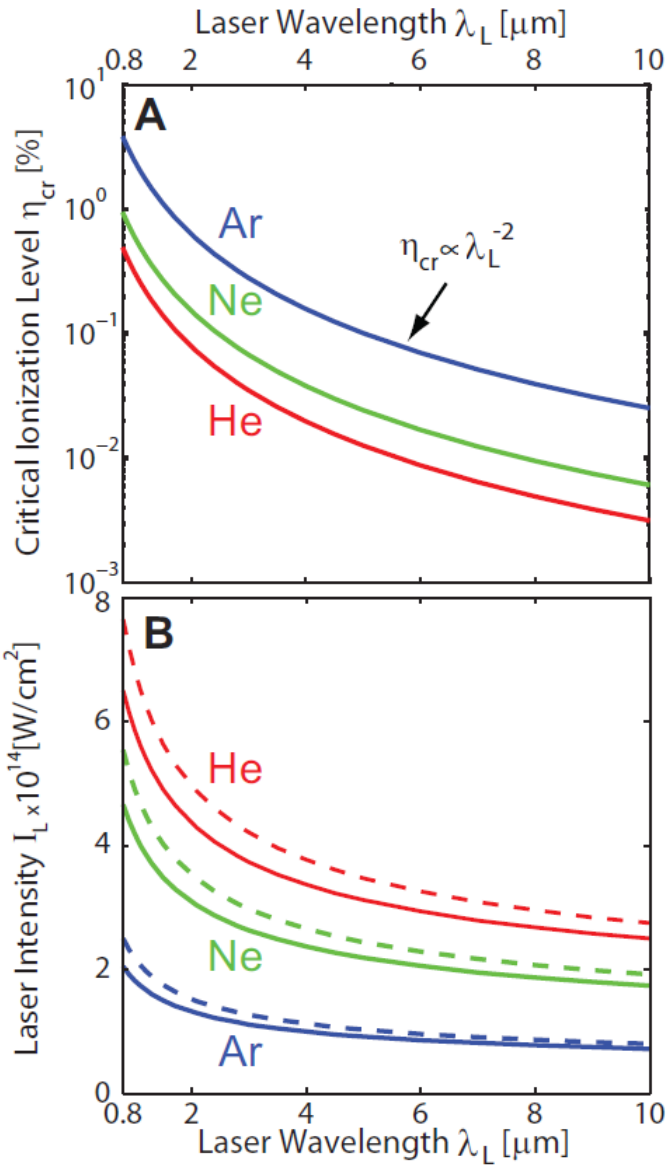

Figure 4.5 (a) Critical ionization levels for the noble gas Ar, Ne and He as a function of the driving laser wavelength. (b) Predicted laser intensity required to reach the critical ionization level at the peak of the laser pulse on axis (solid line), and when modal averaging is taken into account (dashed line). These figures are captured from Ref. [27].

Moreover, this intensity will determine the phase matching cutoff of HHG. In the sing-atom response, we have seen that the $h\nu_{max,single\_atom} \approx I_l\lambda_l^2$, which means the single atom HHG cutoff can be scaled by both the laser intensity and the laser wavelength; they are both free parameters. However, in the phase matching HHG, at specific wavelength, the critical ionization level determines the maximum intensity we can use, so the intensity is no longer a free parameter. In order to get the matching cutoff of HHG, we have to find the relationship between I_l and λ_l, then put it into the single-atom formula to obtain the new cutoff formula, which should have only one free parameter.

To obtain the maximum intensity the critical ionization level allows at specific wavelength, we need to treat the ionization more carefully. Generally, the ionization could be categorized as multiphoton ionization and tunneling ionization by Keldysh parameter γ, defined as $\gamma = \sqrt{I_p/2U_p}$ [4.30]. When $\gamma < 1$, the ionization is described by the multiphoton ionization, and When $\gamma > 1$, the ionization is described by the tunneling ionization. The detailed discussion on the photon-ionization is beyond the content of this thesis. V. S. Popov reviewed the photon-ionization in a strong laser field in Ref. [111]. Here, from our experiment data as shown in Fig. 4.6, we can see that the photoelectron momentum distribution in the multiphoton ionization is more isotropic, and photoelectron momentum distribution in the tunneling ionization is more linearly parallel to the polarization of the laser field. Obviously, HHG favors the tunneling ionization since the ionized electrons have to recombine with the parent iron. So, we will restrict the ionization process in the tunneling region.

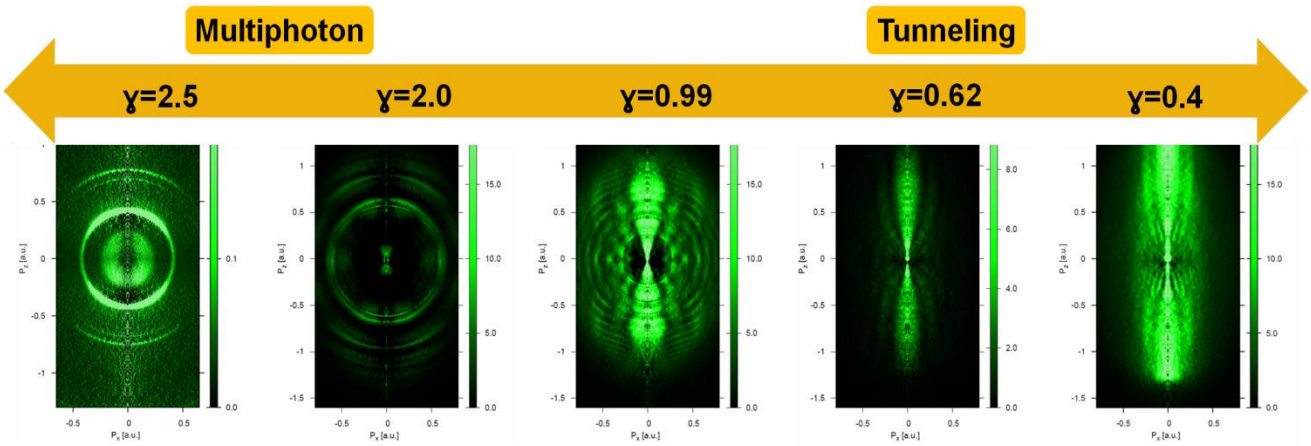

Figure 4.6 Photoelectron momentum spectra of the Xe ionization with respect to the Keldysh parameter γ.

In the tunneling region, the ionization of an atom is well described by the ADK tunneling ionization model, particularly for the longer wavelength driving lasers. The ADK ionization rate is given by

$$w_{ADK} = \sqrt{\frac{3E_l}{\pi(2I_p)^{\frac{3}{2}}}}|C_{n^*l^*}|^2 f(l,m) I_p \left(\frac{2(2I_p)^{\frac{3}{2}}}{E_l}\right)^{\left(\left(\frac{2z}{\sqrt{2I_p}}\right)-|m|-1\right)} \exp\left(-\frac{2(2I_p)^{\frac{3}{2}}}{3E_l}\right) \tag{4.28}$$

where Z is the ion charge, E_l is the E-field of driving laser, and l and m represent the angular momentum and magnetic quantum number, respectively. Factors $C_{n^*l^*}$ and $f(l,m)$ are given by

$$|C_{n^*l^*}|^2 = \frac{2^{2n^*}}{n^*\Gamma(n^*+l^*+1)\Gamma(n^*-l^*)} \tag{4.29}$$

$$f(l,m) = \frac{(2l+1)(l+|m|)!}{2^{|m|}(|m|)(l-|m|)!} \tag{4.30}$$

where $n^* = Z(2I_p)^{-1/2}$ and $l^* = n^* - 1$.

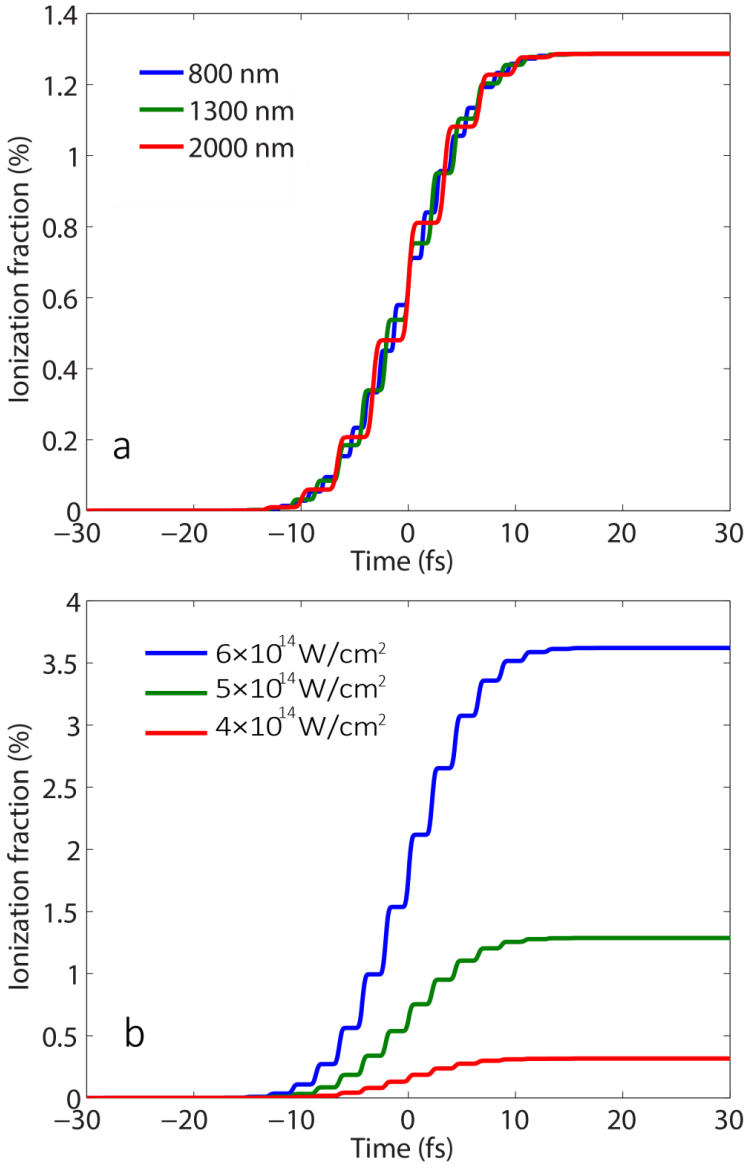

Figure 4.7 (a) The ionization fraction of gas neon in a 30 fs Gaussian shaped pulse with peak intensity of 5×10^{14} W/cm^2. The wavelength of the pulse is changed from 800 nm to 1300 nm to 2000 nm. Although the ionization step changes due to the different cycle duration, the ionization rates as a function of time almost keep the same for different driving wavelength. (b) The ionization fraction of gas neon in a 30 fs Gaussian shaped pulse with wavelength at 1300 nm. The peak intensity changes from 6×10^{14} W/cm^2 to 4×10^{14} W/cm^2. Ionization fraction changes more than an order of magnitude with the intensity change. If the intensity drops to 3×10^{14} W/cm^2, the ionization faction will be reduced to 0.05%, another order of magnitude lower, which is not easily seen in this plot. Thus, 50% of intensity change would introduce orders of magnitude change of the ionization fraction.

From ADK model, we can demonstrate that the tunneling ionization rate in HHG is almost wavelength independent, while strongly depends on the laser intensity (Fig. 4.7). Considering these two points, we can find the driving laser intensity required to reach the critical ionization level decreases slightly as the driving wavelength increases (Fig. 4.5 (b)). As a result, the phase matching HHG cutoff scales approximately as

$$h\nu_{PMC} \sim \lambda_l^{1.6-1.7} \tag{4.31}$$

The relationship is shown in Fig. 4.8 and has been demonstrated by the experiments [100].

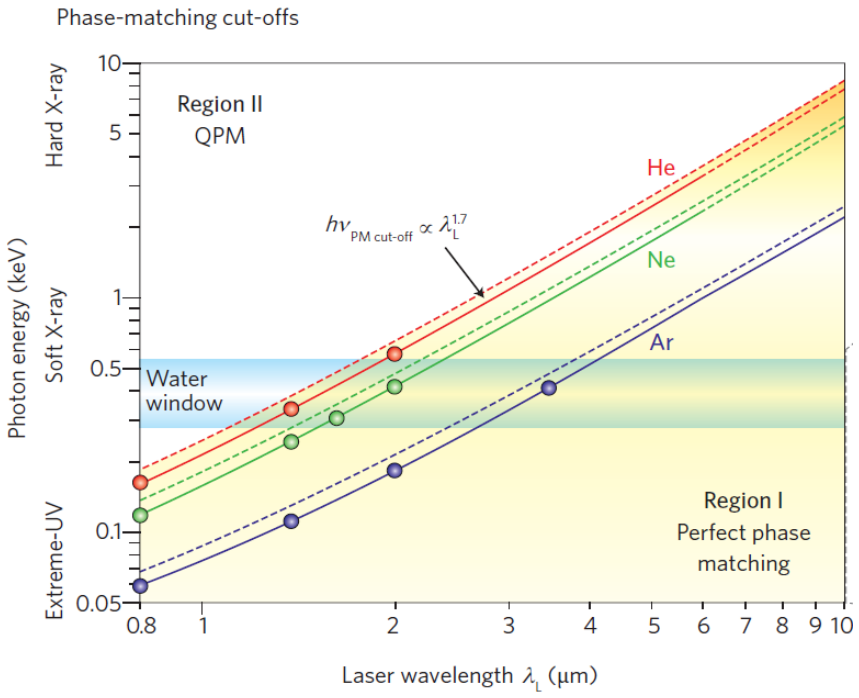

Figure 4.8 Theoretical HHG phase matching cutoff as a function of driving laser wavelength for three-cycle (dashed lines) and eight-cycle (solid lines) pulses. This global phase matching picture has been validated experimentally (solid circles) using several laser wavelengths and nonlinear media. The figure is adapted from [100].

From equation (4.31), although the freedom of scaling up the HHG cutoff by driving laser intensity is restricted by the requirement of the phase matching condition, the phase matching HHG cutoff still could be scaled up by the increase of the driving laser wavelength. People have known that the HHG cutoff from 800 nm driving laser is limited less than 150 eV. Therefore, in order to obtain bright soft X-ray light (> 100 eV), using longer driving wavelength is proposed.

The last question is whether the phase matching process could help the HHG to balance the low single-atom yield at long driving wave length, since the single atom response is scaled as $\lambda^{-5.5}$ or even worse. From E. Constant's semi-analytical model, for the qth harmonic, the number N_{out} of photons emitted on axis per unit time per area is [112]:

$$N_{out} \sim \rho^2 A_q^2 \frac{4L_{abs}^2}{1+4\pi^2(L_{abs}^2/L_{coh}^2)}\left[1+\exp\left(-\frac{L_{med}}{L_{abs}}\right)-2\cos\left(\frac{\pi L_{med}}{L_{coh}}\right)\exp\left(-\frac{L_{med}}{L_{abs}}\right)\right] \tag{4.32}$$

where ρ is the gas density, A_q is the is the amplitude of the single atom response at the harmonic frequency ω_q. The absorption length is $L_{abs} = 1/\rho\sigma$, where σ is the ionization cross-section, and coherent length is $L_{coh} = \pi/\Delta k$. From this model, we can have a few insights to the HHG flux from long wavelength driving pulse.

First, the asymptotic behavior of N_{out} can be obtained by assuming the phase matching is achieved so $L_{coh} = \infty$ and the gas medium length (hollow waveguide length) $L_{med} \gg L_{abs}$. Under the assumptions, the asymptotic behavior of (4.32) is

$$N_{out} \sim A_q^2/\sigma^2 \tag{4.33}$$

From equation (4.33), we can find that, although N_{out} would decrease due to the single atom response at long driving wavelength, the absorption cross-section tends to decrease at long wavelength as well. So, from asymptotic behavior, if we can extend the harmonic

emission to the photon energy region that the absorption is much lower than the EUV region. The decrease from single atom response might be balanced by the decrease of the reabsorption.

Second, combining Eq. (4.24) and (4.26), and considering the critical ionization level at long wavelength is typically less than 1%, the phase matching pressure around the critical ionization level is

$$P_{PMC} \sim \lambda_l^2 \tag{4.34}$$

It means the phase matching pressure is much higher when we use long driving wavelength, typically from 1 atm to 80 atm when the wavelength change from 1300 nm to 4000 nm.

Third, from Eq. (4.31), there is another important result: in order to approach the asymptotic behavior, $L_{coh} \geq 10L_{abs}$ and $L_{med} \geq 6L_{abs}$ are required. Since the absorption cross-section greatly reduces at the high energy region, the L_{abs} increases significantly. For example, close to keV region, for gas He, it requires a medium length as large as tens of centimeters to approach the asymptotic value [27].

In summary, by using the long driving wavelength, it requires a long interaction distance with high pressure. It means the hollow waveguide geometry is the best choice in experiment to achieve the high photon flux. The large pressure length product in hollow waveguide geometry would make the photon emission from HHG to the asymptotic value in Eq. (4.33), where the reduction of absorption might balance the low single atom yield. Finally, we cite Tenio Popmintchev's prediction of the HHG flux from Ref. [27] to thank his contribution to the long wavelength driving HHG.

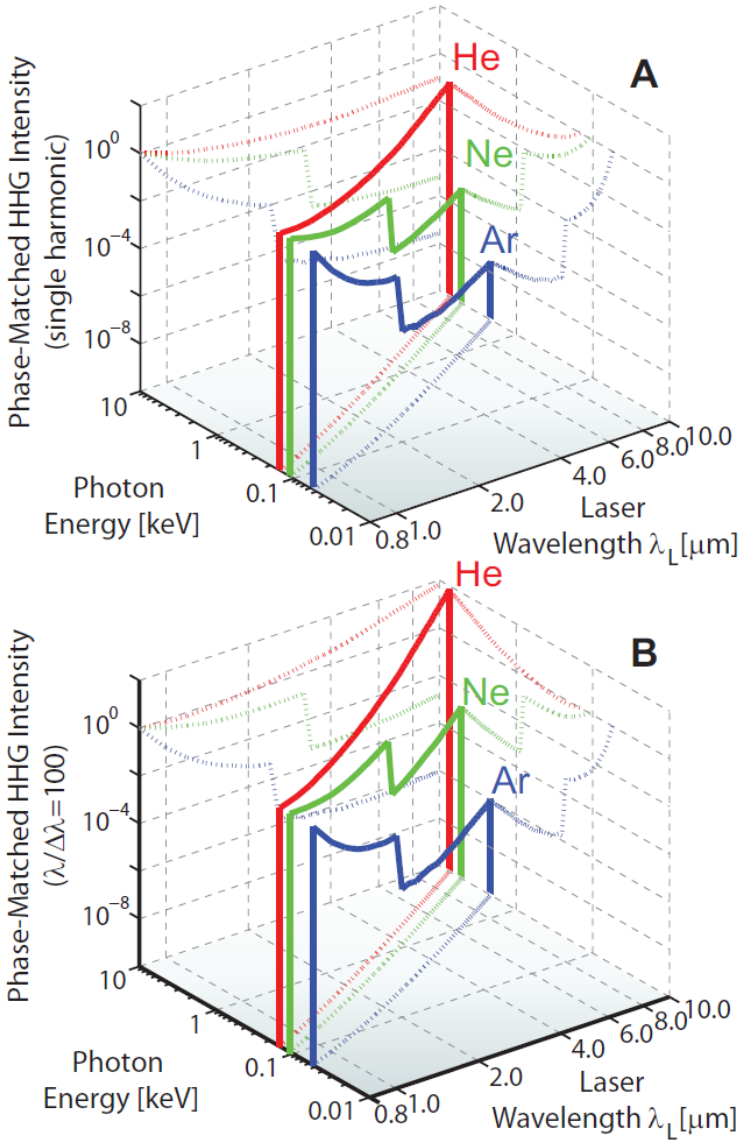

Figure 4.9 Absorption-limited intensity of phase-matched HHG in a bandwidth corresponding to a single harmonic (A) and a linewidth of 1% bandwidth (B) at the phase-matching cutoffs for laser wavelengths between 0.8 um and 10 um. The curves are normalized to the phase-matched HHG emission at 0.8 um.

4.4 Experiment setup and results

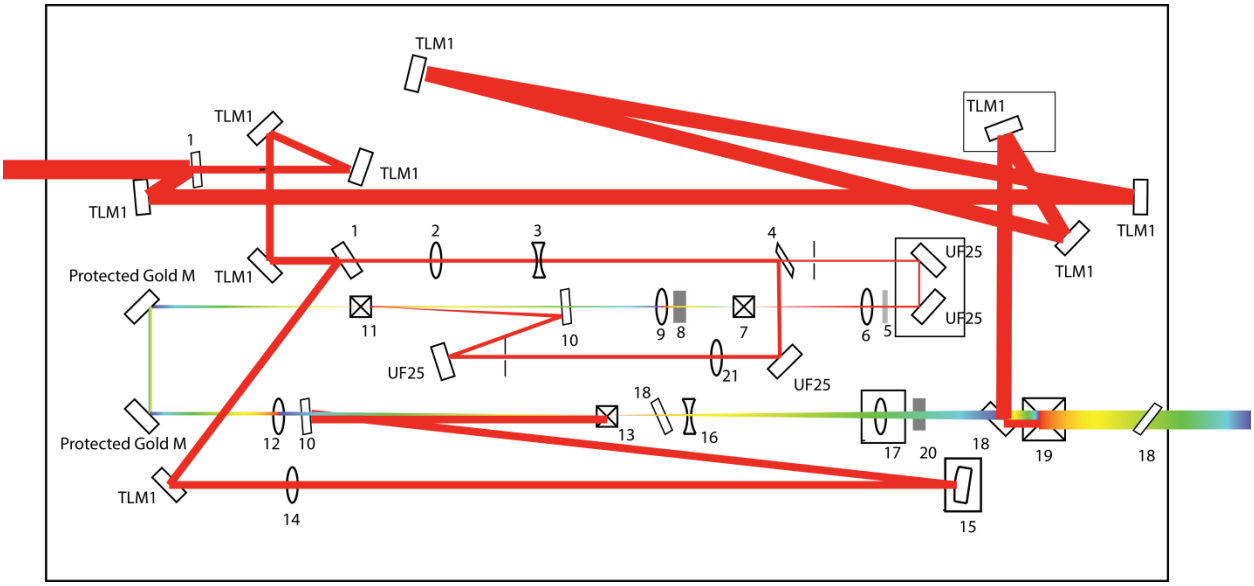

Figure 4.10 Schematic diagram of the high energy high efficiency OPA.

As discussed in the last two sections, the scheme of high flux soft X-ray generation has two steps: first, using OPA to obtain the longer driving wavelength at 1.3 um; second, using the hollow waveguide geometry to generate the fully phase matching high-order harmonic. Then, the characterization of the soft X-ray flux is done by using the soft X-ray spectrometer and CCD Camera. The details are showing bellow.

A homebuilt 3-stage OPA that achieves greater than 40% conversion of the 0.8 μm light into 1.3 μm (signal) and 2 μm (idler) beams to are used to obtain the high-quality 1.3 μm pulses to drive soft X-ray HHG (Fig 4.10). Type II BBO crystals are used as the nonlinear crystals in the OPA to amplify the seed from the white light generation process. The reasons for using Type II BBO are: First, compared to the type I phase matching, type

II phase matching reduces the effect from the group velocity mismatch, which enable a much longer interaction distant compare to the splitting length defined by the group velocity mismatch, so it gives a higher conversion efficiency (Fig. 4.11 (a)). Second, although the type I phase matching allows broader phase matching bandwidth, which supports shorter pulse duration, the tunability of the output wavelength is much worse than type II phase matching (Fig. 4.11 (b)). Since the HHG cutoff is determined by the driving wavelength, the tunable driving wavelength would make the generated soft X-ray from HHG also tunable in photon energy, which has great practical importance. So we decided choose the Type II BBO, aiming for high conversion efficiency and high tunability other than the ultra-short pulse duration. Crystal thicknesses of 2.5 mm, 2.0 mm and 1.5 mm were used in the first, second and the third OPA stage respectively.

The high energy OPA design is the standard one used by many groups worldwide, similar for example to the HE-TOPAS from Light Conversion. Due to the excellent beam quality of the high-energy regenerative amplifier, very high conversion efficiency of 40% is possible in the OPA. For these measurements, the total pulse energy used to drive the OPA was 8.5 mJ. In the first stage, 1% of the pulse energy is used for white light generation and the first stage pump. The second stage uses 9% of the pulse energy as the pre-amplification pump, while 90% of the pulse energy is used to pump the final stage. The output OPA signal pulse energy is 2.25 mJ, with a spectral full-width of greater than 200 nm centered at 1.3 μm. The pulse energy of the idler is 1.4 mJ, giving a total conversion efficiency in the OPA from pump to signal plus idler of approximately 43%. The good coupling of the OPA mode into our soft x-ray waveguide and resultant record soft x-ray flux (discussed in the following section) demonstrates that the OPA mode is of high quality, and indeed was the motivation for the new regenerative amplifier design. Additionally, the broad spectrum of the 1.3 μm light originates from white light generation, and supports an ultrashort pulse

duration of 30 fs (characterized by a second harmonic FROG measurement) (Fig.4.12). As expected in parametric down-conversion of multi-cycle ultrafast pulses, this signal pulse duration is considerably shorter than the 45 fs 0.8 μm pump pulse.

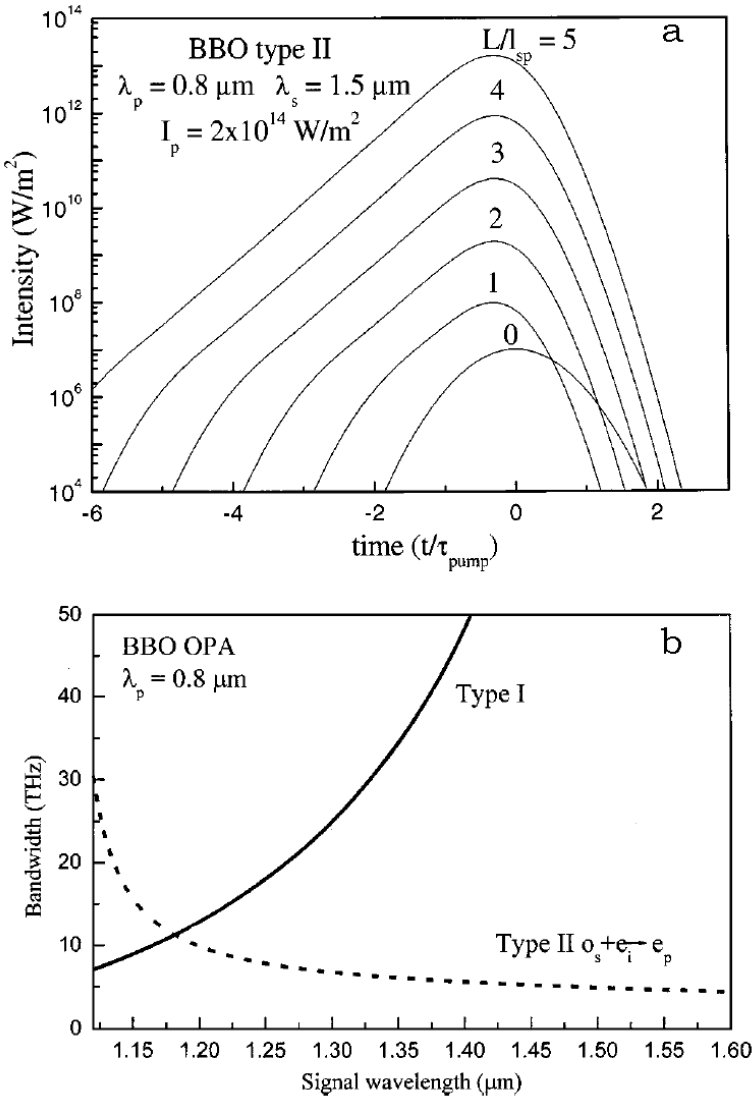

Figure 4.11 (a) Signal pulse evolution for a BBO type II OPA, with pump wavelength of 800 nm and signal wavelength of 1500 nm, for different lengths L of the nonlinear crystal. (b) Phase matching bandwidth for a BBO OPA at the pump wavelength of 800 nm for type I phase matching (solid line) and type II phase matching (dashed line). Figures are captured from Ref. [30].

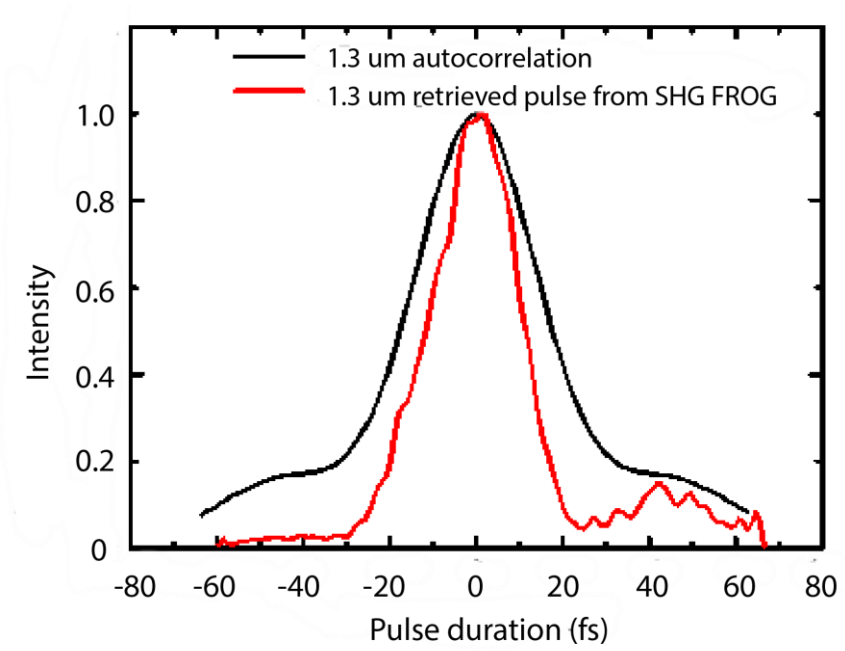

Figure 4.12 Pulse characterization of 1.3 um from OPA by the SHG FROG. The pulse duration of 1.3 um light is 29.6 fs, which is shorter than the pulse duration of the pump pulse.

Bright soft X-ray harmonics are generated by focusing the 2 mJ pulse energy, 1.3 μm, OPA signal output into a gas-filled hollow waveguide (length 1 cm and diameter 150 μm) using an f = 25 cm lens. The coupling efficiency is more than 50% - even with high pressure gas in the waveguide, so that the driving pulse peak intensity inside of the waveguide can reach 5×10^{14} W/cm^2, with the energy well coupled into an EH_{11} mode. The waveguide is filled with Argon (Ar) or Neon (Ne) to generate the soft X-ray. Since each noble gas has a different refractive index and ionization potential, each gas optimizes at a different phase matching pressures and laser intensity, and also extends efficient HHG to some maximum phase matched photon energy cutoff. By controlling the gas pressure inside the waveguide and the 1.3 μm pulse energy before the waveguide, we can optimize the

HHG flux at the phase matching pressure, as shown in Fig. 4.13. For a 1 cm long, 150 μm diameter waveguide and 1.3 μm driving lasers, the optimized pulse energies, phase matching pressures and phase matching cutoff photon energies are 0.95 mJ, 700 torr and 110 eV for Ar, and 1.6 mJ, 1300 torr, and 200 eV for Ne. By accounting for the absorption of the metal filters, the efficiencies of the spectrometer (Hettrick Scientific), and the quantum efficiency of the CCD camera (Andor, Inc.), the photon flux of the harmonics is estimated at more than 10^6 photons/pulse in 1% bandwidth up to 200 eV (Fig. 4.13), corresponding to 10^9 photons/s in 1% bandwidth at kHz repetition rates. This photon flux represents an approximately 3 orders of magnitude increase compared with past work (which used lower repetition rates or non-phase matching geometry). Additionally, a long term stability test demonstrates that the HHG flux is stable over many hours, limited primarily by beam pointing drift (when no beam pointing stabilization is used).

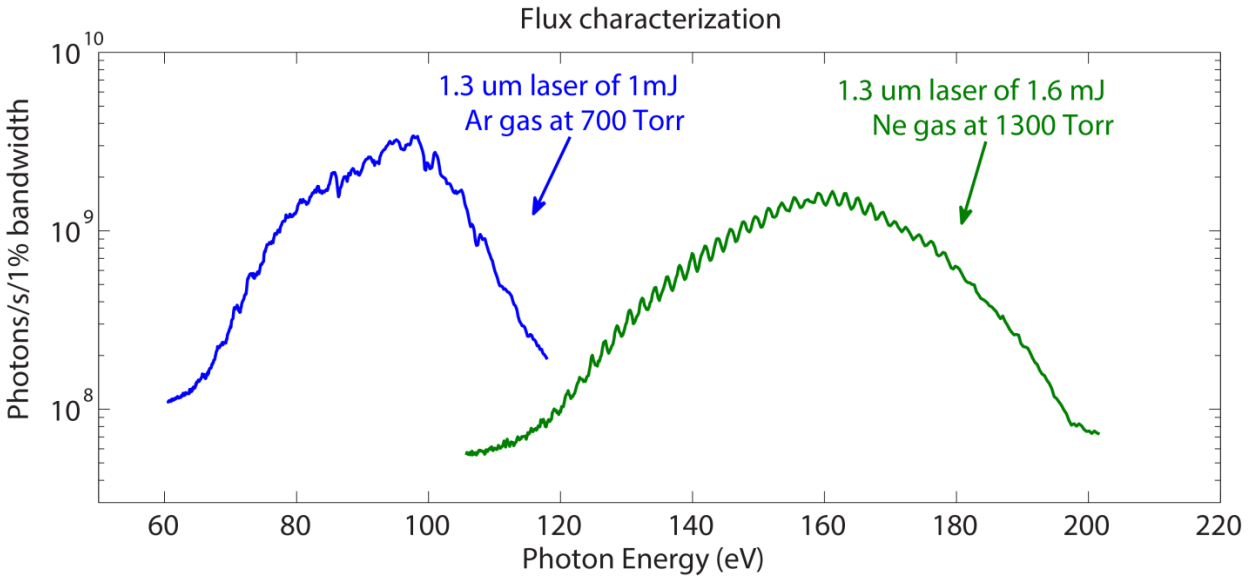

Figure 4.13 Flux characterization of the optimized fully phase matched HHG emission from a 1 cm long, 150 μm diameter with driving wavelength of 1.3 um. Noble gas Ar and Ne are used.

Since numerous experiments have been implemented utilizing 0.8 μm-driven EUV harmonics, we compared the optimized fully phase matched HHG flux driven by 0.8 μm light with the HHG flux driven by 1.3 μm light. We used the same waveguide for comparison, since the geometry and quality of the waveguide might affect the harmonic yield. The pulse energy used for the 0.8 μm-driven HHG from Ar, Ne, and He is 0.40 mJ, 1.5 mJ and 2.2 mJ, respectively. We find that at 100 eV photon energy, the 1.3-μm-driven HHG flux is within a factor of two of the flux of 0.8 μm-driven HHG, while above 150 eV, the 1.3 μm HHG flux becomes much more efficient. This shows that many applications based on EUV harmonics can now be extended to the soft X-ray region. Although our laser/OPA system did not provide sufficient pulse energy to generate fully optimized phase-matched HHG flux from He, we were in-fact able to generate coherent light up to ~300 eV from He. However, the HHG flux obtained was significantly lower (by ~100x) than the data of Fig. 4.14, which still represents a record HHG flux of 10^7 photons/s in 1% bandwidth at 300 eV, at kHz repetition rates. We predict that a further modest increase in pulse energy (by $\lesssim$2x) will allow us to generate flux comparable to that of Fig. 4.14 up to the water window using He as the nonlinear medium.

Finally, it is worth noting that high harmonics peak to peak modulation is much shallower when driven by 1.3 um than driven by 800 nm. The spectroscopic study (next chapter) also demonstrates that harmonic spectrum using Ne gas is a true coherent broadband supercontinuum - an observation which is consistent with other recent work demonstrating that phase matched soft X-ray HHG driven by mid-infrared lasers naturally emerges as an isolated, attosecond-duration, burst [113].

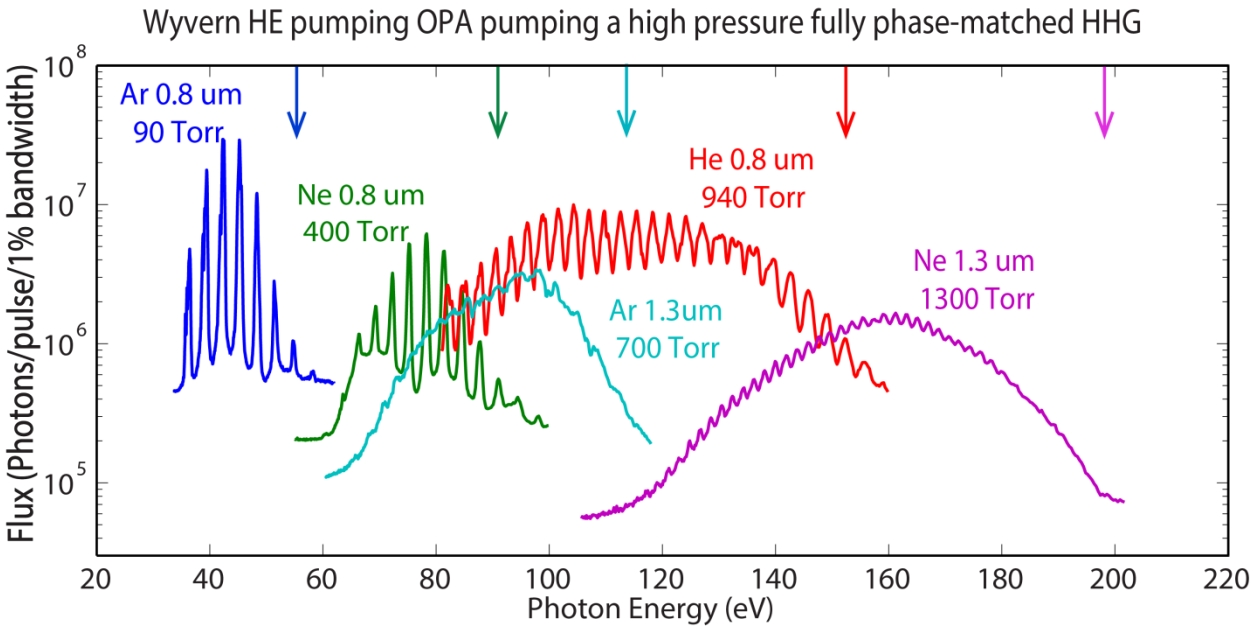

Figure 4.14 Flux comparison of the optimized fully phase matched HHG emission from a 1 cm long, 150 µm diameter, waveguide driven by 1.3 µm and 0.8 µm light in various noble gases (Ar, Ne, and He). The vertical arrows indicate the maximum predicted phase matched HHG energy cutoff for each gas and laser wavelength as predicted in Fig.4.8. The HHG flux obtained using a 1.3 µm driving laser is comparable to that achieved using 0.8 µm.

4.5 Summary and the future investigation

In this chapter, we introduced the HHG history first. Then, to answer the question how to generate the high flux high energy harmonics, we started from the theoretical models for single atom response of HHG in both classical and quantum pictures. Although they both agree that HHG photon energy cutoff could be increased by increasing the wavelength and the intensity of the driving pulse, the low single atom response hits the HHG from long driving wavelength would have low flux. This problem is overcome by the phase matching HHG in hollow waveguide. The decrease of the absorption cross-section at higher photon-energy, associated with the increase of the pressure length product required by the phase matching condition, might balance the low single atom yield in a fully phase matching hollow waveguide HHG. Promoted by this idea, we have achieved a photon flux of more than 10^9 photons/s/1% bandwidth up to 200 eV at kHz repetition rates by using the high quality 1.3 um driving light from a high efficiency OPA. The flux is 1000 times higher than past work. The stability and brightness of this tabletop soft X-ray source indicate great potential for future time resolved molecular and material dynamics studies.

Future investigations:

Preliminary studies from our research have shown that, by tapering the entrance of the hollow waveguide (Fig. 4.15), the HHG flux from Ne with 1.3 um driving light can be increased by 3 times. The taped entrance doesn't help to increase to the coupling efficiency but increases the phase matching pressure. This suggests that the increase of the HHG flux comes from the higher phase matching pressure which is associated with more emitters inside the waveguide. From the phase matching theory, the increase of the phase matching pressure also means the change of the modes inside the waveguide as well. A new field

distribution (mode matching) with high phase matching pressure (phase matching) may help the HHG flux, which is to be studied.

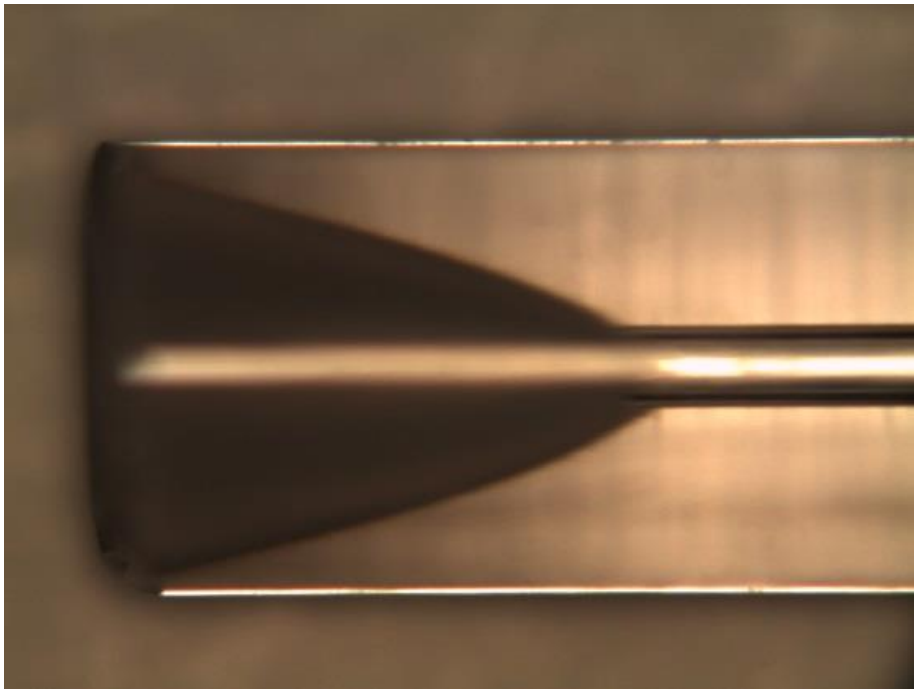

Figure 4.15 The photo of the taper-end hollow waveguide. The taper is 1.5 mm deep, and the outer diameter of hollow waveguide is 1.2 mm, so the angle is 43 deg.

Second, a more interesting experiment is to use the PCF to generate the HHG. PCF typically has very tiny core < 50 um, which would bring up the coupled intensity orders of magnitude higher if the input pulse energy keeps the same. Therefore, this is the way to obtain high rep rate high order harmonic which is the ideal tool to applications, including lithography, imaging and spectroscopy. More details can be seen in Chapter 3.

Chapter 5

NEXAFS from Soft X-Ray HHG and Xe photo-ionization transient absorption spectroscopy

5.1 Introduction

X-ray absorption spectroscopy measures the absorption of X-rays as a function of the incident X-ray photon energy. The general features are (see Fig. 5.1(b)): 1. With the increase of the photon energy, the overall absorption decreases. 2. A few saw-tooth-like features with a sharp rise at discrete energies, called absorption edges, are present in the overall decrease of the X-ray absorption. These absorption edges are corresponding to the photon-electron transition originated from the innermost electron orbitals to the free continuum (ionization of core orbitals) or to unoccupied bound levels just below the ionization limit, for example, originated from $n = 1$ electron orbital is called K-edge, from $n = 2$ electron orbital called L-edge (L_I refers to 2s, L_{II} to $2p_{1/2}$, and L_{III} to $2p_{3/2}$ orbitals), and M, N, etc refers to the corresponding higher lying bound core shells. 3. Fine structures (Fig. 5.1 (c)) are shown around the absorption edges, which could be divided into the X-ray absorption near edge structure (XANES) and the extended X-ray absorption fine structure (EXAFS). Different references name these fine structures differently, so from now on, the X-ray absorption near edge structure (XANES) is called the near edge X-ray absorption fine

structure (NEXAFS) in this thesis, which is more consistent with EXAFS and is used in the book [33]. Simply speaking, the general feature 1 tells us the overall absorption behavior of all elements, which could be derived from quantum mechanics. And, it also explains the possibility and one of the motivations of the long wavelength driving HHG (chapter 4). The general feature 2 provides us the information of the energies of the core energy levels, which is useful but relatively old. And the general feature 3 contains much more information we are interested in, such as the molecular structures, therefore, we are focused in this region. If it is combined with pump-probe technique, a movie of a specific molecular or material dynamics could be recorded by observing the fine structures change.

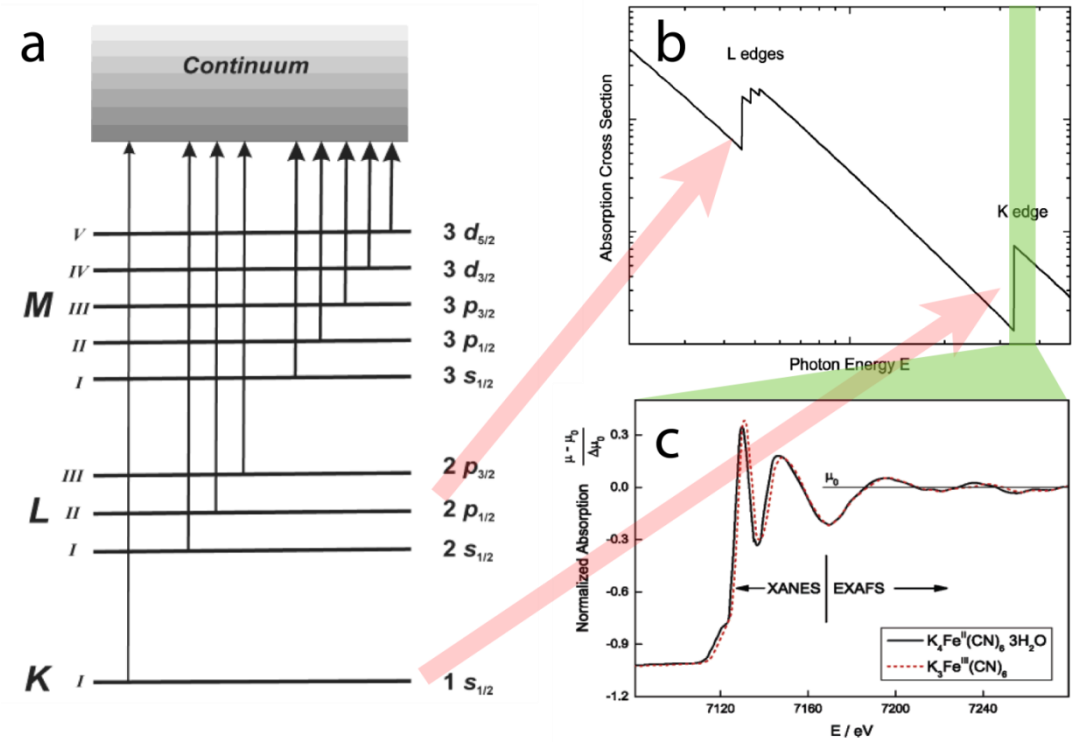

Figure 5.1 (a) Transitions resulting from the absorption of X-rays. (b) Variation of the linear X-ray absorption coefficient of an atom as a function of the photon energy. (c) Example for

the X-ray absorption near edge structure (XANES) and extended X-ray absorption fine structure (EXAFS) from K edge X-ray absorption spectra of iron in $K_4Fe^{II}(CN)_6$ and $K_3Fe^{III}(CN)_6$ bulk samples. Figures are captured from Ref. [114].

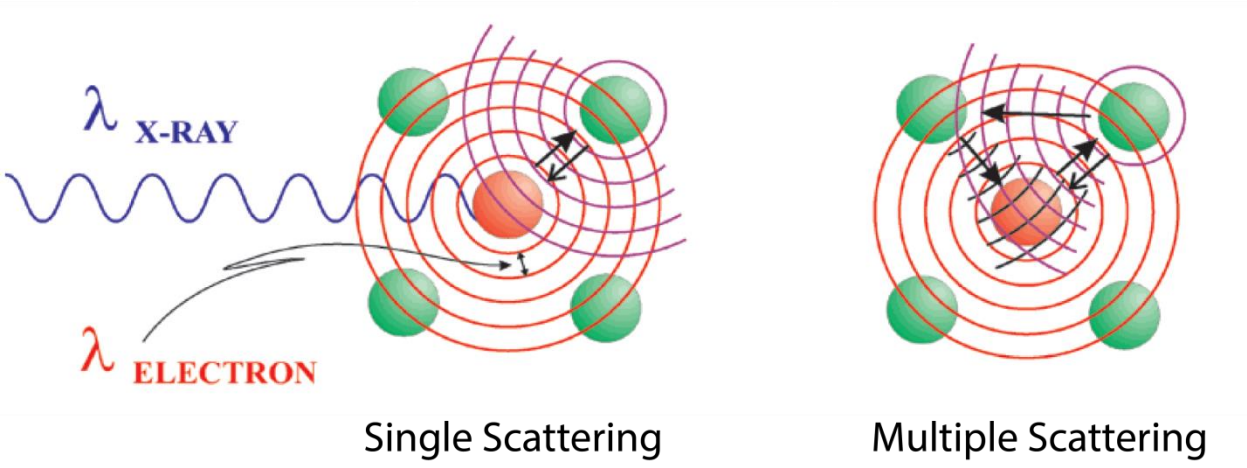

Figure 5.2 Physics picture for X-ray absorption near edge structure (XANES) and extended X-ray absorption fine structure (EXAFS), which are originated from multiple scattering and single scattering, respectively, of the out-going photon-electron excited by the X-ray. Figure is captured from Ref. [114].

Specifically, the EXAFS region covers the high-energy continuum above the ionization threshold, whose energy region is from about 50 eV to even keV above the absorption edge. In this regime, the scattering of outgoing electrons is such that the only significant contributions to the final state wave function in the vicinity of the absorbing atom comes from paths in which the electron is scattered only once (see Fig. 5.2) [115]. An oscillatory structure in the spectrum (Fig. 5.1 (c)) is then present due to the single

scattering. In the energy domain, the oscillatory structure can be obtained directly from the absorption spectrum as,

$$\chi(E) = \frac{\mu(E)-\mu_0(E)}{\Delta\mu_0(E)} \tag{5.1}$$

where, $\mu(E)$ oscillatory absorption coefficient from the spectrum, $\mu_0(E)$ is the smoothly varying atomic-like background absorption, and $\Delta\mu_0(E)$ is the normalization factor. From the relationship between energy and momentum of a free particle,

$$k = \frac{2\pi}{h}\sqrt{2m(h\nu - E_B)} \tag{5.2}$$

where $h\nu$ is the X-ray photon energy, E_B is the binding energy. The oscillatory absorption can be expressed as a function of the wave-vector. Then, by the standard EXAFS formula:

$$\chi(k) = \sum_j S_0^2 N_j \frac{|f_j(k)|}{kR_j^2}\sin(2kR_j + 2\delta_e + \Phi)\exp(-2R_j/\lambda(k))\exp(-2\sigma_j^2 k^2) \tag{5.3}$$

where R_j is the interatomic distances, N_j is the number of the equivalent scatters (the subscript j refers to the group of N_j atoms with identical properties, e.g., bond distance and chemical species), σ_j is the temperature-dependent root mean square fluctuation in bond length, $f_j(k) = |f_j(k)|\exp(i\Phi(k))$ is the backscattering amplitude, δ_e is the central-atom partial-wave phase shift of the final state, $\lambda(k)$ is the energy dependent photon-electron mean free path, and S_0^2 is the overall amplitude reduction factor, the structure information such as the bond length R_j could be obtained from EXAFS.

NEXAFS covers an energy range from slightly below the absorption edge to about 50 eV above the edge. The region that lies below the ionization threshold is dominated by excitations such as transitions to bound valence states or quasi-bound states (so-called shape resonances in molecules), core excitons in ionic crystals, unoccupied local electronic states in metals and insulators, etc. Therefore, structures in this region differ by different classes of materials. The region above ionization threshold comes from the multiple

scattering of the outgoing electrons by neighboring atoms (Fig 5.2). As a result, NEXAFS contains information of both the electronic and the molecular structure, different from EXAFS which mainly contains the structure information. Much valuable electronic and structural information can be unraveled by a careful analysis of the NEXAFS regions. Furthermore, the signal strength of the NEXAFS is about one order of magnitude higher than that of EXAFS, since it is either from the multiple scattering or the transitions to bound states other than the single scattering. So, in synchrotron, measuring EXAFS is considered as a tool to demonstrate to feasibility and stability of the X-ray fine structure measurement since its signal is weaker than NEXAFS (If EXAFS could be obtained, NEXAFS should be easily obtained as well). The disadvantage of the NEXAFS is its information is not as clean as EXAFS, which could be directly used by the simple standard formula (5.3). Complimentary knowledge might be required to analyze the NEXAFS data.

In this thesis, we are focusing on using the soft X-ray to measure the NEXAFS from both solid sample and gas sample, which means the soft X-ray from HHG is the probe light other than the pump light as in most other HHG experiment before [116]. The pioneer work of using HHG source as the probe light in the transient absorption spectroscopy is Leone's group [117-121]. However, they are limited by the 800 nm HHG source, therefore the photon-energy range of the probe light is limited below 100 eV.

Finally, we end up the introduction with definition of the absorbance $A(E)$, which is frequently being used in the later sections:

$$A(E) = -\log_{10} I(E)/I_0(E) \tag{5.4}$$

where $I(E)$ is the X-ray intensity after the sample, and $I_0(E)$ is the intensity before or without the sample.

5.2 EUV- Soft X-ray (transient) absorption spectroscopy scheme

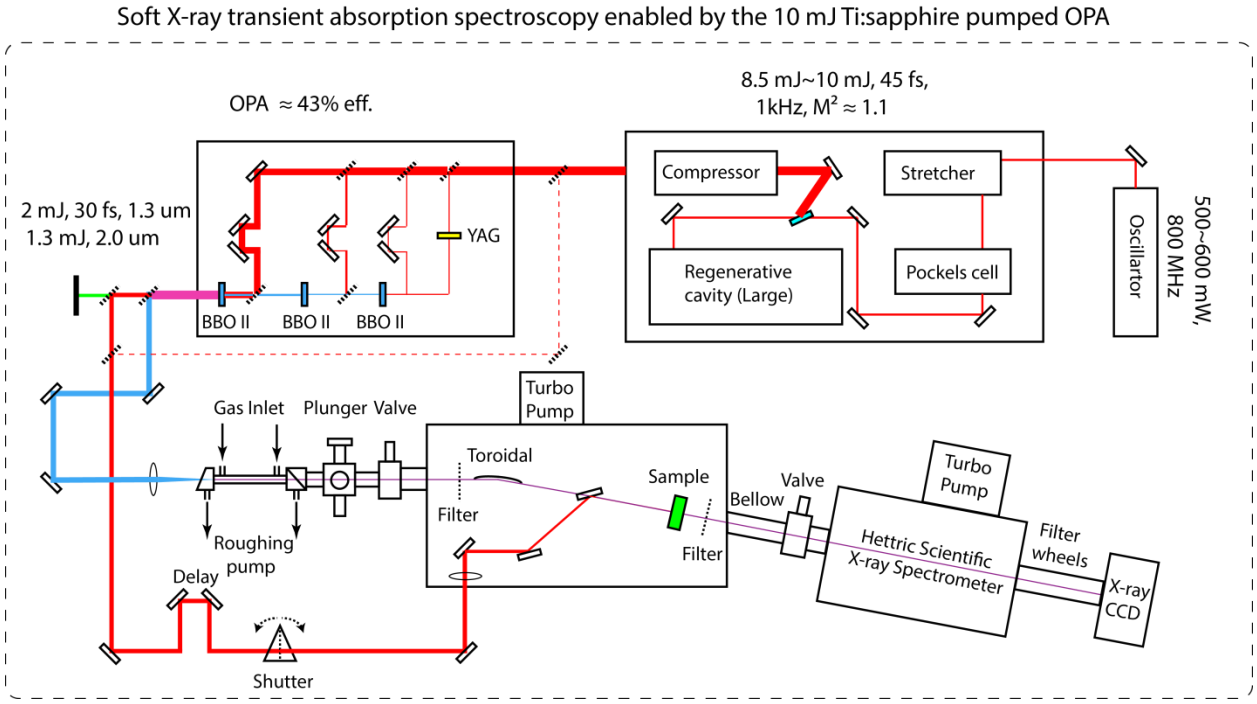

Figure 5.3 The whole soft X-ray transient absorption spectroscopy scheme enabled by the 10 mJ Ti:saphhire pumped OPA.

The whole EUV-soft X-ray transient absorption spectroscopy scheme is shown in Figure 5.3. It starts from the 10 mJ, 45 fs, 1 kHz, Ti:saphhire amplifier, which typically runs around 8.8 mJ for experiments, by reducing the pump power to 42 W and adding one more round trip to the amplification of the seed in the regenerative cavity to reach the gain saturation. The main reason of not running at full power is the pump laser mode (532 nm) becomes better when the pump power is lower, so the amplified cavity mode is better. Although the mode matching between the pump mode, seed mode and cavity mode would help the amplified mode quality compared to that of the multipass amplifier, a bad pump mode would still affect the output mode quality. Some oxygen is filled into the cryogenic cell

to help to reduce the asymmetry of the amplified mode. An elliptical pump (800 nm) mode will not affect the performance (efficiency and pulse duration) of the OPA, but will reduce the coupling efficiency of 1.3 um light into hollow waveguide, since the mode of 1.3 um light from the OPA has very similar shape to the pump mode and the hollow waveguide has cylindrical symmetry. The asymmetry in the pump mode would also affect the overlap between the pump and the probe in the dynamics experiment. (It's important to note that the asymmetry does not have to be shown as a bad M^2 number as mode is still clean.)

The high pulse energy 800 nm light then pumps the efficient three stages OPA (see Chapter 4). The output pulse energy of 1.3 um is around 2 mJ with the pulse duration of 30 fs. The spatial and temporal qualities of the 1.3 um are typically checked by a tight focusing lens. Round, bright, symmetric plasma should be obtained at the exit of the OPA with the lens. The high quality 1.3 um light is then coupled into a 5 mm-1 cm long hollow waveguide by a lens of 25 cm focal length. The gas is supplied through two side holes in the hollow waveguide and pumped efficiently from the entrance and exit of the waveguide by two roughing pumps. Without gas supplied in, the front and back end of the waveguide should be pumped below 100 mTorr, ideally 30 mTorr with the roughing pump we have, to demonstrate no leak. The pumping capacity, especially at the front entrance, is of particular importance, since any residual gas before the waveguide would reduce the coupling efficiency and violate the coupled mode and the residue gas after the waveguide will reabsorb the high harmonic. After the waveguide a differential pumping block is used to keep the vacuum at the experimental side not affected by the gas inside the waveguide, as high phase matching pressure is required for long driving wavelength HHG; the pressure after the different pumping block is typically below 10^{-4} Torr. A plunger is placed after the differential pumping block for checking the coupled mode quality and measuring the coupled 1.3 um pulse energy. Even with high gas pressure supplied into the waveguide,

the coupling efficiency should be 50 % or more for the 1.3 um light, which indicates the good spatial quality of 1.3 um, proper mode coupling (chapter 3) and no leak.

A high vacuum valve is used after the plunger to separate the soft X-ray generation setup from the sample chamber, and one more high vacuum valve is used between the sample chamber and the soft X-ray characterization system, which includes the Hettrick X-ray spectrometer, metal filters and the EUV-X-ray camera. Therefore, the soft X-ray generation setup, the sample chamber and the detection system are well separated, and we can work on each specific part of the whole X-ray beamline without venting the whole system.

In the sample chamber, a 0.2 um thick silver (Ag) filter is placed right after the entrance to block the residue 1.3 um light. Then, a nickel coated toroidal mirror is aligned at a 4 degree grazing angle with respect to the X-ray beam to focus the X-ray down to 100 um diameter at the focus. This incidence angle is critical since it not only affects the focal size but also the focal shape of the X-ray beam (the probe), which determines the overlap between the pump and probe light. The flatness of the Ni coating is critical as well, since the X-ray optics requires a finer surface than the EUV optics due to the wavelength of the X-ray is shorter. The reflectivity of a layer of Ni at grazing angle of 4 degree should be around 60 %, but the “coarse” surface may easily reduce it to 30 %. After the toroidal mirror, the X-ray passes through a mirror with a hole at the center. The “with hole mirror” is used to combine the pump and probe beam before the sample, where the probe beam transmits through the hole and the pump beam is reflected on the surface, so the pump and the probe beams are nearly parallel after the mirror into the sample. The sample is set at the focus of the X-ray on a 3 dimensional controlled translational stage to optimize the transmission of the X-ray through the sample. The sample holder is also mounted on a rotational stage with the rotation axis perpendicular to the X-ray beam, so that the sample surface (in the case of

the solid sample) could be set perpendicular to the X-ray precisely. The detailed designs for the gas sample and the solid sample are shown in Fig. 5. 4.

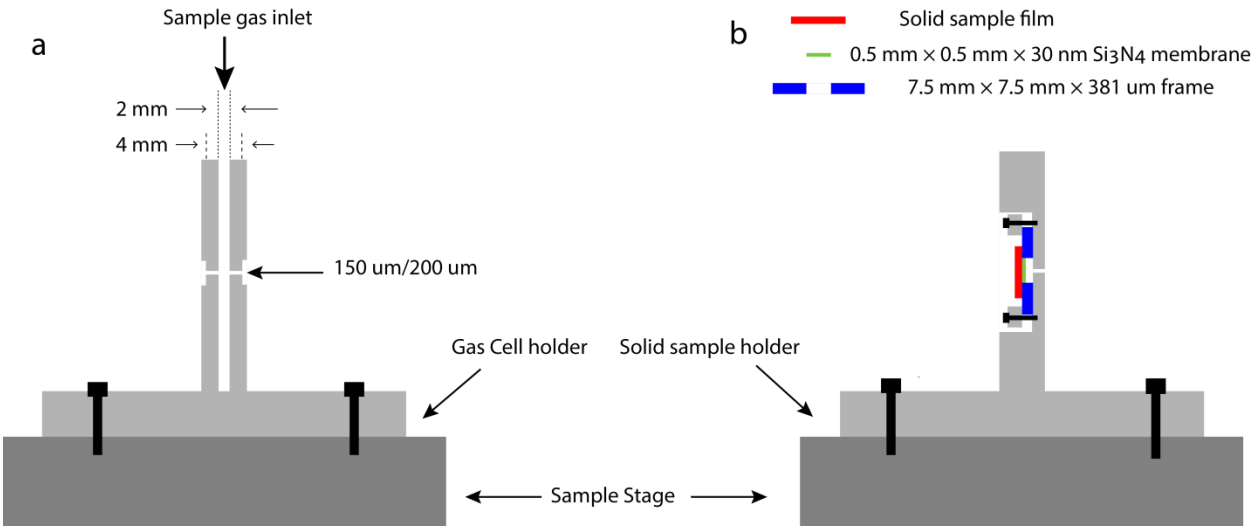

Figure 5.4 The sample holder designs. (a) The gas cell design. (b) The solid sample holder design.

A 2 mm thick gas cell is used for the gas phase experiment. The gas is supplied from a side hole by a 1/8 inch diameter hose. The entrance and exit for the X-ray beam on the gas cell are 150 um or 200 um diameter holes at the center of the cell. The gas density inside the cell is controlled by the supplied gas pressure. Typically, the pressure inside the gas cell is from 20 Torr to 50 Torr to introduce enough absorption depth (Fig 5.5). The sample chamber is pumped by a 300 liters/s turbo pump, therefore, although the sample gas is leaking from the gas cell through the entrance and exit holes for the X-ray beam, the background gas pressure inside the sample chamber is being kept around 10 mTorr. Considering the sample chamber length is 40 cm, the absorption from the gas density

outside the gas cell to the total absorption signal is less than 10 % inside the sample chamber.

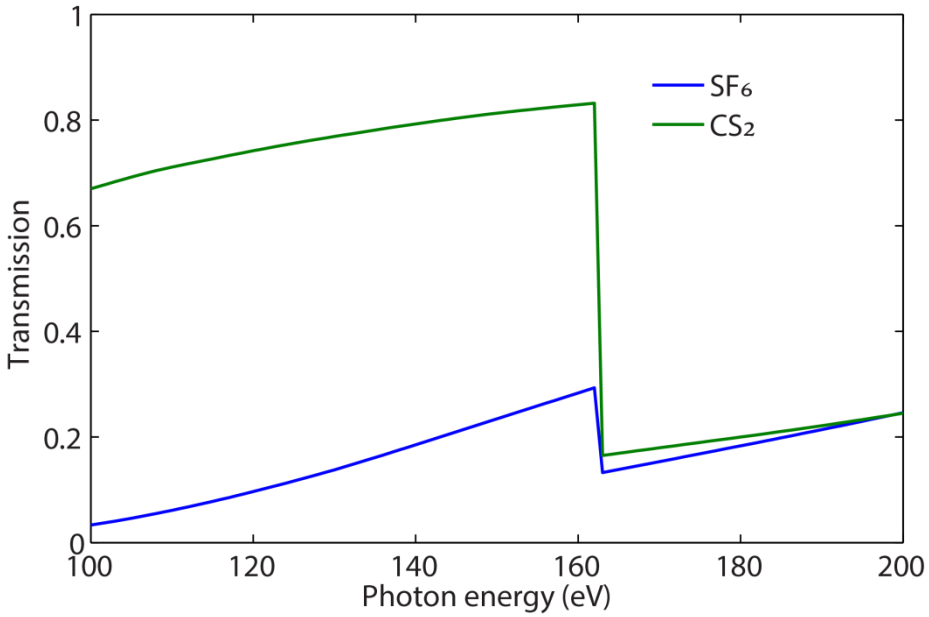

Figure 5.5 The soft X-ray transmission from gas SF_6 and CS_2 through the 2 mm thick gas cell with gas pressure at 30 Torr. Data obtained from www.CXRO.com.

So far, this number is limited by the relatively small hole on the chamber wall connecting the turbo pump, which reduces the pumping capacity. If we can increase the size of the hole to the required dimension, then the background pressure should be able to reduce to less than 1 mTorr, and the absorption from the gas density outside the gas cell to the total absorption signal will be reduced to less than 1%, which could be neglected. For the static absorption experiment, the absorption of the gas outside the gas cell is not a problem, but for the dynamics experiment, it will affect the signal to noise (s/n) ratio.

The solid sample film is coated on a thin (30 nm) Silicon Nitride membrane window from solution either by the spin coating method or the simple drip and evaporation method. The 30 nm thick Silicon Nitride window will absorb the soft X-ray beam by 35 %-50 % at photon energy range from 100 eV to 200 eV. And the thickness of the sample is typically around tens to hundreds of nanometer depending on the solution density. The Silicon Nitride window is 500 um by 500 um big, which is sitting at the center of a 7.5 mm by 7.5 mm big frame. Since the focus of the X-ray is around 100 um diameter, the X-ray beam can through the solid sample and window without any clipping.

The last element in the sample chamber is another metallic filter, which is used to block the residue pump light after the sample. After the sample chamber is the EUV-X-ray spectrometer (Hettrick scientific). It is consisted of a pair of Kirkpatrick-Baez (KB) mirrors and a set of EUV-X-ray gratings. The X-ray beam is focused and spectrally dispersed by them. Then after another two or three filters, which thoroughly block any residue pump or stray light, the spectrum is recorded on the EUV-X-ray CCD camera at the imaging point.

Finally, plenty of choices of the pump wavelength and sufficient pump power are available for the dynamics experiment due our high energy amplifier and the light conversion OPA. For example, the residue 800 nm light (3 mJ to 4 mJ) after the OPA could be used for the strong field ionization and dissociation experiment; small amount of 800 nm light could be split before the OPA (dash line in Fig 5.3) when the pump of high mode quality is needed; and with the nonlinear crystal or crystal combinations, wavelengths of 200 nm, 267 nm, 400 nm, 500 nm, 1 um, and 2 um have all been achieved for the pump light already. At the meantime, a shutter is placed in the pump beam line, which is synchronized with the CCD camera. 0.1 second exposure time of the camera (5 Hz shutter speed) is chosen to real-time subtract pump on and pump off signals in order to reduce the effect from HHG fluctuation.

5.3 Soft X-ray NEXAFS from gas phase and solid phase samples

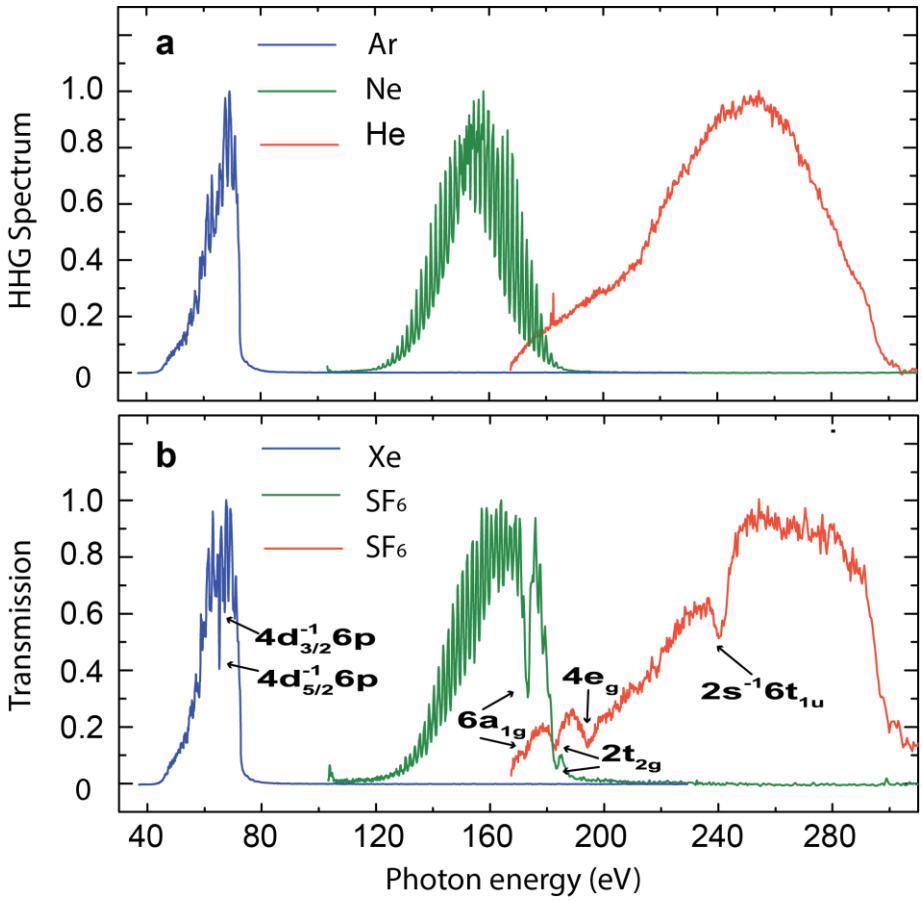

Figure 5.6 (a) Normalized High-order harmonics spectrum generated from Ar, Ne and He gases with driving laser wavelength at 1.3 μm. (b) Normalized Xe transmission spectrum observed using harmonics from Ar, and SF_6 transmission observed using harmonics from Ne and He.

By passing the high harmonics through a 2 mm long, 200 μm diameter gas cell, the absorption signal from the sample can be directly observed from the transmitted HHG spectrum (Fig 5.6). For example, for SF_6 gas, using harmonics generated from Ne, we simultaneously observe three Sulfur 2p inner well resonance absorption peaks [122] $6a_{1g}$,

$2t_{2g}$, $4e_g$, as well as $2t_{2g}$ and $4e_g$ shape resonances. When the SF6 gas transimssion is measured using He HHG, one additional Sulfur 2s Fano-type resonance absorption peak [123] $2s^{-1}$ $6t_{1u}$ appears in the spectrum. The absorption peak $6a_{1g}$, which is not obvious in the spectrum of the harmonics from He, is much sharper in the Ne HHG spectrum. Note that in the He data, an absorption at a photon energy of 285eV originates from the carbon (C) K-edge, due to C contamination on the spectrometer optics. Thus, we can measure the absorption spectrum of multiple elements simultaneously. Figure 5.6 (b) also shows the 4d giant resonance absorption in Xe [124] at high spectral resolution using harmonics from Ar gas, which clearly resolves absorption from different spin states. (We are going to discuss the Xe absorption in details in the photon-ionization transient absorption experiment.) This demonstrates element specificity and sensitivity to electronic structure over a very broad ~250 eV spectral range in a tabletop setup.

High quality absorption spectra can be obtained by taking the logarithm of the ratio between the transmitted harmonic spectrum without (Figure 5.6 (a)) and with the sample gas (Figure 5.6 (b)), for the same exposure time, as the definition from absorbance as mentioned in the introduction. Figure 5.7 (b) shows the SF6 Sulfur L-edge 2p orbital NEXAFS structure. Different transitions and spin states are clearly resolved and assigned using synchrotron data [122], and the 1.2 eV energy splitting due to the Sulfur 2p orbital spin states splitting in the absorption peaks $6a_{1g}$ and $2t_{2g}$ agrees well with synchrotron data. Although the energy resolution is currently 0.25 eV, limited by 160 g/mm groove density of the grating used in our setup, further increases in spectral resolution will be possible using a higher groove-density grating.

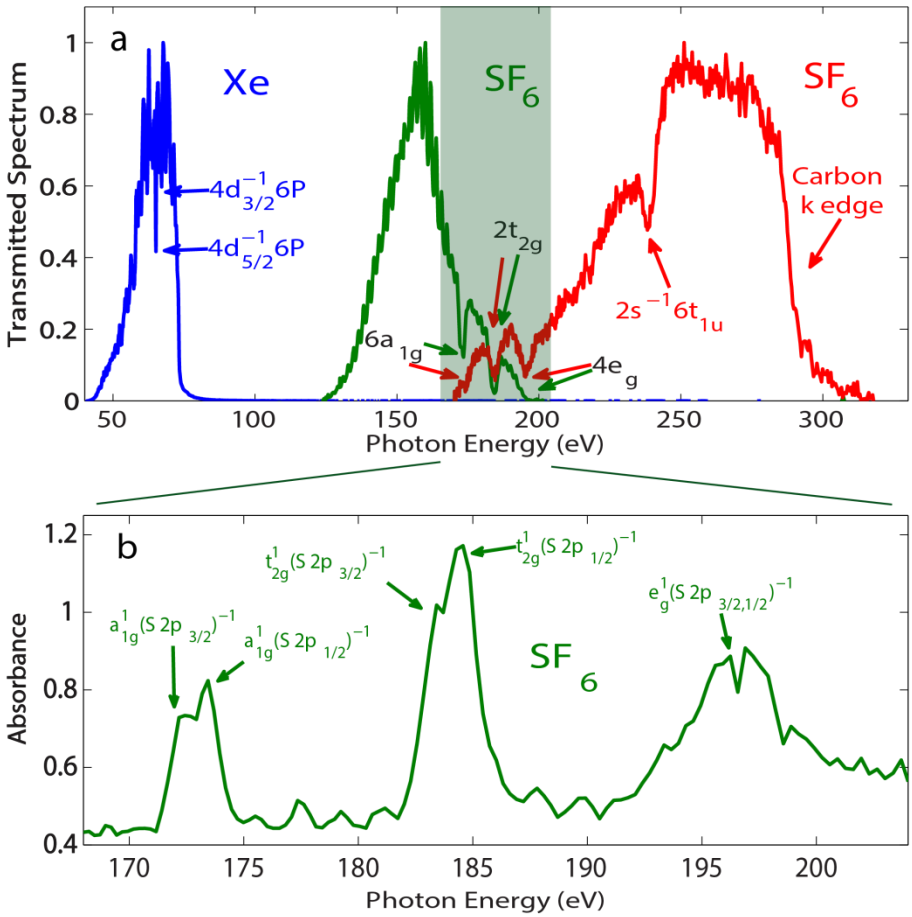

Figure 5.7 (a) Normalized raw data for 1.3 μm-driven HHG from Ar (blue), Ne (green), and He (red) after transmission through a 2 mm long sample cell of Xe (HHG from Ar), and SF_6 (HHG from Ne and He). Note that the apparent gap between 70 eV and 100 eV is because of Al filters used to block the fundamental light—full tuning across this range can be achieved by switching to other filters as shown in Fig. 2. (b) NEXAFS spectrum of SF_6 Sulfur L-edge 2p orbital. The high quality NEXAFS spectra were obtained in a 300 s exposure time. However, changes in the absorption signal can be monitored in real time, with exposures as short as 0.1 s. The modulations between the resonance absorption peaks $6a_{1g}$, $2t_{2g}$, and $4e_g$ arise from individual harmonic peaks that are separated by 1.9 eV. These modulations can be reduced by increasing the driving pulse energy into the hollow waveguide, implementing beam pointing stabilization, and reducing the integration time. Figures are captured from Ref. [125].

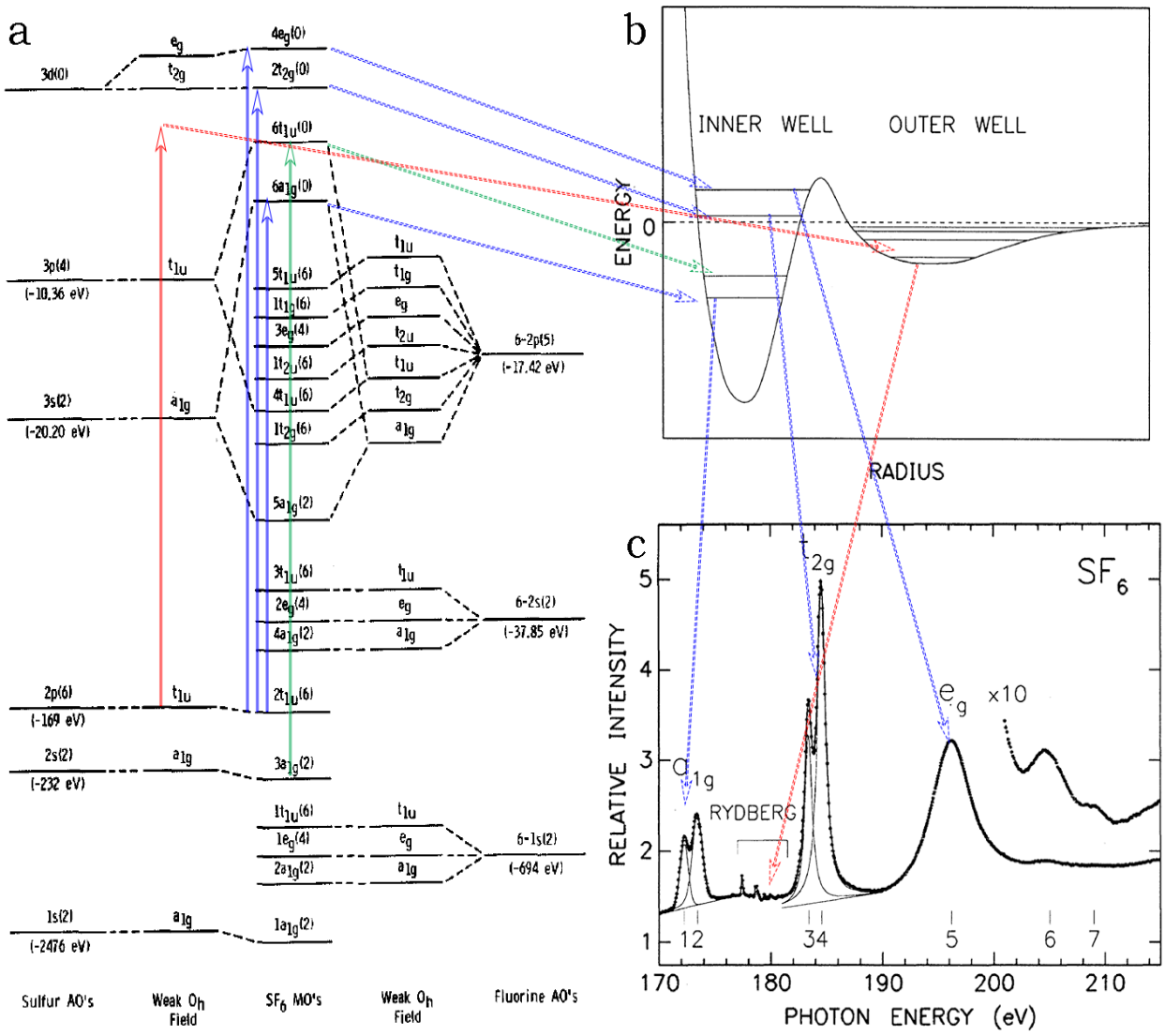

Figure 5.8 (a) Schematic MO diagram for SF_6. Figure is captured from [126]. (b) Schematic representation of the double-well potential (not to scale) for SF_6. The barrier divides the potential curve into two regions, the inner well and the outer well. Valence orbitals are located mainly in the inner well. Rydberg orbitals are located mainly in the outer well. (c) Synchrotron data for SF_6 NEXAFS. Figures (b) and (c) are captured from [122].

The observed SF_6 NEXAFS could be explained by the molecular orbital (MO) theory. Generally, the resonances in NEXAFS spectra here arise from the excitation of a core electron into a virtual orbital. The final state of the system is commonly described by referring to the character of the newly occupied orbital. In particular, the transition may be

to an inner-well or outer-well state, which is similar to the atomic partial-wave potential energy diagram for an electron of angular momentum $l > 1$, where centrifugal contribution to the potential energy may combine with the electrostatic contributions to produce a potential barrier as shown in Fig 5.8 (b). In molecules the electrons around the outer atoms produce a similar barrier along the bond directions. Virtual orbitals with a spatial distribution primarily inside the potential barrier are known as inner-well orbitals. If an electron is promoted into such a valence orbital, the system is said to be in an inner-well state. Allowed transitions to these states are normally quite intense in NEXAFS spectra. If the virtual orbital is located mainly in the outer well, the transition is to a Rydberg state. These transitions are normally weak in NEXAFS spectra as a result of poor spatial overlap between the initial-state and final-state orbitals. Transitions to bound inner-well states lie at energies below transitions to Rydberg states. The Rydberg resonances have a series of energies which converge on the absorption edge from below. Transitions to quasibound inner-well states are referred to as shape resonances and occur at energies above the absorption edge. Specifically, the $6a_{1g}$ resonance (blue line in Fig. 5.8 (a)) is corresponding to the excitation from $2t_{1u}$ orbital, originated from Sulfur 2p orbital (L_{II}, L_{III} edge depending on the angular momentum), to the $6a_{1g}$ bound inner-well state; $2t_{2g}$, $4e_g$ resonance (blue line in Fig. 5.8 (a)) are excitation from $2t_{1u}$ orbital to $2t_{2g}$, $4e_g$ quasibound inner-well states, shape resonances; and the $6t_{1u}$ resonance (green line in Fig. 5.8 (a)) is excitation from $3a_{1g}$ orbital, originated from Sulfur 2s orbital (L_I edge), to $6t_{1u}$ inner-well state, referred as Fano-type resonance. In the synchrotron data (Fig 5.8 (c)), the Rydberg resonances (red line in Fig. 5.8 (a)) were also observed. In high harmonic spectra, the harmonic peak fluctuation is much larger than the fluctuation of the overall counts; therefore, the Rydberg resonances haven't been captured by our HHG soft X-ray source so far. However, comparing our data with the synchrotron data, the inner-well resonances including the spin information are all captured.

Another sample gas CS_2 is also measured by our soft X-ray source, and the NEXAFS is shown in Fig 5.9 (a). Comparing with the synchrotron data (Fig 5.9 (b)), the absorption fine structure above 166 eV is resolved. However, the fine structure below the 166 eV (the red shadow in Fig 5.9 (a)) is overwhelmed by the harmonic peak fluctuation. Therefore, the peak fluctuation is the main limitation in our absorption measurement. Since the harmonic peak is an indication of the pulse train of the generated high harmonic, and the longer driving pulse, such as the 2 um wavelength, would generate single atto-burst under the phase matching condition [113], the better absorption data would be obtained by using longer driving pulse HHG. For the soft X-ray source from 1.3 um, over-ionize the noble gas for HHG is a way to reduce the harmonic peak fluctuation.

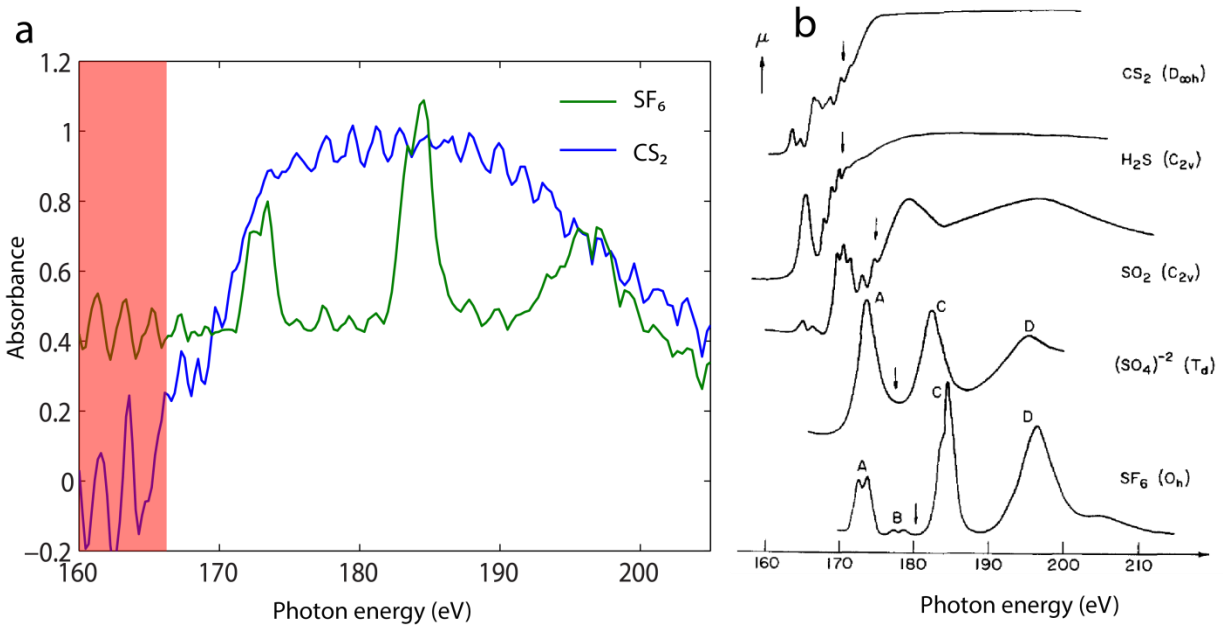

Figure 5.9 (a) NEXAFS of CS_2 and SF_6 obtained from our HHG Soft X-ray. (b) Synchrotron data for CS_2, H_2S, SO_2, $(SO_4)^{-2}$, and SF_6 NEXAFS, adapted from [126].

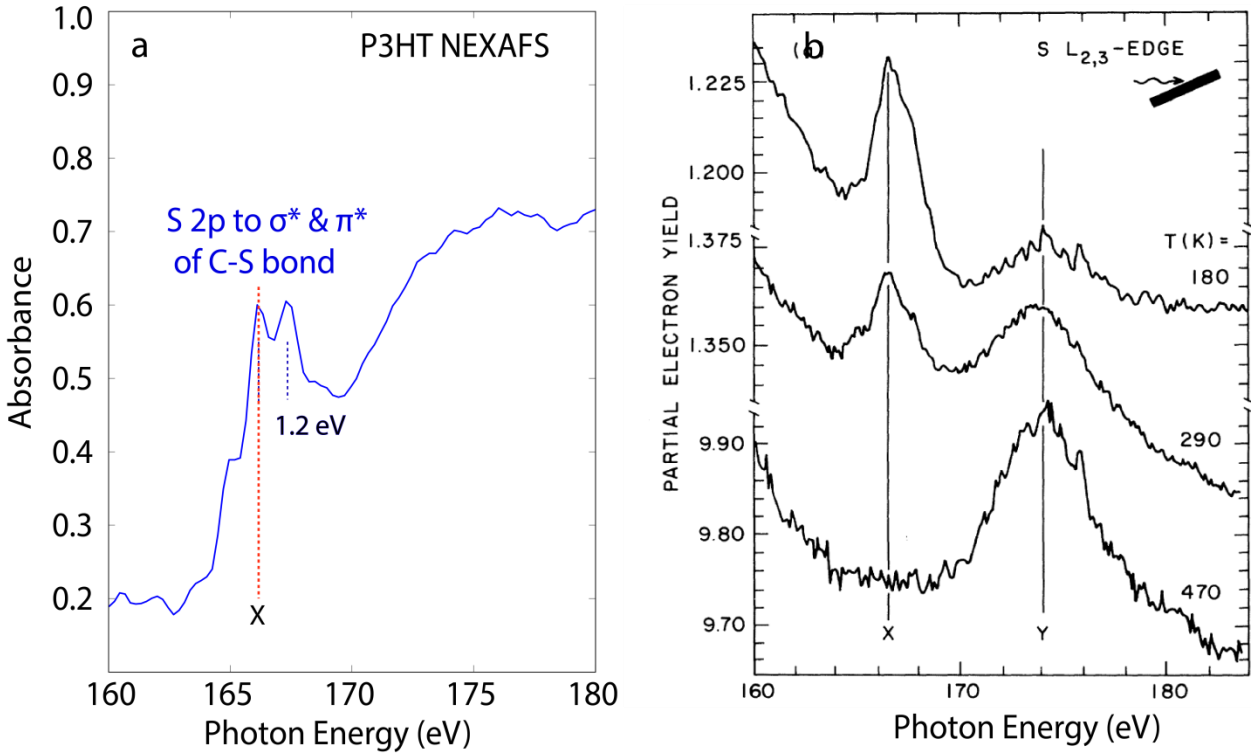

Figure 5.10 (a) NEXAS from P3HT. The red vertical line indicates where the peak X is in (b). (b) NEXAS from thiophene (C_4H_4S) on Pt (111), adapted from [127].

After investigating the gas sample, the solid sample P3HT, Poly (3-hexylthiophene-2, 5-diyl), is measured because of its popularity in the solar cell material research. An absorption peak splitting around 166 eV is shown in the NEXAFS (see Fig. 5.10 (a)). Since the peak is spitted by 1.2 eV, they cannot be both from the harmonic fluctuation. In order to understand the origin of the absorption, we searched in the synchrotron data, and only the data of thiophene (C_4H_4S) is found. (P3HT could be considered as the polymer of thiophene) [127]. In the thiophene NEXAFS, two absorption peaks X and Y are shown in the photon energy range we are discussing now. Peak X corresponds to transitions of S 2p electrons to closely spaced unfilled σ^* and π^* molecular orbitals associated with the S-C bond in thiophene. And Peak Y is a substrate-enhanced atomic resonance in the continuum due to

excitations to d-like final states, because the thiophene is on the Pt (111) substrate in that experiment. Therefore, the absorption peak shown in Fig. 5.10 (a) is probably the transitions of S 2p electrons to unfilled σ^* and π^* molecular orbitals.

5.4 EUV transient absorption spectroscopy: Xe photon-ionization

Besides the static absorption, the high repetition rate enabled high flux broadband high-order harmonics also allows us to follow the dynamics, such as the charge transfer, using femtosecond-resolved transient absorption spectroscopy. To demonstrate this, we studied the ionization process of Xe gas using harmonics from Ar. The residual 800 nm light left after pumping the OPA is focused into the cylindrical gas cell to photon-ionize the Xe gas as the pump beam by a lens of 25 cm focal length. The ionization induces additional absorption peaks in Xe and these peaks can be detected using harmonics from Ar. The Xe gas pressure inside of the gas cell is 30 Torr. The residual pump pulse is blocked by a 0.2 um thick Al filter after the cell.

The neutral Xe 4d absorption peaks (Fig. 5.11 (a)), match the data from synchrotron [124]. When the pump pulse is incident before the probe beam, four introduced absorption peaks appear in the spectrum (Fig. 5.11 (b)). The photon energy corresponding to the four peaks are 55.4 eV, 56.1 eV, 57.1 eV and 57.6 eV. According to previous studies of the Xe ion 4d giant resonance [128], peak 1 and 2 corresponding to the Xe^+ ($4d^{10}5p^5$ $^2P \rightarrow 4d^9 5p^6$ ^2D) resonances, and the transitions are $2P_{3/2} \rightarrow 2D_{5/2}$ and $2P_{1/2} \rightarrow 2D_{3/2}$ respectively. Peak 3 and 4 are corresponding to the Xe^{2+} ($4d^{10}5p^4 \rightarrow 4d^9 5p^5$) resonances, which include four transitions theoretically. Additionally, the intensity ratios between peaks 1 and 2 and peaks 3 and 4 are close to the published oscillator strength ratios. Thus, the ability to resolving a set of

congested absorption peaks demonstrates the fine frequency resolution of transient spectra taken using a HHG soft X-ray source. Furthermore, even without further compression, the high harmonic beam can be used to probe ultrafast dynamics on the order of tens of femtosecond. With a 10 fs step size all four absorption peaks build up within 75 fs after the time zero, as shown in the difference data from the subtraction of the pump on and pump off counts (See Fig. 5.11 (c)).

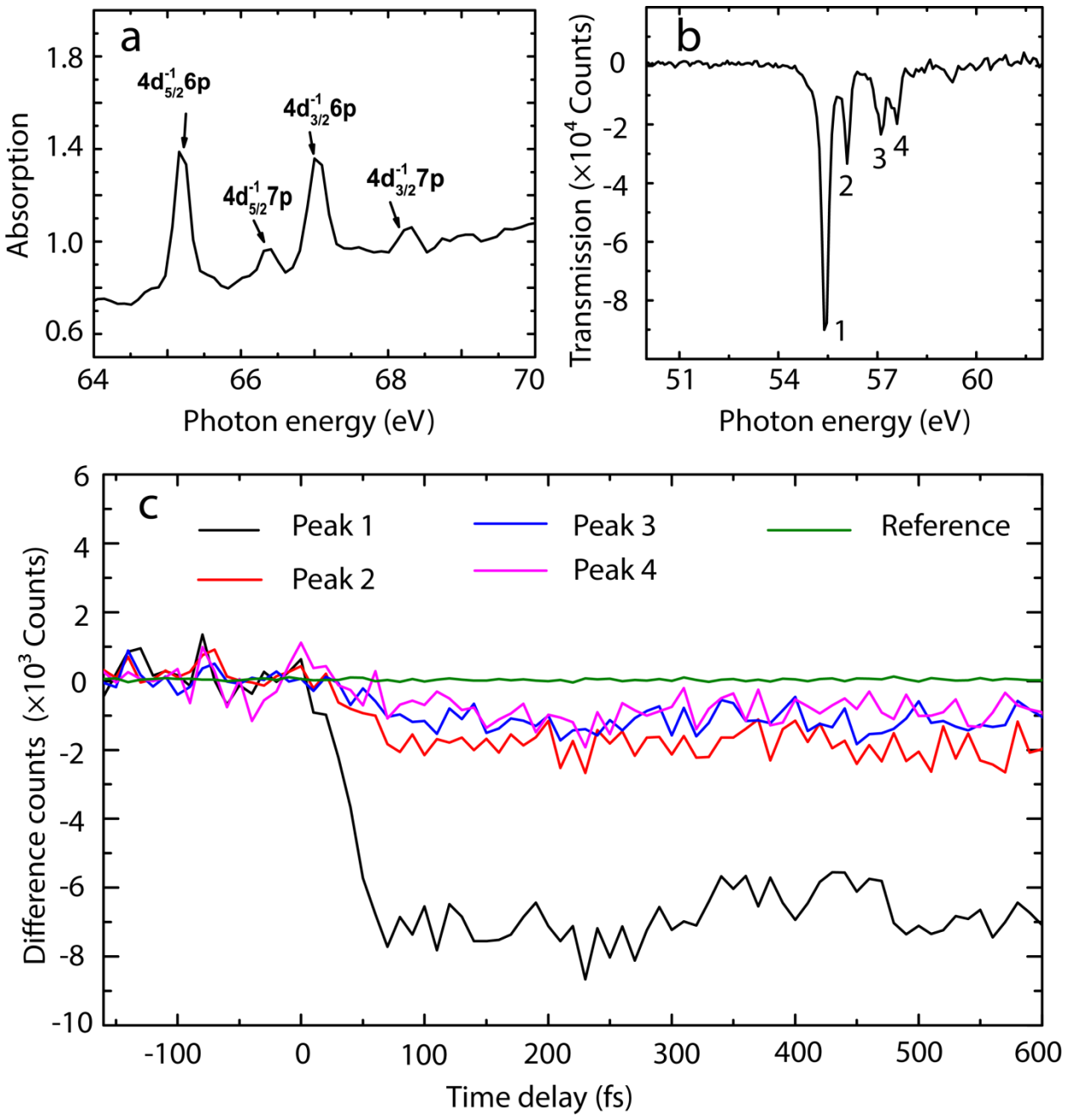

Figure 5.11 (a) Neutral Xe 4d absorption. (b) Xe^{+} and Xe^{2+} 4d absorption. (c) Xe^{+} and Xe^{2+} transient absorption signal.

5.5 Conclusion and ongoing experiment

In this chapter, we first introduced the X-ray absorption features, especially, the fine structures of the absorption edge. Then, we introduced the Soft X-ray transient absorption spectroscopy setup we have implemented. After that, we presented the NEXAFS from the gas sample SF_6 and CS_2, and solid sample P3HT using our soft X-ray source. Finally, we demonstrated the transient absorption spectroscopy by resolving the Xe photon-ionization process in the EUV region.

Ongoing experiment

The samples for static NEXAFS measurements are all the proposed samples for soft X-ray region transient absorption spectroscopy experiments we are doing. For example, SF_6 shape resonance could be used for detecting the vibrational dynamics pumped by impulsive stimulated Raman scattering; P3HT could be used for studying the charge transfer in the solar cell material.

Bibliography

[1] Ferenc Krausz, Misha Ivanov. Attosecond physics. Reviews Of Modern Physics, 81: 172-234, 2009.

[2] A. Rundquist, C. G. Durfee, Z. Chang, C. Herne, S. Backus, M. M. Murnane, and H. C. Kapteyn. Phase-Matched Generation of Coherent Soft X-rays. Science, 280: 1412-1415, 1998.

[3] R. A. Bartels, A. Paul, H. Green, H. C. Kapteyn, M. M. Murnane, S. Backus, I. P. Christov, Y. Liu, D. Attwood, and C. Jacobsen. Generation of Spatially Coherent Light at Extreme Ultraviolet Wavelengths. Science, 297: 376-378, 2002.

[4] T. Popmintchev, M.-C. Chen, D. Popmintchev, P. Arpin, S. Brown, S. Ališauskas, G. Andriukaitis, T. Balčiunas, O. D. Mücke, A. Pugzlys, A. Baltuška, B. Shim, S. E. Schrauth, A. Gaeta, C. Hernández-García, L. Plaja, A. Becker, A. Jaron-Becker, M. M. Murnane, and H. C. Kapteyn. Bright Coherent Ultrahigh Harmonics in the keV X-ray Regime from Mid-Infrared Femtosecond Lasers. Science, 336: 1287-1291, 2012.

[5] C. G. Durfee, A. R. Rundquist, S. Backus, C. Herne, M. M. Murnane, and H. C. Kapteyn. "Phase Matching of High-Order Harmonics in Hollow Waveguides. Physical Review Letters, 83: 2187-2190,1999.

[6] E. Constant, D. Garzella, P. Breger, E. Mével, Ch. Dorrer, C. Le Blanc, F. Salin, and P. Agostini. Optimizing High Harmonic Generation in Absorbing Gases: Model and Experiment. Physical Review Letters, 82: 1668-1671, 1999.

[7] J. M. Glownia, J. Cryan, J. Andreasson, A. Belkacem, N. Berrah, C. I. Blaga, C. Bostedt, J. Bozek, L. F. DiMauro, L. Fang, J. Frisch, O. Gessner, M. Gühr, J. Hajdu, M. P. Hertlein, M. Hoener, G. Huang, O. Kornilov, J. P. Marangos, A. M. March, B. K. McFarland, H. Merdji, V. S. Petrovic, C. Raman, D. Ray, D. A. Reis, M. Trigo, J. L. White, W. White, R. Wilcox, L. Young, R. N. Coffee, and P. H. Bucksbaum. Time-resolved pump-probe experiments at the LCLS. Optics Express, 18: 17620-17630, 2010.

[8] H. T. Lemke, C. Bressler, L. X. Chen, D. M. Fritz, K. J. Gaffney, A. Galler, W. Gawelda, K. Haldrup, R. W. Hartsock, H. Ihee, J. Kim, Kyung Hwan Kim, J. H. Lee, M. M. Nielsen, A. B. Stickrath, W. Zhang, D. Zhu, and M. Cammarata. Femtosecond X-ray Absorption

Spectroscopy at a Hard X-ray Free Electron Laser: Application to Spin Crossover Dynamics. The Journal of Physical Chemistry A, 117: 735-740, 2013.

[9] T. E. Glover, D. M. Fritz, M. Cammarata, T. K. Allison, S. Coh, J. M. Feldkamp, H. Lemke, D. Zhu, Y. Feng, R. N. Coffee, M. Fuchs, S. Ghimire, J. Chen, S. Shwartz, D. A. Reis, S. E. Harris, and J. B. Hastings. X-ray and optical wave mixing. Nature, 488: 603-609, 2012.

[10] I. P. Christov, M. M. Murnane, and H. C. Kapteyn. High-Harmonic Generation of Attosecond Pulses in the "Single-Cycle" Regime. Physical Review Letters, 78: 1251-1254, 1997.

[11] G. Sansone, E. Benedetti, F. Calegari, C. Vozzi, L. Avaldi, R. Flammini, L. Poletto, P. Villoresi, C. Altucci, R. Velotta, S. Stagira, S. De Silvestri, and M. Nisoli. Isolated Single-Cycle Attosecond Pulses. Science. 314: 443-446, 2006.

[12] E. Goulielmakis, M. Schultze, M. Hofstetter, V. S. Yakovlev, J. Gagnon, M. Uiberacker, A. L. Aquila, E. M. Gullikson, D. T. Attwood, R. Kienberger, F. Krausz, and U. Kleineberg. Single-Cycle Nonlinear Optics. Science, 320: 1614-1617, 2008.

[13] R. Velotta, N. Hay, M. B. Mason, M. Castillejo, and J. P. Marangos. High-Order Harmonic Generation in Aligned Molecules. Physical Review Letters, 87: 183901, 2001.

[14] N. L. Wagner, A. Wüest, I. P. Christov, T. Popmintchev, X. Zhou, M. M. Murnane, and H. C. Kapteyn. Monitoring molecular dynamics using coherent electrons from high harmonic generation. Proceedings of the National Academy of Sciences of the United States of America,103: 13279-13285, 2006.

[15] Z. H. Loh, M. Khalil, R. E. Correa, R. Santra, C. Buth, and S. R. Leone. Quantum State-Resolved Probing of Strong-Field-Ionized Xenon Atoms Using Femtosecond High-Order Harmonic Transient Absorption Spectroscopy. Physical Review Letters, 98: 143601, 2007.

[16] W. Li, X. Zhou, R. Lock, S. Patchkovskii, A. Stolow, H. C. Kapteyn, and M. M. Murnane. Time-Resolved Dynamics in N2O4 Probed Using High Harmonic Generation. Science, 322: 1207-1211, 2008.

[17] R. Haight and D. R. Peale. Tunable Photoemission with Harmonics from Subpicosecond Lasers. Review of Scientific Instruments, 65: 1853-1857, 1994.

[18] R. Haight and P. F. Seidler. High Resolution Atomic Core Level Spectroscopy with Laser Harmonics. Applied Physics Letters, 65: 517-519, 1994.

[19] M. Probst and R. Haight. Unoccupied molecular orbital states of tris (8-hydroxy quinoline) aluminum: Observation and dynamics. Applied Physics Letters, 71: 202-204, 1997.

[20] K. Read, H. S. Karlsson, M. M. Murnane, H. C. Kapteyn, and R. Haight. Excitation dynamics of dye doped tris (8-hydroxy quinolone) aluminum films studied using time-resolved photoelectron spectroscopy. Journal of Applied Physics, 90: 294-300, 2001.

[21] M. E. Siemens, Q. Li, R. Yang, K. A. Nelson, E. H. Anderson, M. M. Murnane, and H. C. Kapteyn. Quasi-ballistic thermal transport from nanoscale interfaces observed using ultrafast coherent soft X-ray beams. Nature Materials, 9: 26-30, 2010.

[22] E. Turgut, C. La-o-vorakiat, J. M. Shaw, P. Grychtol, H. T. Nembach, D. Rudolf, R. Adam, M. Aeschlimann, Cl. M. Schneider, T. J. Silva, M. M. Murnane, H. C. Kapteyn, and S. Mathias. Controlling the Competition between Optically Induced Ultrafast Spin-Flip Scattering and Spin Transport in Magnetic Multilayers. Physical Review Letters, 110: 197201, 2013.

[23] S. Hellmann, T. Rohwer, M. Kalläne, K. Hanff, C. Sohrt, A. Stange, A. Carr, M. M. Murnane, H. C. Kapteyn, L. Kipp, M. Bauer, and K. Rossnagel. Time-domain classification of charge-density-wave insulators. Nature Communications, 3: 1069, 2012.

[24] M. D. Seaberg, D. E. Adams, E. L. Townsend, D. A. Raymondson, W. F. Schlotter, Y. Liu, C. S. Menoni, L. Rong, C. C. Chen, J. Miao, H. C. Kapteyn, and M. M. Murnane. Ultrahigh 22 nm resolution coherent diffractive imaging using a desktop 13 nm high harmonic source. Optics Express, 19: 22470-22479, 2011.

[25] M. D. Seaberg, B. Zhang, D. F. Gardner, E. R. Shanblatt, M. M. Murnane, H. C. Kapteyn, and D. E. Adams. Tabletop Nanometer Extreme Ultraviolet Imaging in an Extended Reflection Mode using Coherent Fresnel Ptychography. http://arxiv.org/abs/1312.2049

[26] T. Popmintchev, M.-C. Chen, O. Cohen, M. E. Grisham, J. J. Rocca, M. M. Murnane, and H. C. Kapteyn. Extended phase matching of high harmonics driven by mid-infrared light. Optics Letters, 33: 2128-2130, 2008.

[27] T. Popmintchev, M.-C. Chen, A. Bahabad, M. Gerrity, P. Sidorenko, O. Cohen, I. P. Christov, M. M. Murnane, and H. C. Kapteyn. Phase matching of high harmonic generation in the soft and hard X-ray regions of the spectrum. Proceedings of the National Academy of Sciences of the United States of America,106: 10516-10521, 2009.

[28] M.-C. Chen, P. Arpin, T. Popmintchev, M. Gerrity, B. Zhang, M. Seaberg,D. Popmintchev, M. M. Murnane, and H. C. Kapteyn. Bright, Coherent, Ultrafast Soft X-Ray Harmonics Spanning the Water Window from a Tabletop Light Source. Physical Review Letters, 105: 173901, 2010.

[29] G. Andriukaitis, T. Balčiūnas, S. Ališauskas, A. Pugžlys, A. Baltuška, T. Popmintchev, M.-C. Chen, M. M. Murnane, and H. C. Kapteyn. 90 GW peak power few-cycle mid-infrared pulses from an optical parametric amplifier. Optics Letters, 36: 2755-2757, 2011.

[30] G. Cerullo and S. De Silvestri. Ultrafast optical parametric amplifiers. Review of Scientific Instruments, 74: 1-17, 2003.

[31] L. V. Dao, C. Hall, H. L. Vu, K. B. Dinh, E. Balaur, P. Hannaford, and T. A. Smith. Phase-matched generation of highly coherent radiation in water window region. Applied. Optics, 51: 4240-4245, 2012.

[32] H. Xiong, H. Xu, Y. Fu, J. Yao, B. Zeng, W. Chu, Y. Cheng, Z. Xu, E. J. Takahashi, K. Midorikawa, X. Liu, and J. Chen. Generation of a coherent x ray in the water window

region at 1 kHz repetition rate using a mid-infrared pump source. Optics Letters, 34: 1747-1749, 2009.

[33] J. Stohr. *NEXAFS Spectroscopy* (Springer, New York, 1992).

[34] S. Pabst. Atomic and molecular dynamics triggered by ultrashort light pulses on the atto- to picosecond time scale. European Physical Journal Special Topics, 221: 1-71, 2013.

[35] G. A. Mourou, T. Tajima, S. V. Bulanov. Optics in the relativistic regime. Reviews of Modern Physics, 78: 309-371, 2006.

[36] B. N. Chicbkov, C. Momma, S. Nolte, F. yon Alvensleben, A. Tiinnermann. Femtosecond, picosecond and nanosecond laser ablation of solids. Applied Physics A, 63: 109-115, 1996.

[37] R. R. Gattass and E. Mazur. Femtosecond laser micromachining intransparent materials. Nature Photonics, 2: 219-225, 2008.

[38] Kendall E. Donaldson, Rosa Braga-Mele, Florence Cabot, Richard Davidson, Deepinder K. Dhaliwal, L.Ac, Rex Hamilton, Mitchell Jackson, Larry Patterson, Karl Stonecipher, Sonia H. Yoo. Femtosecond laser–assisted cataract surgery. Journal of Cataract & Refractive Surgery, 39: 1753–1763, 2013.

[39] A. J. DeMaria, D. A. Stetser, and H. Heynau. Self Modelocking of Lasers With Saturable Absorbers. Applied Physics Letters, 8: 174-176, 1966.

[40] U. Keller, D. A. B. Miller, G. D. Boyd, T. H. Chiu, J. F. Ferguson, and M. T. Asom. Solid-state low-loss intracavity saturable absorber for Nd:YLF lasers: an antiresonant semiconductor Fabry-Perot saturable absorber. Optics Letters, 17: 505-507, 1992.

[41] Wayne H. Knox. Femtosecond Optical Pulse Amplification. IEEE Journal of Quantum Electronics, 24: 388-397, 1988.

[42] A. M. Weiner. *Ultrafast Optics*. (John Wiley & Sons, Inc., Hoboken, New Jersey, 2009).

[43] R. Paschotta. *Encyclopedia for Photonics and Laser Technology.* Open Access online.

[44] S. Backus, C. G. Durfee, M. M. Murnane, and H. C. Kapteyn. High power ultrafast lasers. Review of Scientific Instruments, 69: 1207- 1223, 1998.

[45] D. C. Brown. The Promise of Cryogenic Solid-State Lasers. IEEE Journal of Selected Topics in Quantum Electronics, 11: 587-599, 2005.

[46] W. Koechner. *Solid-State Laser Engineering*. (Springer, New York, 2006).

[47] W. Koechker and D. K. Rice. Effect of Birefringence on the Performance of Linearly Polarized YAG:Nd Lasers. IEEE Journal of Quantum Electronics, QE-6: 557-566, 1970.

[48] W. Koechner. Rupture Stress and Modulus of Elasticity for Nd:YAG Crystals. Applied Physics, 2: 279-280, 1973.

[49] W. Koechner. Thermal Lensing in a Nd:YAG Laser Rod. Applied Optics, 9: 2548-2553, 1970.

[50] W. Koechner. Absorbed Pump Power, Thermal Profile and Stresses in a cw Pumped Nd:YAG Crystal. Applied Optics, 9: 1429-1434, 1970.

[51] A. Yariv and P. Yeh. *Optical Waves in Crystals: Propagation and Control of Laser Radiation.* (John Wiley & Sons, Inc., Hoboken, New Jersey, 2003)

[52] J. -M. Heritier, S. Fournier, G. J. Germann, B. Resan, R. Viselga, and A. Fry. Cryogenically cooled Ti:Sapphire amplifiers. Proceedings of SPIE, 6451: 64510, 2007.

[53] R.H. Stolen and A. Ashkin. Optical Kerr effect in glass waveguide. Applied Physics Letters, 22: 294-296, 1973.

[54] I. Matsushima, H. Yashiro, and T. Tomie. A 37% Efficiency, Kilohertz Repetition Rate Cryogenically Cooled Ti:Sapphire Regenerative Amplifier. Japanese Journal of Applied Physics, 44: L823-L826, 2005.

[55] A. E. Siegman. Defining, measuring, and optimizing laser beam quality. Proceedings of SPIE, 1868: 2-12, 1993.

[56] I. Jovanovic, B. J. Comaskey, and D. M. Pennington. Angular effects and beam quality in optical parametric amplification. Journal of Applied Physics, 90: 4328-4337, 2001.

[57] A. M. Weiner. Ultrafast optical pulse shaping: A tutorial review. Optics Communications, 284: 3669-3692, 2011.

[58] C. Li, Y. Leng, C. Zhang, X. Liang, R. Li, Z, Xu. An Ultra-Broadband Spatially Dispersed Regenerative Amplifier Free from Spatial Chirp. Chinese Physics Letter, 25: 2048-2050, 2008.

[59] R. Lausten and P. Balling. Thermal lensing in pulsed laser amplifiers: an analytical model. Journal of the Optical Society of America B, 20: 1479-1485, 2003.

[60] T. A. Planchon, W. Amir, C. Childress, J. A. Squier and C. G. Durfee. Measurement of pump-induced transient lensing in a cryogenically-cooled high average power Ti:sapphire amplifier. Optics Express, 16: 18557-18564, 2008.

[61] T. Kobayashi and Y. Kida. Ultrafast spectroscopy with sub-10 fs deep-ultraviolet pulses. Physical Chemistry Chemical Physics, 14: 6200-6210, 2012.

[62] J. D. Geiser, S. M. Dylewski, J. A. Mueller, R. J. Wilson, R. Toumi, and P. L. Houston. The vibrational distribution of O_2 ($X\sum_g^-$) produced in the photodissociation of ozone between 226 and 240 and at 266 nm. Journal of Chemical Physics, 112: 1279-1286, 2000.

[63] S. A. Trushin, W. E. Schmid, and W. Fuß. A time constant of 1.8 fs in the dissociation of water excited at 162 nm. Chemical Physics Letters, 468: 9-13, 2009.

[64] T. Kiss, F. Kanetaka, T. Yokoya, T. Shimojima, K. Kanai, S. Shin, Y. Onuki, T. Togashi, C. Zhang, C. T. Chen, and S. Watanabe. Photoemission Spectroscopic Evidence of Gap Anisotropy in an f-Electron Superconductor. Physical Review Letters, 94: 057001, 2005.

[65] K. Kosma, S. A. Trushin, W. Fuss, and W. E. Schmid. Ultrafast Dynamics and Coherent Oscillations in Ethylene and Ethylene-d_4 Excited at 162 nm. Journal of Physical Chemistry A, 112: 7514-7529, 2008.

[66] T. Kanai, X. Wang, S. Adachi, S. Watanabe, and C. Chen. Watt-level tunable deep ultraviolet light source by a KBBF prism-coupled device. Optics Express, 17: 8696-8703, 2009.

[67] X. Zhang, Z. M. Wang, S. Y. Luo, G. L. Wang, Y. Zhu, Z. Y. Xu, C.T. Chen. Widely tunable fourth harmonic generation of a Ti:sapphire laser based on RBBF crystal. Applied Physics B, 102: 825-830, 2011.

[68] T. Kanai, T. Kanda, T. Sekikawa, S. Watanabe, T. Togashi, C. Chen, C. Zhang, Z. Xu, and J. Wang. Generation of vacuum-ultraviolet light below160 nm in a KBBF crystal by the fifth harmonic of a single-mode Ti:sapphire laser. Journal of the Optical Society of America B, 21: 370-375, 2004.

[69] C. G. Durfee, S. Backus, M. M. Murnane, and H. C. Kapteyn. Ultrabroadband phase-matched optical parametric generationin the ultraviolet by use of guided waves. Optics Letters, 22:1565-1567, 1997.

[70] C. G. Durfee, S. Backus, H. C. Kapteyn, and Margaret M. Murnane. Intense 8-fs pulse generation in the deep ultraviolet. Optics Letters, 24: 697-699, 1999.

[71] L. Misoguti, S. Backus, C. G. Durfee, R. Bartels, M. M. Murnane, and H. C. Kapteyn. Generation of Broadband VUV Light Using Third-Order Cascaded Processes. Physical Review Letters, 87: 013601, 2001.

[72] C. G. Durfee, L. Misoguti, S. Backus, H. C. Kapteyn, and M. M. Murnane. Phase matching in cascaded third-order processes. Journal of the Optical Society of America B, 19: 822-831, 2002.

[73] T. Nagy and P. Simon. Generation of 200 μJ, sub-25-fs deep-UV pulses using a noble-gas-filled hollow fiber. Optics Letters, 34: 2300-2302, 2009.

[74] F.Reiter, U. Graf, M. Schultze, W. Schweinberger, H. Schröder, N. Karpowicz, A. M. Azzeer, R. Kienberger, F. Krausz, and E. Goulielmakis. Generation of sub-3 fs pulses in the deep ultraviolet. Optics Letters, 35: 2248-2250, 2010.

[75] J. Wojtkiewicz, K. Hudek and C. G. Durfee. Chirped-pulse frequency conversion of ultrafast pulses to the deep-UV. OSA/CLEO, CMK5, 2005.

[76] P. Zuo, T. Fuji, and T. Suzuki. Spectral phase transfer to ultrashort UV pulses through four-wave mixing. Optics Express, 18: 16183-16192, 2010.

[77] Y. Kida and T. Kobayashi. Generation of sub-10 fs ultraviolet Gaussian pulses. Journal of the Optical Society of America B, 28: 139-148, 2011.

[78] F. Thëberge, N. Aközbek, W. Liu, A. Becker, and S.-L. Chin. Tunable Ultrashort Laser Pulses Generated through Filamentation in Gases. Physical Review Letters, 97: 023904, 2006.

[79] T. Fuji, T. Horio, and Toshinori Suzuki. Generation of 12 fs deep-ultraviolet pulses by four-wave mixing through filamentation in neon gas. Optics Letters, 32: 2483-2481, 2007.

[80] M. Beutler, M. Ghotbi, and Frank Noack. Generation of intense sub-20-fs vacuum ultraviolet pulses compressed by material dispersion. Optics Letters, 36: 3726-3728, 2011.

[81] T. Horio, T. Fuji, Y.-I. Suzuki, and T. Suzuki. Probing Ultrafast Internal Conversion through Conical Intersection via Time-Energy Map of Photoelectron Angular Anisotropy. Journal of the American Chemical Society, 131, 10392-10393, 2009.

[82] F. Gebert, M. H. Frosz, T. Weiss, Y. Wan, A. Ermolov, N. Y. Joly, P. O. Schmidt, and P. St. J. Russell. Damage-free single-mode transmission of deep-UV light in hollow-core PCF. Optics Express, 22: 15388-15396, 2014.

[83] P. St. J. Russell, P. Hölzer, W. Chang, A. Abdolvand and J. C. Travers. Hollow-core photonic crystal fibres for gas-based nonlinear optics. Nature Photonics, 8: 278-286, 2014.

[84] E. Snitzer. Cylindrical Dielectric Waveguide Modes. Journal of the Optical Of Society America, 51: 491-498, 1961

[85] E. A. J. Marcatili and R. A. Schmeltzer. Hollow metallic and dielectric waveguides for long distance transmission and lasers. Bell System Technical Journal, 43: 1783-1810, 1964.

[86] J. J. Degnan. Waveguide laser mode patterns in the near and far-field. Applied Optics, 12: 1026-1030, 1973.

[87] R. M. Jenkins and R. W. J. Devereux. Effect of field regeneration on the TEM_{00} transmission characteristics of a circular-section waveguide. Applied Optics, 31: 5086-5091, 1992.

[88] A. M. Zheltikov. Ultrashort light pulses in hollow waveguides. Physics-Uspekhi, 45 (7): 687- 718, 2002.

[89] D. Attwood. Soft X-rays and extreme ultraviolet radiation: principles and applications. Cambridge University Press, 1999.

[90] A. McPherson, G. Gibson, H. Jara, U. Johann, T. S. Luk, I. A. McIntyre, K. Boyer, and C. K. Rhodes. Studies of multiphoton production of vacuum-ultraviolet radiation in the rare gases. Journal of the Optical Society of America B, 4: 595-601, 1987.

[91] X. F. Li, A. L Huillier, M. Ferray, L. A. Lompre, and G. Mainfray. Multiple-harmonic generation in rare gases at high laser intensity. Physical Chemistry A, 39: 5751-5761, 1989.

[92] J. Zhou, J. Peatross, M. M. Murnane, and H. C. Kapteyn. Enhanced High-Harmonic Generation Using 25 fs Laser Pulses. Physical Review Letters, 76: 752-755, 1996.

[93] Z. Chang, A. Rundquist, H. Wang, M. M. Murnane, and H. C. Kapteyn. Generation of Coherent Soft X Rays at 2.7 nm Using High Harmonics. Physical Review Letters, 79: 2967-2970, 1997.

[94] S. Sartania, Z. Cheng, M. Lenzner, G. Tempea, Ch. Spielmann, F. Krausz, and K. Ferencz. Generation of 0.1-TW 5-fs optical pulses at a 1-kHz repetition rate. Optics Letters, 22: 1562-1564, 1997.

[95] Ch. Spielmann, N. H. Burnett, S. Sartania, R. Koppitsch, M. Schnürer, C. Kan, M. Lenzner, P. Wobrauschek, F. Krausz. Generation of Coherent X-rays in the Water Window Using 5-Femtosecond Laser Pulses. Science, 278: 661-664, 1997.

[96] E. A. Gibson, A. Paul, N. Wagner, R. Tobey, D. Gaudiosi, S. Backus, I. P. Christov, A. Aquila, E. M. Gullikson, D. T. Attwood, M. M. Murnane, H. C. Kapteyn. Coherent Soft X-ray Generation in the Water Window with Quasi–Phase Matching. Science, 302: 95-98, 2003.

[97] X. Zhang, A. L. Lytle, T. Popmintchev, X. Zhou, H. C. Kapteyn, M. M. Murnane, and O. Cohen. Quasi-phase-matching and quantum-path control of high-harmonic generation using counterpropagating light. Nature Physics, 3: 270-275, 2007.

[98] K. C. Kulander, K. J. Schafer, and K. L. Krause. "Super-Intense Laser–Atom Physics," (B. Piraux, A. L'Huillier, K. Rzążewski, Eds.), Vol. 316 of NATO Advanced Studies Institute, Series B: Physics. Plenum, New York, p. 95. (1993).

[99] P. B. Corkum. Plasma Perspective on Strong-Field Multiphoton Ionization. Physical Review Letters, 71: 1994-1997, 1993.

[100] T. Popmintchev, M.-C. Chen, P. Arpin, M. M. Murnane, and Henry C. Kapteyn. The attosecond nonlinear optics of bright coherent X-ray generation. Nature Photonics, 4: 822-832, 2010.

[101] M. Lewenstein, Ph. Balcou, M. Yu. Ivanov, A. L'Huillier, and P. B. Corkum. Theory of high-harmonic generation by low-frequency laser fields. Phyiscal Review A, 49: 2117-2132, 1994.

[102] M. V. Ammosov, N. B. Delone, and V. P. Krainov. Tunnel ionization of complex atoms and of atomic ions in an alternating electromagnetic field. Soviet Physics Journal of Experimental and Theoretical Physics, 64(6): 1191-1194, 1986.

[103] W. Becker, F. Grasbon, R. Kopold, D. B. Milosevic, G.G. Paulus, and H. Walther. Above-Threshold Ionization: From Classical Features to Quantum Effects. Advances In Atomic, Molecular, And Optical Physics, 48: 35-98, 2002

[104] J. Tate, T. Auguste, H. G. Muller, P. Salières, P. Agostini, and L. F. DiMauro. Scaling of Wave-Packet Dynamics in an Intense Mid-infrared Field. Physical Review Letters, 98: 013901, 2007.

[105] K. Schiessl, K. L. Ishikawa, E. Persson, and J. Burgdörfer. Quantum Path Interference in the Wavelength Dependence of High-Harmonic Generation. Physical Review Letters, 99: 253903, 2007.

[106] M.V. Frolov, N. L. Manakov, and A. F. Starace. Wavelength Scaling of High-Harmonic Yield: Threshold Phenomena and Bound State Symmetry Dependence. Physical Review Letters, 100: 173001, 2008.

[107] A. D. Shiner, C. Trallero-Herrero, N. Kajumba, H.-C. Bandulet, D. Comtois, F. Légaré, M. Giguère, J-C. Kieffer, P. B. Corkum, and D. M. Villeneuve. Wavelength Scaling of High Harmonic Generation Efficiency. Physical Review Letters, 103: 073902, 2009.

[108] A. L'Huillier, K. J. Schafer, and K. C. Kulander. High-Order Harmonic Generation in Xenon at 1064 nm: The Role of Phase Matching. Physical Review Letters, 66: 2200-2003, 1991.

[109] Ph. Balcou and Anne L'Huillier. Phase-matching efFects in strong-field harmonic generation. Physical Review A, 47: 1447-1459, 1993.

[110] Philippe Balcou, Pascal Salières, Anne L'Huillier, and Maciej Lewenstein. Generalized phase-matching conditions for high harmonics: The role of field-gradient forces. Physical Review A, 55: 3204-3210, 1997.

[111] V. S. Popov. Tunnel and multiphoton ionization of atoms and ions in a strong laser field (Keldysh theory). Physic –Uspekhi, 47: (9) 855- 885, 2004.

[112] E. Constant, D. Garzella, P. Breger, E. Mével,1 Ch. Dorrer, C. Le Blanc, F. Salin, and P. Agostini. Optimizing High Harmonic Generation in Absorbing Gases: Model and Experiment. Physical Review Letters, 82: 1668-1671, 1999.

[113] M.-C. Chen, C. Mancuso, C. Hernández-Garcíaa, F. Dollar, B. Galloway, D. Popmintchev, P.-C. Huang, B. Walker, L. Plajac, A. A. Jaron-Becker, A. Becker, M M. Murnane, H. C. Kapteyn, and T. Popmintchev. Generation of bright isolated attosecond soft X-ray pulses driven by multicycle midinfrared lasers. Proceedings of the National Academy of Sciences of the United States of America, www.pnas.org/cgi/doi/10.1073/pnas.1407421111.

[114] C. Bressler and M. Chergui. Ultrafast X-ray Absorption Spectroscopy. Chemical Reviews, 104: 1781-1812, 2004.

[115] E. A. Stern. Theory of the extended x-ray-absorption fine structure. Physical Review B, 10: 3027-3037, 1974.

[116] A. S. Sandhu, E. Gagnon, R. Santra, V. Sharma, W. Li, P. Ho, P. Ranitovic, C. L. Cocke, M. M. Murnane, H. C. Kapteyn. Observing the Creation of Electronic Feshbach Resonances in Soft X-ray-Induced O_2 Dissociation. Science, 322: 1081-1085, 2008.

[117] Z.-H. Loh, M. Khalil, R. E. Correa, R. Santra, C. Buth, and S. R. Leone. Quantum State-Resolved Probing of Strong-Field-Ionized Xenon Atoms Using Femtosecond High-Order Harmonic Transient Absorption Spectroscopy. Physical Review letters, 98: 143601, 2007.

[118] Z.-H. Loh, C. H. Greene, S. R. Leone. Femtosecond induced transparency and absorption in the extreme ultraviolet by coherent coupling of the He 2s2p ($^1P^o$) and $2p^2$ ($1S^e$) double excitation states with 800 nm light. Chemical Physics, 350: 7-13, 2008.

[119] Z.-H. Loh and S. R. Leone. Ultrafast strong-field dissociative ionization dynamics of CH_2Br_2 probed by femtosecond soft x-ray transient absorption spectroscopy. The Journal of Chemical Physics, 128: 204302, 2008.

[120] Z.-H. Loh and S. R. Leone. Capturing Ultrafast Quantum Dynamics with Femtosecond and Attosecond X-ray Core-Level Absorption Spectroscopy. The Journal of Physical Chemistry Letters, 4: 292-302, 2013.

[121] E. Goulielmakis, Z.-H. Loh, A. Wirth, R. Santra, N. Rohringer, V. S. Yakovlev, S. Zherebtsov, T. Pfeifer, A. M. Azzeer, M. F. Kling, S. R. Leone, and F. Krausz. Real-time observation of valence electron motion. Nature, 466: 739-744, 2010.

[122] E. Hudson, D. A. Shirley, M. Domke, G. Remmers, A. Puschmann, T. Mandel, C. Xue, and G. Kaindl. High-resolution measurements of near-edge resonances in the core-level photoionization spectra of SF6. Physical Review A, 47: 361-373, 1993.

[123] M. Stener, P. Bolognesi, M. Coreno, P. O'Keeffe, V. Feyer, G. Fronzoni, P. Decleva, L. Avaldi, and A. Kivimäki. Photoabsorption and S 2p photoionization of the SF_6 molecule: Resonances in the excitation energy range of 200–280 eV. The Journal of Physical Chemistry, 134: 174311, 2011.

[124] O.-P. Sairanen, A. Kivimäki, E. Nõmmiste, H. Aksela, and S. Aksela. High-resolution pre-edge structure in the inner-shell ionization threshold region of rare gases Xe, Kr, and Ar. Physical Review A, 54: 2834-2839, 1996.

[125] C. Ding, W. Xiong, Ti. Fan, D. D. Hickstein, T. Popmintchev, X. Zhang, M. Walls, M. M. Murnane, and H. C. Kapteyn. High flux coherent supercontinuum soft X-ray source driven by a single-stage 10 mJ, Ti:sapphire amplifier pumped OPA. Optics Express, 22: 6194-6202 (2014).

[126] J. L. Dehmer. Evidence of Effective Potential Barriers in the X-Ray Absorption Spectra of Molecules. The Journal of Chemical Physics, 56: 4496-4504, 1972.

[127] J. Stöhr, J. L. Gland, E. B. Kollin, R. J. Koestner, A. L. Johnson, E. L. Muetterties, and F. Sette, Desulfurization and Structural Transformation of Thiophene on the Pt(111) Surface. Physical Review letters, 53: 2161-2164, 1984.

[128] P. Andersen, T. Andersen, F. Folkmann, V. K. Ivanov, H. Kjeldsen, and J. B. West. Absolute cross sections for the photoionization of 4d electrons in Xe^+ and Xe^{2+} ions. Journal of Physics B: Atomic, Molecular and Optical Physics, 34: 2009-2019, 2001.